ACKNOWLEDGMENTS

The author wishes to express his sincere gratitude to Professor Edward S. Yang for his invaluable advice, understanding and constant encouragement during the course of this investigation and preparation of the manuscript.

The author is also grateful to Professors Jacob Millman, Thomas C. Marshall, Alan B. Fowler, David I. Paul, and C. K. Chu for their careful reading of the manuscript and for many constructive comments and suggestions.

This research was supported in part by the National Science Foundation under Grant GK-1550 and in part by NASA under Grant NGR 33-008-090.

ABSTRACT

The internal physical mechanism that governs the current conduction in junction-gate field-effect transistors is studied. A numerical method of analyzing the devices with different length-to-width ratios and doping profiles is developed. This method takes into account the two-dimensional character of the electric field and the field-dependent mobility. Application of the method to various device models shows that the channel width and the carrier concentration in the conductive channel decrease with the increasing drain-to-source voltage for conventional devices. It also shows larger differential drain conductances for shorter devices when the drift velocity is not saturated. The interaction of the source and the drain gives the carrier accumulation in the channel which leads to the space-charge-limited current flow. The important parameters for the space-charge-limited current flow are found to be the L/L_{DE} ratio and the crossover voltage. Triode-like characteristics have been obtained for a device model with a small L/L_{DE} ratio and a small crossover voltage. In conclusion the theory presented in this dissertation explains the important features of the experimentally observed steady-state drain characteristics by clarifying the contribution of the various physical mechanisms to the current conduction.

TABLE OF CONTENTS

Chapter I: INTRODUCTION

A junction-gate field-effect transistor (JFET) is an active semiconductor junction device. The cross-sectional view of a JFET with N-channel is shown in Fig. 1.1. The two gate terminals in the figure are usually tied together. The drain current which flows parallel to the metallurgical gate junction is controlled mainly by the transverse electric field by means of the reverse biased gate P-N junction. Unlike the bipolar transistor which operates by the injection of minority carriers, the JFET is a unipolar transistor; the current is carried by the majority carriers. When compared to the bipolar transistors, the JFET has lower noise, smaller temperature dependence, stronger resistance to the radiation damage and higher DC input impedance.

The operation of the JFET was first analyzed by W. Shockley[1] for symmetric devices with heavily doped gate regions and with large length-to-width ratios, i.e.,

$$L/a > 3$$

where L is the length and 2a is the width of the active region of the device. The analysis is based on the 'Gradual-Channel Approximation' which assumes the total depletion of the free carriers in the space-charge region and the neutrality of the conducting channel. It is further assumed that the transition between the two regions is abrupt. An important parameter of the gradual-channel approximation is the pinch-off voltage, V_p which is the potential drop

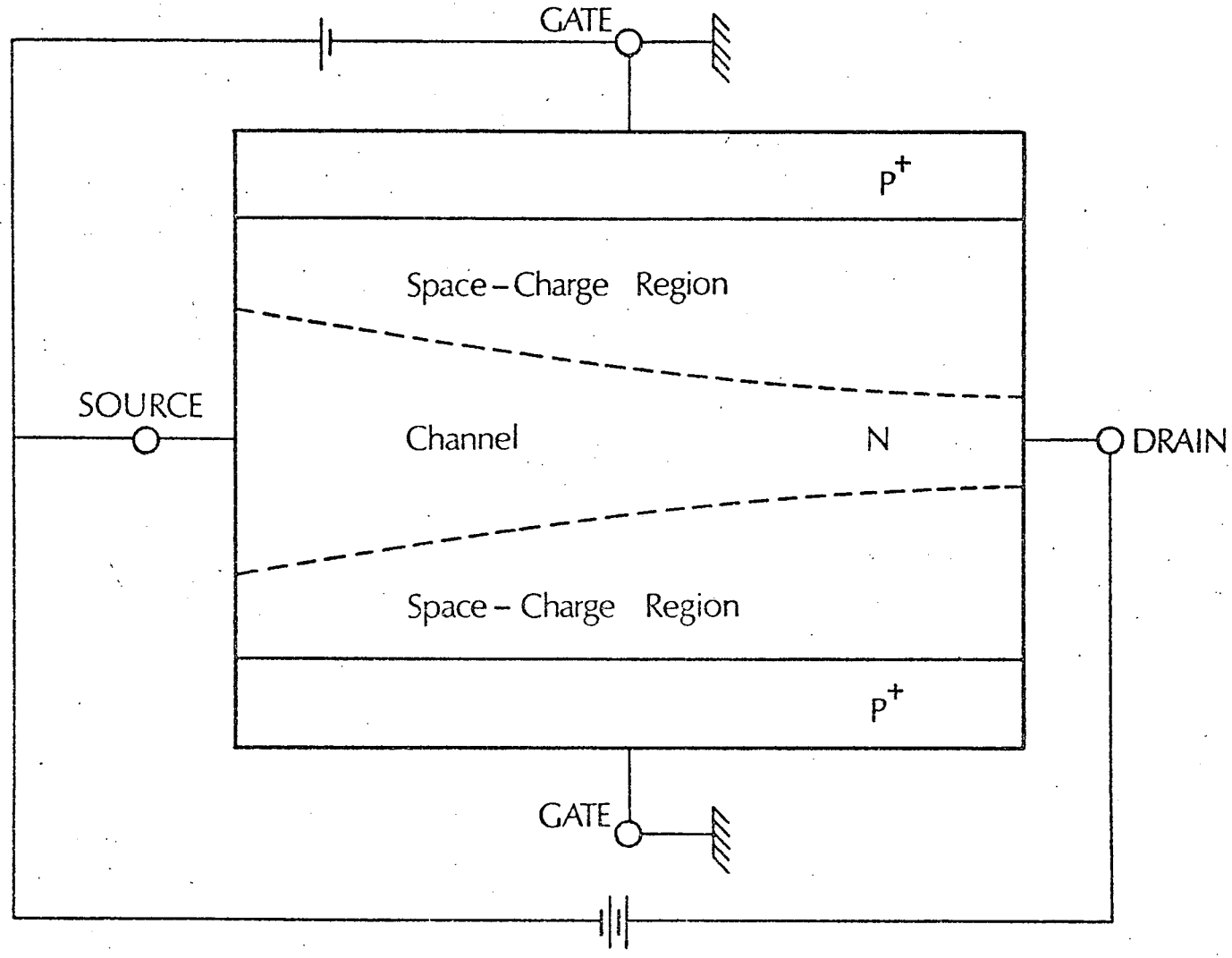

Figure 1.1 The cross-sectional view of a JFET with N-channel

across a space-charge region of width 'a' of a one-dimensional P-N junction similar to the gate P-N junction of the device. When the source and the drain terminals are shorted, the application of V_p to the gate depletes all the carriers from the channel. As was recognized by Shockley, the gradual-channel approximation is valid only for a device with a large length-to-width ratio and for the drain-to-gate voltage (V_{dg}) less than the pinch-off voltage of the device. If we assume, however, that the drain current remains constant for $V_{dg} > V_p$, the general behavior of the pentode-like external drain characteristics observed in experiments[2] is well described. Since the gradual-channel approximation gives zero channel width for $V_{dg} = V_p$, the assumption of the constant drain current implying zero differential drain conductance is arbitrary. Moreover, the internal physical mechanism of the current conduction giving this drain current can not be explained. The gradual-channel approximation has received wide acceptance due to its simplicity and its capability of giving a reasonable description of the external characteristics although it fails to give the detailed picture of the internal behavior of the device.

Esaki and Chang[3] have shown that devices with small length-to-width ratios are favorable for high-speed operations by comparing various structures of JFETs in terms of the transit time and the transconductance at some limiting bias conditions. From a similar study, Buchanan et al.[4] were also led to the same conclusion and their experimental device showed nonsaturated drain characteristics.

The failure of the gradual-channel approximation for the bias condition $V_{dg} > V_p$ originates from the strong two-dimensional field distribution near the drain. Several attempts have been made to describe this field distribution. From the assumption that the conducting channel is completely pinched-off for $V_{dg} > V_p$, Shockley and Prim[1,5] solved for the two-dimensional electric field near the drain and the solution was matched to that of the gradual-channel approximation near the source. A similar approach has been used by Wu and Sah[6] with a more refined matching process. The non-zero differential drain conductance predicted by these analyses is in general agreement with the experiments[2,6] but the starting assumption of complete pinch-off of the conducting channel is incompatible with the large drain current.

The saturation of the drift velocity with high electric fields[7,8] has been recognized as an important factor for the operation of a JFET by many authors. Dacey and Ross[9] have modified the gradual-channel approximation by assuming that the electric field is in the tepid range. An approximation which gives the mobility for the whole range of the electric field has been used by Trofimenkoff[10] and Tarney[11] to obtain an analytic solution. Grosvalet et al.[12] have used an analog computer to find the potential distribution along the center line of the channel and have suggested that the saturation of the drift velocity is the main cause of the saturation of the drain current for their device. Zuleeg[13] measured the saturation current for short devices at

various temperatures and found the same temperature dependence as the limiting drift velocity.

Hauser[14] has analyzed both long and short devices using a revised form of the gradual-channel approximation for the circular gate junction and taking into account the field dependent mobility. By qualitative arguments, he predicted a minimum channel width of the order of the Debye length and the decrease of the free carrier concentration inside the conducting channel below the thermal equilibrium value with the increasing drain voltage.

Grebene and Ghandhi[15] have proposed a device model with two regions. In region-I the gradual-channel approximation is valid and in region-II the current is confined to flow through a narrow channel whose width is much smaller than the device width. The two regions are separated by assuming that the electric field in region-II is always greater than the critical field, i.e., the drift velocity is saturated in region-II. According to this 'Two-Region Model', the carrier concentration inside the channel in region-II is larger than that in the thermal equilibrium condition.

Teszner and Gicquel[16] have fabricated devices with small length-to-width ratios by lateral diffusion techniques. Due to the fabrication process, the doping profiles of these devices are non-uniform along the channel. These devices have shown both pentode-like and triode-like characteristics. From the similarity with the space-charge-limited current, where the current is proportional

to the square of the applied voltage, they suggested that the change in the drain characteristics is due to the joining of the two gate regions underneath the source region during the diffusion process. The device is then equivalent to a bipolar transistor operating beyond the punch-through point and the current is space-charge limited. Zuleeg[17] has developed this idea further and fabricated a device with N^+-N-P-N-N^+ structure which showed both the space-charge-limited operation and the bipolar operation.

When the analyses of conventional JFETs reported so far are investigated closely, they have an important common feature. They start from some assumptions about the shape of the channel and the free carrier concentration inside the channel. The Poisson's equation and the continuity equation are then simplified and solved for the space-charge region and the conducting channel separately. Since the equations are nonlinear partial differential equations, assumptions are necessary to obtain an analytic solution. As we have seen, however, different assumptions lead to conflicting results.

The purpose of the present investigation can be divided into two parts. The first part is to find the physical mechanism of the current conduction for the devices with different length-to-width ratios and with different doping profiles along the channel. For this purpose, an iterative numerical method which can solve the equations without any assumptions concerning the distribution of free carriers is developed. The method takes into account the

two-dimensional character of the electric field and the variation of the mobility with electric fields. The comparison of the solutions for various device models will clarify the effects of the geometry, bias voltages, and the field dependent mobility to the current conduction mechanism. The solution can also be used to find the validity of the assumptions of other analyses.

The second part of the investigation is concerned with the triode characteristics. The devices considered here have essentially the same geometrical structure as the conventional JFETs. The study is based on the space-charge-limited (SCL) current for a one-dimensional N^+-N-N^+ structure. The possibility and the criterion of obtaining the triode characteristics are investigated in terms of the parameters characterizing the device.

Chapter II: MATHEMATICAL FORMULATION

II-1 Device Model and Basic Equations

Fig. 2.1 shows the geometry of the model of a practical device with the coordinates to be used later. For simplicity only N-channel devices will be considered here. It is assumed that the P^+-N junctions at the gate are step junctions and that the doping profile of the N^+-N junctions at the source and the drain contacts are described by complementary error functions. The gate P^+-regions are much more heavily doped than both N- and N^+-regions.

By assuming no variation along the Z-direction, the region of interest is a plane bounded by $X = 0$, $X = L_o$, $Y = a$, and $Y = -a$. The two N^+-regions are included in the analysis to obtain a relatively simple boundary condition and to find out any possible effect of these regions to the pinch-off phenomenon. For a device with a very small length, these N^+-regions are of primary importance in that the interaction of them makes the space-charge-limited current possible.

The specific device model shown has been chosen to avoid the complexity of mathematics while retaining the important features for the device characterization.

When the electro-static potential and the quasi-Fermi levels for electrons and holes are chosen as dependent variables, Poisson's equation and continuity equations are[18]

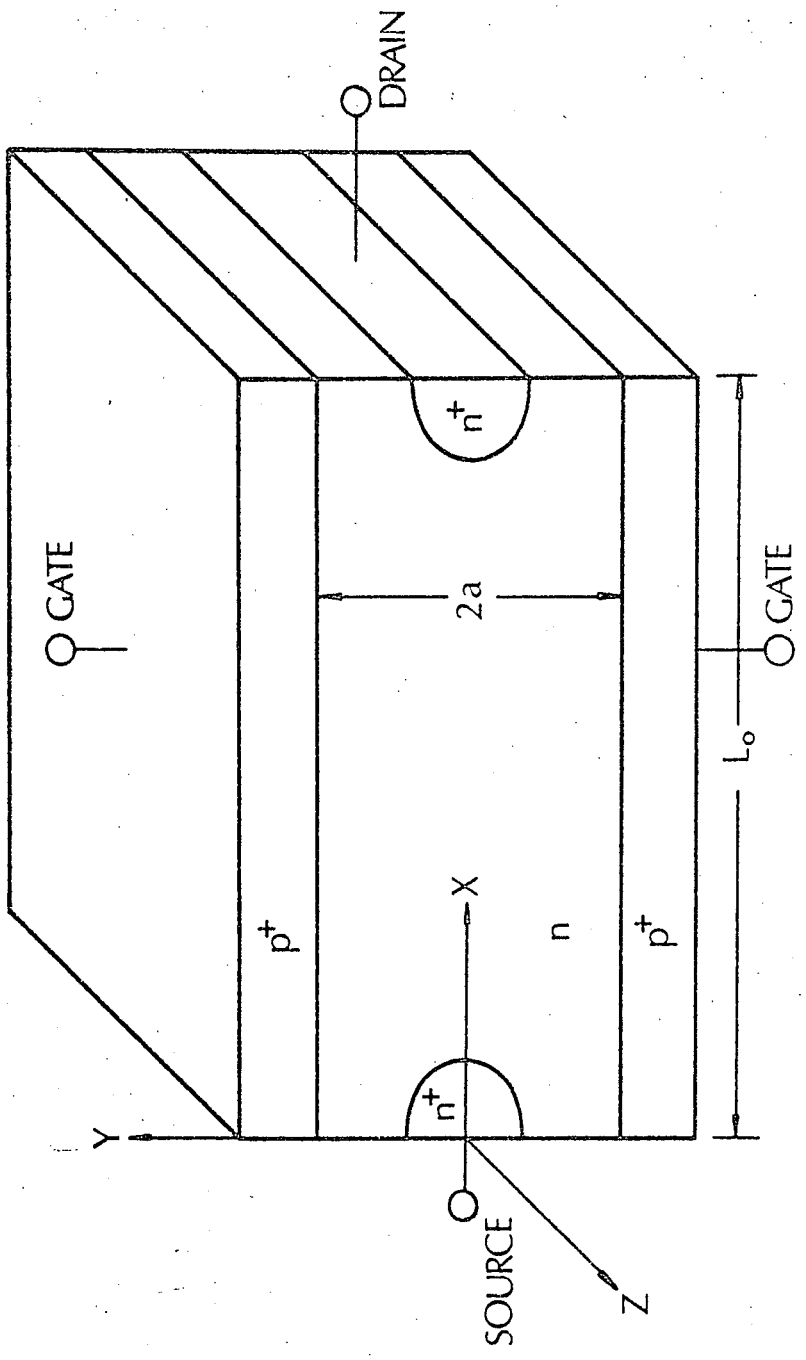

Figure 2.1 Device Model and Coordinates

$$\nabla^2\Psi = -2\alpha[N(x,y) - P(x,y) - n(x,y) + p(x,y)] \qquad (2.1)$$

$$\nabla\cdot\vec{J}_n = \nabla\cdot\left[-\frac{1}{\alpha}\, n(x,y)\ \mu_n\ \nabla\varphi_n\right] = R \qquad (2.2)$$

$$\nabla\cdot\vec{J}_p = \nabla\cdot\left[-\frac{1}{\alpha}\, p(x,y)\ \mu_p\ \nabla\varphi_p\right] = -R \qquad (2.3)$$

The symbols used in equations (2.1) - (2.3) are defined as follows:

Ψ = electro-static potential normalized by kT/q

φ_n = quasi-Fermi level for electrons normalized by kT/q

φ_p = quasi-Fermi level for holes normalized by kT/q

N = donor concentration normalized by N_D

P = acceptor concentration normalized by N_D

n = electron concentration normalized by N_D

p = hole concentration normalized by N_D

$\vec{J}_n$ = electron current density normalized by $qN_D\mu_{no}\ V_p/a$

$\vec{J}_p$ = hole current density normalized by $qN_D\mu_{po}\ V_p/a$

μ_n = electron mobility normalized by μ_{no}

μ_p = hole mobility normalized by μ_{po}

α = ratio of the pinch-off voltage to the thermal voltage = $V_p\ /\ (kT/q)$

V_p = pinch-off voltage of the device = $qN_Da^2/(2\epsilon\epsilon_o)$

μ_{no} = low field electron mobility

μ_{po} = low field hole mobility

N_D = donor concentration of the N-region

a = half of the width of the N-region

R = net rate of recombination

x, y = X, Y normalized by a

When equations (2.1) - (2.3) are combined with the results of the Boltzmann statistics

$$n = e^{\Psi-\varphi_n} \tag{2.4}$$

$$p = e^{\varphi_p-\Psi} \tag{2.5}$$

we obtain a set of equations which, when solved, describes non-degenerate semiconductor devices.

α is related to the ratio of the extrinsic Debye length, L_{DE}, to a by

$$\frac{L_{DE}}{a} = \sqrt{\frac{\epsilon\epsilon_o kT}{q^2 N_D}} \Big/ a = \frac{1}{\sqrt{2\alpha}}$$

The transition from the space-charge region to the neutral channel takes place in about $3L_{DE}$.[19] If this transition is to be treated as abrupt, we should have at least $3L_{DE}/a \leq 0.1$, which is equivalent to $\alpha \geq 450$ or $V_p \geq 11.6$ Volts. For a device with $V_p \sim 2$ Volts, which is quite common these days, the transition region is about 25% of the device width. Moreover, if the minimum width of the conducting channel is in the order of L_{DE} as predicted by Hauser[14], the correct description of the pinch-off is possible only when the finiteness of the transition region is taken into account.

Since a JFET is a majority carrier device, the contribution of the hole current to the drain current is negligible and the hole density is always very small compared to the donor density in the region of interest. Therefore, the net rate of recombination can be considered insignificant. From these considerations, we may simplify equations (2.1) - (2.5) as

$$\nabla^2\psi = -2\alpha\left[N(x,y) - e^{\psi-\varphi_n}\right] \tag{2.6}$$

$$\nabla\cdot\vec{J}_n = \nabla\cdot\left[-\frac{1}{\alpha}\, e^{\psi-\varphi_n}\, \mu_n\, \nabla\varphi_n\right] = 0 \tag{2.7}$$

$$\nabla\cdot\vec{J}_p = 0 \tag{2.8}$$

Since equation (2.6) is to be applied to N-region only, we have put $P(x,y) = 0$.

It is to be noted that the neglect of the net rate of recombination is equivalent to the zero gate current or infinite DC input impedance.

II-2 One-Dimensional Formulation

Before going into the detailed discussion of equations (2.6) and (2.7), a brief summary of the gradual-channel approximation will be presented in this section. This will be followed by a critical review of the approximation and a range of validity will be estimated.

II-2-a Gradual-Channel Approximation

The gradual-channel approximation starts from dividing the region of interest into the space-charge region and the conducting channel with an abrupt transition. It is assumed that the space-charge region is completely devoid of free carriers and the channel is neutral. Consider a device with a uniform doping level, i.e., $N(x,y) = 1$, and a large length-to-width ratio. The electric field in the space-charge region is mainly in the Y-direction and the Poisson's equation is simplified as

$$\frac{d^2\Psi}{dy^2} = -2\alpha \qquad \frac{b}{a} \leq |y| \leq 1 \tag{2.9}$$

where b is half of the conducting channel width. (See Fig. 2.3). Due to the symmetry of the device, we may consider only the upper half of the entire region ($y \geq 0$). Since the gate P^+-region is much more heavily doped than the N-region, the space-charge region lies in the N-region only and the potential along the line $y = \pm 1$ is constant. When this potential is taken as the reference, we obtain

$$\Psi(y = 1) = 0 \tag{2.10}$$

Another boundary condition for equation (2.9) comes from the assumption that the electric field inside the channel is in X-direction only, i.e.,

$$\frac{d\Psi}{dy}\left(y = \frac{b}{a}\right) = 0 \tag{2.11}$$

The solution of equation (2.9) subject to the boundary conditions (2.10) and (2.11) gives the potential in the space-charge region as

$$\Psi = -\alpha\left(y^2 - 1\right) + 2\alpha\left(\frac{b}{a}\, y - \frac{b}{a}\right) \qquad \frac{b}{a} < y < 1 \tag{2.12}$$

The potential inside the channel is obtained by putting $y = b/a$ in equation (2.12).

$$\Psi_c = \alpha\left(1 - \frac{b}{a}\right)^2 \qquad |y| < \frac{b}{a} \tag{2.13}$$

Note the implicit dependence of Ψ_c upon x through b(x) which is yet to be determined.

Because of the neutrality of the channel and the uniform doping, the current inside the channel is entirely drift current. Assuming a constant mobility, the drain current is

$$\begin{aligned} I_D &= -2 \int_0^{b/a} J_x \, dy \\ &= \frac{2}{\alpha} \int_0^{b/a} \frac{d\Psi_c}{dx} \, dy \\ &= -4 \frac{b}{a^2} \left(1 - \frac{b}{a}\right) \frac{db}{dx} \end{aligned} \tag{2.14}$$

where I_D is normalized by $q\mu_{no} N_D V_p$. The integration of equation (2.14) yields

$$x = \frac{2}{3I_D}\left[3\left\{\left(\frac{b_s}{a}\right)^2 - \left(\frac{b}{a}\right)^2\right\} - 2\left\{\left(\frac{b_s}{a}\right)^3 - \left(\frac{b}{a}\right)^3\right\}\right] \qquad (2.15)$$

and

$$I_D = \frac{2a}{3L}\left[3\left\{\left(\frac{b_s}{a}\right)^2 - \left(\frac{b_D}{a}\right)^2\right\} - 2\left\{\left(\frac{b_s}{a}\right)^3 - \left(\frac{b_D}{a}\right)^3\right\}\right] \qquad (2.16)$$

where L is the length of the device and b_s and b_D are half of the conducting channel width at the source and the drain respectively. The drain current can also be expressed as a function of the potential at the source and the drain using equations (2.13) and (2.16).

$$I_D = \frac{2a}{3L}\left[\frac{\Psi_{cD}}{\alpha}\left(3 - 2\sqrt{\frac{\Psi_{cD}}{\alpha}}\right) - \frac{\Psi_{cs}}{\alpha}\left(3 - 2\sqrt{\frac{\Psi_{cs}}{\alpha}}\right)\right] \qquad (2.17)$$

where

$$\Psi_{cs} = \alpha\left(1 - \frac{b_s}{a}\right)^2$$

$$\Psi_{cD} = \alpha\left(1 - \frac{b_D}{a}\right)^2$$

$\Psi_c = \alpha$ implies $b = 0$, i.e., the conducting channel is completely pinched-off. Since $b \geq 0$, it is clear that the above analysis applies only for $\Psi_c \leq \alpha$.

Fig. 2.2 shows the drain characteristics predicted by equation (2.17). Here, the drain current for $\Psi_{cD} \geq \alpha$ has been assumed to be constant.

The electro-static potential as a function of x and y is given by equations (2.12), (2.13), and (2.15) and the channel shape, i.e., b(x) is given implicitly by equation (2.15). These results are shown in Fig. 2.3 for $\Psi_{cs} = 0$, $\Psi_{cD} = \alpha$, and $L/a = 3$. In the figure, the electrostatic potential is divided by α.

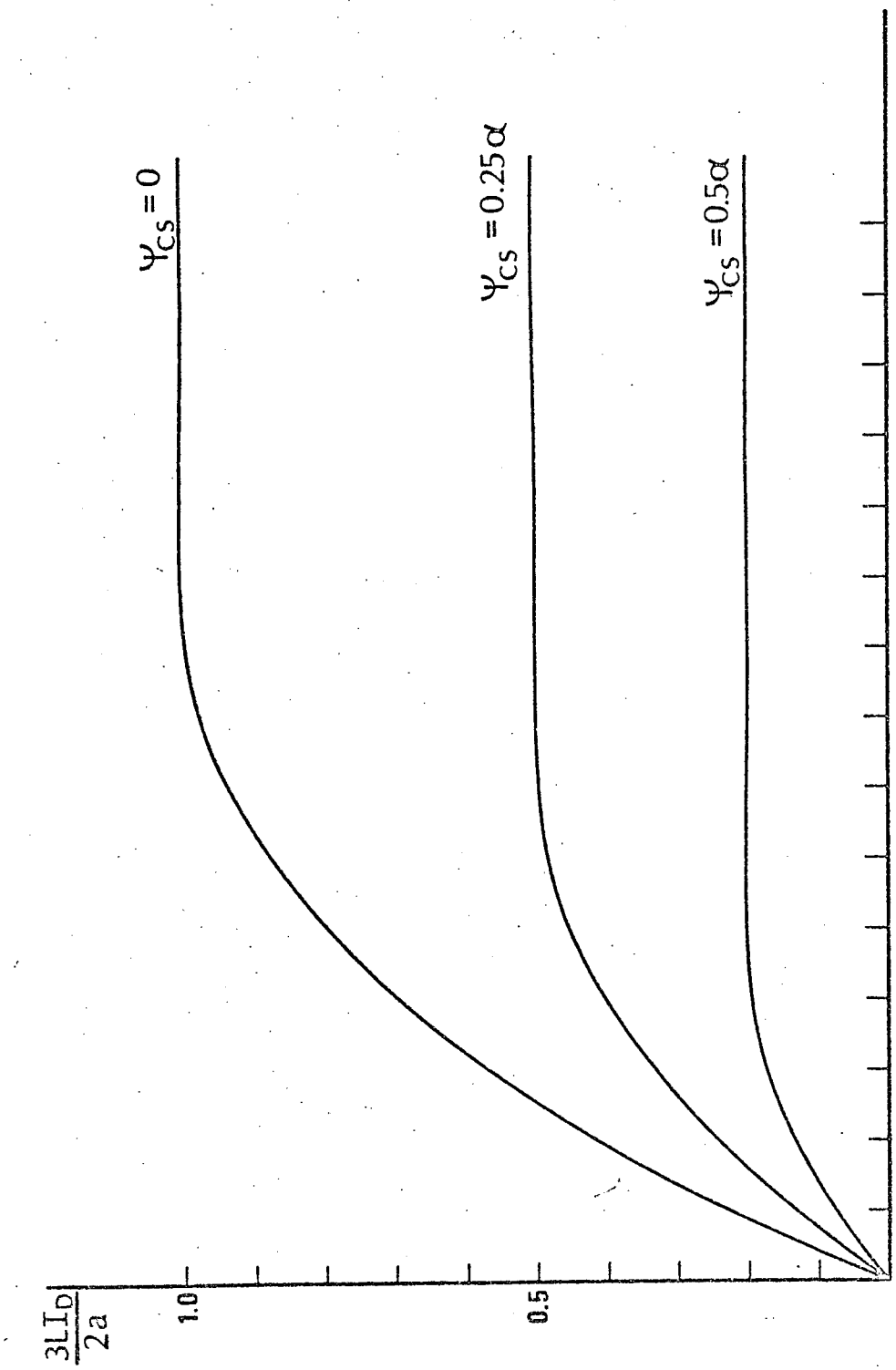

Figure 2.2 Drain characteristics of a JFET
- Gradual-Channel Approximation

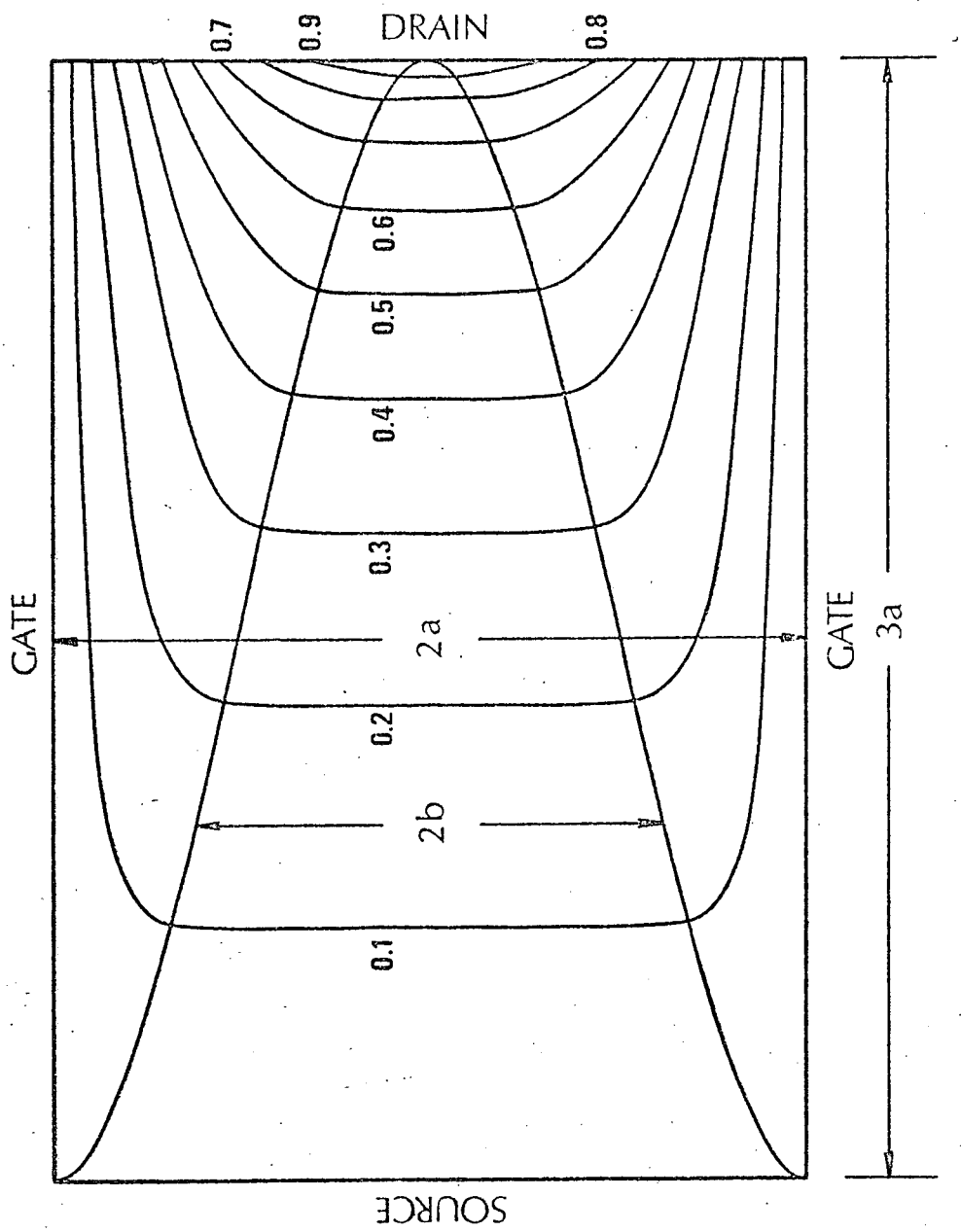

Figure 2.3 Electro-Static Potential and Channel Shape
-Gradual-Channel Approximation

II-2-b Valid Range of the Gradual-Channel Approximation

It was assumed in deriving equation (2.14) that, inside the channel, the potential is a function of x only and that the charge neutrality is maintained. These two assumptions, however, are related to each other by the Poisson's equation.

$$n = 1 + \frac{1}{2\alpha} \frac{d^2 \psi_c}{dx^2} \tag{2.18}$$

The second term of the right hand side of equation (2.18), which will be denoted by δn, indicates the deviation from the charge neutrality condition of the channel. From equation (2.13),

$$\delta n = \left[\frac{d}{dx}\left(\frac{b}{a}\right)\right]^2 - \left(1 - \frac{b}{a}\right) \frac{d^2}{dx^2}\left(\frac{b}{a}\right) \tag{2.19}$$

The condition of the constant drain current along x gives

$$\frac{dI_D}{dx} = -4\left[\frac{b}{a}\left(1 - \frac{b}{a}\right) \frac{d^2}{dx^2}\left(\frac{b}{a}\right) + \left(1 - 2\frac{b}{a}\right)\left\{\frac{d}{dx}\left(\frac{b}{a}\right)\right\}^2\right] = 0 \tag{2.20}$$

When equations (2.19) and (2.20) are combined, we obtain

$$\delta n = \frac{1 - \frac{b}{a}}{\frac{b}{a}} \left\{\frac{d}{dx}\left(\frac{b}{a}\right)\right\}^2 \tag{2.21}$$

or when equation (2.14) is used

$$\delta n = \frac{a^5 \left(\frac{3LI_D}{2a}\right)^2}{36L^2 b^3 \left(1 - \frac{b}{a}\right)} \qquad (2.22)$$

In this equation, the drain current is divided by $\frac{2a}{3L}$ which is the maximum possible value predicted by equation (2.16).

We will adopt a criterion that the gradual-channel approximation can be considered as valid if $\delta n \leq 0.1$. Thus,

$$3.6 \frac{L^2 b^3}{a^5} \left(1 - \frac{b}{a}\right) \geq \left(\frac{3LI_D}{2a}\right)^2 \qquad (2.23)$$

A graphical method of finding the range of b for which equation (2.23) is satisfied is shown in Fig. 2.4 by an example. The left hand side of equation (2.23) is shown as a function of b/a for three different values of L/a and the current level is indicated on the right edge of the figure. The example is for a device with L/a = 3 and for $\frac{3LI_D}{2a} = 0.7$. The valid range of b for this case is

$$0.27a \leq b \leq 0.98a$$

From the figure we can observe the following points:

(a) If L/a is small, the gradual-channel approximation is not valid at all for a high current level. (See the curve for L/a = 1.)

(b) The range of b increases with increasing L/a and with decreasing drain current.

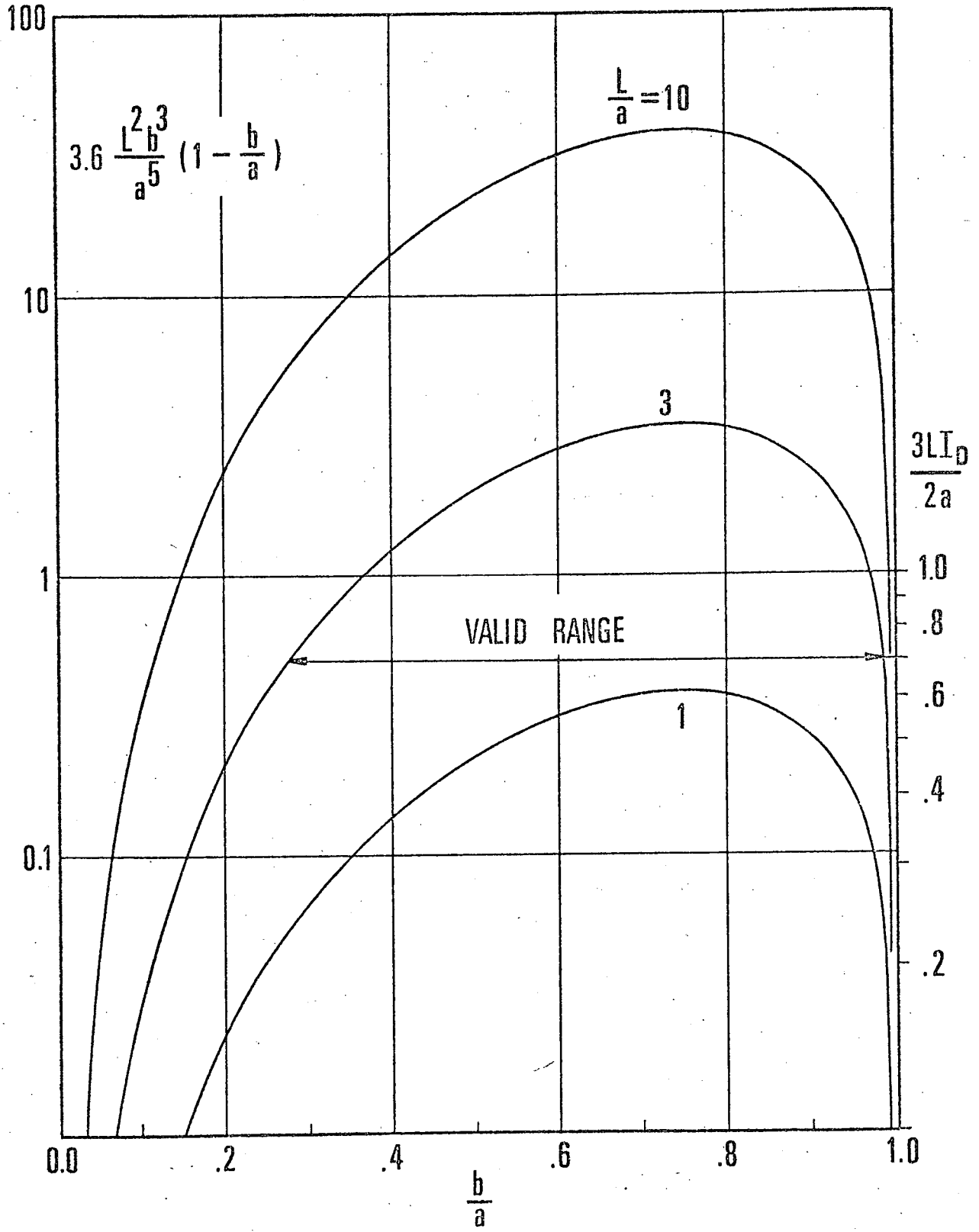

Figure 2.4 Graphical Method of Finding the Valid Range of b

(c) Even for a long device, the gradual-channel approximation is inadequate near pinch-off (small b).

By comparing the foregoing observations with the potential diagram in Fig. 2.3, one notes that the failure of the gradual-channel approximation is always associated with the two-dimensional field distribution.

It is clear by now that the operation of a JFET near and beyond pinch-off must be analyzed two-dimensionally. The solution thus obtained is expected to show the non-zero differential drain conductance in the saturation region and the physical mechanism of the current conduction beyond pinch-off. Another advantage of this approach is that both long and short devices can be treated by the same method. Therefore, the effects of the geometry of the device to the external drain characteristics can be found.

II-3 Two-Dimensional Formulation

II-3-a Poisson's Equation

Equation (2.6) is a nonlinear elliptic partial differential equation and has a unique solution when $N(x,y)$, φ_n, and boundary conditions are given. If an approximate solution Ψ_a is known, the equation can be expanded in terms of the difference $\delta\Psi$ between the exact solution and the approximate solution. Let

$$\Psi = \Psi_a + \delta\Psi \tag{2.24}$$

Then

$$\nabla^2\delta\Psi - 2\alpha e^{\Psi_a-\varphi_n}\,\delta\Psi = -\nabla^2\Psi_a - 2\alpha\left[N(x,y) - e^{\Psi_a-\varphi_n}\right] + O(\delta\Psi^2) \tag{2.25}$$

Neglecting the terms of second and higher order, we obtain a linear equation for $\delta\Psi$.

$$\nabla^2\delta\Psi - 2\alpha e^{\Psi_a-\varphi_n}\,\delta\Psi = -\nabla^2\Psi_a - 2\alpha\left[N(x,y) - e^{\Psi_a-\varphi_n}\right] \tag{2.26}$$

From an argument similar to that leading to equation (2.10), the boundary condition for Ψ along $y = 1$ and $y = -1$ is

$$\Psi(x,1) = \Psi(x,-1) = 0 \tag{2.27}$$

The thermal equilibrium condition at the source and the drain contacts gives

$$n(0,0) = n\left(\frac{L_o}{a},0\right) = N\left(0,0\right) = N\left(\frac{L_o}{a},0\right) = N_D^+/N_D$$

By using equation (2.4), we obtain

$$\Psi(0,0) = \varphi_n(0,0) + \ln\left(\frac{N_D^+}{N_D}\right) \tag{2.28}$$

$$\Psi\left(\frac{L_o}{a},0\right) = \varphi_n\left(\frac{L_o}{a},0\right) + \ln\left(\frac{N_D^+}{N_D}\right) \tag{2.29}$$

$\varphi_n(0,0)$ and $\varphi_n\left(\frac{L_o}{a},0\right)$ are determined by the applied bias voltages.

$$\varphi_n(0,0) = \alpha V_{gs}\left(1 - \frac{V_B}{V_p}\right) + \alpha \frac{V_B}{V_p} \tag{2.30}$$

$$\varphi_n\left(\frac{L_o}{a},0\right) = \alpha V_{ds}\left(1 - \frac{V_B}{V_p}\right) + \varphi_n(0,0) \tag{2.31}$$

where V_B is the built-in potential of the P^+-N gate junction. In these equations, the applied bias voltages are normalized by $V_p - V_B$ because this is what is measured from the terminals. A positive V_{gs} means a negative gate voltage with respect to the source and a positive V_{ds} means a positive drain voltage with respect to the source.

It will be shown in section II-3-b that the quasi-Fermi level for electrons can be treated as a function of x only;

$$\varphi_n = \varphi_n(x) \tag{2.32}$$

With φ_n determined by equations (2.30) - (2.32), the one-dimensional variation of the Poisson's equation (2.26) can be solved along the lines $X = 0$ and $X = L_o$ with the boundary conditions given by equations (2.27) - (2.29). This solution is then used as the boundary condition for the original two-dimensional Poisson's equation.

In this way, the boundary conditions are specified along the boundary of the region of interest rather than along the lines dividing the space-charge region and the channel as in the gradual-channel approximation. Therefore, the effect of the gradual transition between the two regions for a device with small α will be seen in the final results. Furthermore, the final solution can be used to answer questions such as pinch-off of the channel and neutrality of the channel because nothing has been assumed for the electron concentration inside the device. Another merit of the boundary conditions given above is that the specification of the bias voltages is sufficient to determine the operation of the device.

In Chapter III, numerical methods of solving elliptic boundary value problems will be presented. In using these methods to solve equations (2.6) and (2.26), the mesh size must be chosen to ensure enough accuracy to the final solution. Since the potential varies as $\exp(-Y/L_{DE})$ in the transition region between the space-charge region and the neutral region, the mesh size should be smaller than or at most equal to L_{DE}.

$$h \lesssim L_{DE} = \frac{a}{\sqrt{2\alpha}} \tag{2.33}$$

If a constant mesh size is used for the whole region, the total number of mesh points M is

$$M \sim \frac{2aL_o}{h^2} \gtrsim 4\alpha \frac{L_o}{a} \tag{2.34}$$

The devices considered in Chapter IV have $\alpha = 50$. L_o/a is 10 for the long device and 4 for the short and the graded-channel device. Therefore, M is in the order of 1000. This large number of mesh points indicates the difficulty with the method in actual computation in that it requires a large storage space and long computing time.

II-3-b Continuity Equation

It has been found from experiences in numerical calculations that an integrated form of equation (2.7) is easier to handle than considering the equation as a differential equation. This approach is analogous to Gummel's treatment of quasi-Fermi levels for a one-dimensional bipolar transistor[20] and the discussion in this section can be regarded as an extension of Gummel's method to two-dimensional problems.

Because of the zero gate current, the total current crossing any plane, x = constant, is the same.

$$I_D = \frac{1}{\alpha} \int_{-1}^{1} e^{\Psi - \varphi_n} \mu_n \frac{\partial \varphi_n}{\partial x} \, dy \qquad (2.35)$$

$$= \text{constant}$$

From one-dimensional analyses, it is well known that, for a reverse biased P-N junction, quasi-Fermi levels can be treated as constant throughout the whole device with negligibly small error to the electro-static potential and the majority carrier concentrations. To find the degree of accuracy of this approximation a one-dimensional step P-N junction with

N_D = donor concentration of the N-region ($X \geq 0$)
$= 10^{15}$ atoms/cm^3

N_A = acceptor concentration of the P-region ($X \leq 0$)
$= 2 \times 10^{15}$ atoms/cm^3

$W_n = W_p = W$ = width of the N- and P-regions

= 1.852 Microns

V_{np} = applied reverse bias voltage

= 2.584 Volts

has been solved numerically both with and without the assumption of constant quasi-Fermi levels. Table 2.1 and 2.2 are the computer outputs of the solutions at some sample points. From the tables, we see that the electro-static potential is accurate to 3 significant figures for the whole device and that the majority carrier concentrations are accurate to 3 significant figures.

Since the gate junction of a JFET is always reverse biased and we are interested only in the potential and the majority carriers, the following approximation will be made:

$$\varphi_n = \varphi_n(x) \tag{2.36}$$

Note that this approximation is consistant with the zero gate current. Let

$$F(x) = \int_{-1}^{1} e^{\Psi} \mu_n \, dy = 2 \int_{0}^{1} e^{\Psi} \mu_n \, dy \tag{2.37}$$

APPROXIMATE SOLUTION

X/W	V/VT	QN/VT	QP/VT	N/ND	P/ND
-1.0	-61.8006	50.0000	-50.0000	4.1851D-54	2.0000D 00
-0.9	-61.8005	50.0000	-50.0000	4.1854D-54	1.9999D 00
-0.8	-61.8001	50.0000	-50.0000	4.1874D-54	1.9989D 00
-0.7	-61.7966	50.0000	-50.0000	4.2018D-54	1.9920D 00
-0.6	-61.7714	50.0000	-50.0000	4.3092D-54	1.9424D 00
-0.5	-61.5917	50.0000	-50.0000	5.1574D-54	1.6230D 00
-0.4	-60.5124	50.0000	-50.0000	1.5177D-53	5.5151D-01
-0.3	-56.6554	50.0000	-50.0000	7.1819D-52	1.1654D-02
-0.2	-48.8951	50.0000	-50.0000	1.6847D-48	4.9685D-06
-0.1	-37.1355	50.0000	-50.0000	2.1559D-43	3.8825D-11
0.0	-21.3762	50.0000	-50.0000	1.5059D-36	5.5582D-18
0.1	-4.3171	50.0000	-50.0000	3.8589D-29	2.1691D-25
0.2	10.7418	50.0000	-50.0000	1.3380D-22	6.2558D-32
0.3	23.8005	50.0000	-50.0000	6.2776D-17	1.3333D-37
0.4	34.8591	50.0000	-50.0000	3.9856D-12	2.1001D-42
0.5	43.9177	50.0000	-50.0000	3.4244D-08	2.4443D-46
0.6	50.9763	50.0000	-50.0000	3.9818D-05	2.1021D-49
0.7	56.0354	50.0000	-50.0000	6.2695D-03	1.3351D-51
0.8	59.1247	50.0000	-50.0000	1.3769D-01	6.0791D-53
0.9	60.5486	50.0000	-50.0000	5.7185D-01	1.4637D-53
1.0	61.1075	50.0000	-50.0000	1.0000D 00	8.3702D-54

V = ELECTRO-STATIC POTENTIAL
QN = QUASI-FERMI LEVEL FOR ELECTRONS
QP = QUASI-FERMI LEVEL FOR HOLES
N = ELECTRON CONCENTRATION
P = HOLE CONCENTRATION
VT = THERMAL VOLTAGE = 0.02584 VOLTS

TABLE 2.1

TRUE SOLUTION

X/W	V/VT	QN/VT	QP/VT	N/ND	P/ND
-1.0	-61.8006	-50.0000	-50.0000	1.1250D-10	2.0000D 00
-0.9	-61.8005	-49.8017	-50.0000	9.2273D-11	1.9999D 00
-0.8	-61.8001	-49.5542	-50.0000	7.2076D-11	1.9989D 00
-0.7	-61.7966	-49.2252	-50.0000	5.2044D-11	1.9921D 00
-0.6	-61.7714	-48.7383	-50.0000	3.2801D-11	1.9424D 00
-0.5	-61.5918	-47.8704	-50.0000	1.6479D-11	1.6231D 00
-0.4	-60.5129	-45.8916	-50.0000	6.7014D-12	5.5180D-01
-0.3	-56.6566	-41.2915	-50.0000	3.1849D-12	1.1669D-02
-0.2	-48.8969	-33.0623	-50.0000	1.9916D-12	4.9778D-06
-0.1	-37.1378	-20.9775	-49.6893	1.4380D-12	5.3095D-11
0.0	-21.3787	-4.9766	-35.5146	1.1291D-12	1.0888D-11
0.1	-4.3196	11.9674	-18.3756	1.2668D-12	1.1794D-11
0.2	10.7394	26.8908	-3.1860	1.4508D-12	1.3440D-11
0.3	23.7984	39.7922	10.0228	1.6985D-12	1.5612D-11
0.4	34.8573	49.5843	21.2573	6.0288D-12	1.8606D-11
0.5	43.9163	49.9999	30.5277	3.4198D-08	2.2988D-11
0.6	50.9752	50.0000	37.8517	3.9776D-05	2.9965D-11
0.7	56.0347	50.0000	43.2626	6.2653D-03	4.2583D-11
0.8	59.1244	50.0000	46.8443	1.3764D-01	6.9652D-11
0.9	60.5485	50.0000	48.8902	5.7180D-01	1.2971D-10
1.0	61.1075	50.0000	50.0000	1.0000D 00	2.2500D-10

V = ELECTRO-STATIC POTENTIAL
QN = QUASI-FERMI LEVEL FOR ELECTRONS
QP = QUASI-FERMI LEVEL FOR HOLES
N = ELECTRON CONCENTRATION
P = HOLE CONCENTRATION
VT = THERMAL VOLTAGE = 0.02584 VOLTS

TABLE 2.2

The second equality comes from the symmetry of the problem. The drain current can now be written as

$$I_D = \frac{1}{\alpha} e^{-\varphi_n(x)} F(x) \frac{d\varphi_n}{dx} \tag{2.38}$$

This can be readily integrated to give

$$e^{-\varphi_n(x)} = e^{-\varphi_n(\ell_o)} + \alpha I_D \int_x^{\ell_o} \frac{dx}{F(x)} \tag{2.39}$$

where

$$\ell_o = \frac{L_o}{a}$$

By putting $x = 0$ in equation (2.39), the drain current is expressed as

$$I_D = \frac{1}{\alpha} \frac{e^{-\varphi_n(0)} - e^{-\varphi_n(\ell_o)}}{\int_0^{\ell_o} \frac{dx}{F(x)}} \tag{2.40}$$

where $\varphi_n(0)$ and $\varphi_n(\ell_o)$ are determined by equations (2.36), (2.30), and (2.31):

$$\varphi_n(0) = \varphi_n(0,0) = \alpha V_{gs} \left(1 - \frac{V_B}{V_p}\right) + \alpha \frac{V_B}{V_p} \tag{2.41}$$

$$\varphi_n(\ell_o) = \varphi_n\left(\frac{L_o}{a},0\right) = \alpha V_{ds} \left(1 - \frac{V_B}{V_p}\right) + \varphi_n(0,0) \tag{2.42}$$

The major contribution to the integral in equation (2.40) comes from the source region where Y is small. As the drain-to-source bias voltage increases with a fixed source-to-gate voltage, space-charge region is formed near the drain and almost all the

potential drop occurs there. Therefore, the change in Ψ in the source region per unit change of the drain voltage decreases with increasing drain voltage which gives the decreasing differential drain conductance. This is similar to the operation of a bipolar transistor in common emitter configuration. When the base-to-emitter forward bias voltage is fixed, an increase of the collector-to-emitter voltage appears at the reverse biased collector junction leaving the potential distribution at the emitter junction unchanged. Since the collector current is controlled by the emitter junction, the collector current becomes saturated. The emitter and the collector junction in a bipolar transistor can be treated separately in normal bias conditions, i.e., before punch-through. In a unipolar transistor, however, the source and the drain regions interact with each other and the small change in the potential distribution in the source region with increasing drain voltage depends not only on the fixed gate-to-source bias voltage but also on the potential and charge distribution in the drain region. In fact, if the operation of a JFET is considered as the modulation of conductance between the source and the drain, the drain region with high resistivity is the controlling part.

An important factor in determining the differential drain conductance beyond pinch-off is the contraction of the size of the region which contributes significantly to the integral in equation (2.40). This is analogous to the Early effect[21] in

the bipolar transistors and is called "Channel Length Modulation" in the extended theory of the gradual-channel approximation.[22]

The effect of the variation of mobility with electric field can be seen in equations (2.37) and (2.40). The region near drain where the potential is high normally contributes insignificantly to the integral in equation (2.40). But in this region, the electric field is also high, giving smaller value for the mobility. This smaller mobility amplifies the effect of the region and decreases the drain current. This effect, however, depends on the magnitude of the electric field inside the device. If the dimension and bias voltages of the device are such that the electric field is in the thermal region, no effect of the field dependent mobility will be observed. This is the reason why devices with small length-to-width ratios can have both saturated and non-saturated drain characteristics.

Chapter III: NUMERICAL METHODS

In the first section of this chapter, the successive over-relaxation method of solving linear, elliptic boundary value problems and generalized Newton's method for nonlinear problems are presented. The presentation is restricted to two-dimensional space and is intended to give only the outline of the methods. For detailed discussions of these methods and for other methods of solving elliptic equations, the references[23-28] should be consulted. Numerical techniques of handling equations (2.39) and (2.40) together with the iteration scheme for the simultaneous solution of equations (2.6) and (2.39) constitute the second section.

III-1 Elliptic Boundary Value Problems

III-1-a Terminologies and Difference Equations

Let G be a bounded point set whose interior R is simply connected and whose boundary S is a contour. The set of points

$$\{(x+ph,y+qh) \mid p = 0,\pm1,\pm2, \ldots ; q = 0,\pm1,\pm2, \ldots\}$$

where (x,y) is an arbitrary point of G and h is a positive constant is called a set of planar grid points. Two such grid points are said to be adjacent if their distance apart is h. The set of all lines, each of which contains at least one pair of adjacent grid points, is called a planar lattice. Let G_h designate the set of points which are either planar grid points

in G or are points of intersection of S and the planar lattice. If a point is an element of $S \cap G_h$, then the point is called a boundary lattice point, and the set of all boundary lattice points is written S_h. The set of all points of G_h which are not elements of S_h is called the set of interior lattice points and is written R_h.

Let $F(x,y,t,p,q) \in C^1$ for all $(x,y) \in R$ and for all real t,p, and q. If for all t

$$\frac{\partial F}{\partial t} \geq 0$$

and for all p and q there exists a constant A such that

$$\left|\frac{\partial F}{\partial p}\right| , \left|\frac{\partial F}{\partial q}\right| \leq A$$

then the elliptic equation

$$\frac{\partial^2 u}{\partial x^2} + \frac{\partial^2 u}{\partial y^2} = F\left(x,y,u,\frac{\partial u}{\partial x},\frac{\partial u}{\partial y}\right) \tag{3.1}$$

is said to be mildly nonlinear on R. A linear elliptic equation will be considered as a special form of a mildly nonlinear equation. Let $\phi(x,y) \in C(S)$. Then a mildly nonlinear Dirichlet problem is that of finding u(x,y) which satisfies the three conditions:

(a) u is a solution of equation (3.1) on R

(b) $u \equiv \phi$ on S

(c) $u \in \left[C^2(R) \cap C(G)\right]$

The fact that a mildly nonlinear Dirichlet problem has a unique solution has been established.[29]

The problems of solving equations (2.6) and (2.26) subject to the given boundary conditions are mildly nonlinear Dirichlet problems. Since these equations do not have any first order term, the discussion from now on will be restricted to equations of the form

$$\frac{\partial^2 u}{\partial x^2} + \frac{\partial^2 u}{\partial y^2} = F(x,y,u) \tag{3.2}$$

The fundamental approach of the finite difference method is to replace the differential equation by a difference equation and the point set G by G_h. For this purpose, let points (x,y), $(x+h,y)$, $(x,y+h)$, $(x-h,y)$, and $(x,y-h)$ be denoted by double subscripts (i,j), $(i+1,j)$, $(i,j+1)$, $(i-1,j)$, and $(i,j-1)$ respectively. Let $u(x,y)$ and $F(x,y,u)$ at a point (i,j) be denoted by $u_{i,j}$ and $F_{i,j}$. We try to determine parameters a_ℓ, $\ell = 0, 1, 2, 3, 4$ such that at (x,y)

$$\frac{\partial^2 u}{\partial x^2} + \frac{\partial^2 u}{\partial y^2} = a_0 u_{i,j} + a_1 u_{i+1,j} + a_2 u_{i,j+1} + a_3 u_{i-1,j} + a_4 u_{i,j-1} \tag{3.3}$$

Using the Taylor expansions about (x,y)

$$a_0 u_{i,j} + a_1 u_{i+1,j} + a_2 u_{i,j+1} + a_3 u_{i-1,j} + a_4 u_{i,j-1}$$

$$= \sum_{\ell=0}^{4} (a_\ell)\, u_{i,j} + h(a_1 - a_3) \frac{\partial u}{\partial x} + h(a_2 - a_4) \frac{\partial u}{\partial y} \qquad (3.4)$$

$$+ \frac{h^2}{2} (a_1 + a_3) \frac{\partial^2 u}{\partial x^2} + \frac{h^2}{2} (a_2 + a_4) \frac{\partial^2 u}{\partial y^2} + \sum O(h^3)$$

Comparing equations (3.3) and (3.4), we obtain

$$a_0 = -\frac{4}{h^2}$$

$$a_1 = a_2 = a_3 = a_4 = \frac{1}{h^2} \qquad (3.5)$$

The substitution of equation (3.5) back into equation (3.4) gives

$$\frac{\partial^2 u}{\partial x^2} + \frac{\partial^2 u}{\partial y^2} = \frac{1}{h^2} \left[u_{i+1,j} + u_{i,j+1} + u_{i-1,j} + u_{i,j-1} - 4u_{i,j} \right] + O(h) \qquad (3.6)$$

Elimination of the term O(h) in equation (3.6) gives a difference equation approximation of equation (3.2)

$$U_{i+1,j} + U_{i,j+1} + U_{i-1,j} + U_{i,j-1} - 4U_{i,j} + h^2 F_{i,j} = 0 \qquad (3.7)$$

where $U_{i,j}$ is an approximation of $u_{i,j}$. This particular difference scheme is known as five-point difference analogue.*

---

* For other difference schemes, see reference 28.

A numerical method of solving equation (3.2) will now be presented.

Step 1. For fixed $h \geq 0$ and fixed (x,y) in R, construct G_h, R_h, and S_h.

Step 2. Suppose R_h consists of m points and S_h of n points. Number the points of R_h with the integers 1 through m in such a way that the numbers are increasing from left to right on any horizontal line of the lattice and increasing from bottom to top on any vertical line. Number the points of S_h with the integers $m+1, m+2, \ldots, m+n$.

Step 3. At each point (x,y) of S_h, set $U(x,y) = \phi(x,y)$. If the point (x,y) is numbered K, this is equivalent to $U_K = \phi(x,y)$.

Step 4. At each point (x,y) of R_h, write the difference analogue of equation (3.2). This gives a system of m equations in m unknowns.

Step 5. Solve the system of equations generated in Step 4.

The problem has now been reduced to that of solving a system of equations. It can be shown that the system of equations generated from an equation of the form of (3.2) has a unique solution and that the solution approaches that of the differential equation as h approaches zero.[26]

III-1-b Linear Equations

When equation (3.2) is linear, it can be written as

$$\frac{\partial^2 u}{\partial x^2} + \frac{\partial^2 u}{\partial y^2} - f(x,y)\, u = g(x,y) \qquad (3.8)$$

where $f(x,y) \geq 0$ for all points in R. Using the same subscripts as those in equation (3.7), the five-point difference analogue of equation (3.8) is

$$U_{i+1,j} + U_{i,j+1} + U_{i-1,j} + U_{i,j-1} - (4+h^2 f_{i,j})\, U_{i,j} = h^2 g_{i,j} \qquad (3.9)$$

For a fixed ω, $1 < \omega < 2$, the successive overrelaxation method is defined by the following iteration scheme.[23]

$$U_{i,j}^{(t+1)} = U_{i,j}^{(t)} + \omega \frac{U_{i+1,j}^{(t)} + U_{i,j+1}^{(t)} + U_{i-1,j}^{(t+1)} + U_{i,j-1}^{(t+1)} - (4+h^2 f_{i,j})\, U_{i,j}^{(t)} - h^2 g_{i,j}}{4 + h^2 f_{i,j}} \qquad (3.10)$$

where the superscripts are iteration indices. The order of application of equation (3.10) to each point of R_h is the same as the ordering of points in Step 2.

The appearance of superscript (t+1) on the right hand side of equation (3.10), when combined with the ordering of the computation, implies that the improved values are used as soon as they are computed. It is clear that the ordering of computation

is an important factor determining the convergence of the method. More rapid convergence can be realized with consistent orderings.[23,24,27] For a five-point difference equation, an example of the consistent ordering is that defined in Step 2. In the discussions to follow, we will always assume a consistent ordering.

To study the convergence property of the method, we write the system of linear equations generated in Step 4 as a matrix equation.

$$A\underline{U} = \underline{k} \tag{3.11}$$

where $\underline{U}$ is the column vector with $U_1, U_2, \ldots, U_m$ as its elements. Note that the boundary conditions are included in the column vector $\underline{k}$. From equation (3.9), we observe that the matrix A is symmetric if every point of G_h is an element of the set

$$\{(x+ph,y+qh) \mid p = 0,\pm1,\pm2, \ldots ; q = 0,\pm1,\pm2, \ldots ; (x,y) \in R\}$$

Suppose we paint the points of G_h with two different colors such that the points of every pair of adjacent grid points have different colors.[25] Then it is easy to see that, by reordering the points of R_h, A can be changed into

$$A = \begin{bmatrix} A_{1,1} & A_{1,2} \\ A_{2,1} & A_{2,2} \end{bmatrix}$$

where $A_{1,1}$ and $A_{2,2}$ are diagonal matrices.

Such a matrix is said to have "Property(A)".[23] In the following discussions, it will be assumed that the matrix A is real, symmetric, positive definite and has Property(A).

Let us subdivide A into three matrices

$$A = B - P - P^T \tag{3.12}$$

where

$$B = \begin{bmatrix} a_{1,1} & & & 0 \\ & a_{2,2} & & \\ & & \ddots & \\ 0 & & & a_{m,m} \end{bmatrix}$$

$$P = \begin{bmatrix} 0 & & & 0 \\ -a_{2,1} & 0 & & \\ -a_{3,1} & -a_{3,2} & 0 & \\ \vdots & \vdots & & \ddots \\ -a_{m,1} & -a_{m,2} & & 0 \end{bmatrix}$$

The method of simultaneous displacements is defined by

$$\underline{u}^{(t+1)} = B^{-1}(P + P^T)\underline{u}^{(t)} + \underline{k} \tag{3.13}$$

Let

$$\underline{u}^{(t)} = \underline{u} + \underline{e}^{(t)}$$

$$M_B = B^{-1}(P + P^T)$$

$\underline{e}^{(t)}$ is the error vector after the t^{th} iteration. The successive

error vectors are related by

$$\underline{e}^{(t+1)} = M_B \underline{e}^{(t)} = M_B{}^t \underline{e}^{(o)} \tag{3.14}$$

It can be seen from equation (3.14) that $\underline{u}^{(t)}$ converges to $\underline{u}$ independent of $\underline{u}^{(o)}$ if the spectral norm (the maximum of the moduli of eigenvalues) of M_B, $\bar{\lambda}$, is less than unity, i.e.,

$$\bar{\lambda} \leq 1 \tag{3.15}$$

Moreover, the convergence is faster if $\bar{\lambda}$ is smaller. For the difference equations derived from an elliptic partial differential equation of the form (3.2), equation (3.15) holds independent of h.[26,27]

The successive overrelaxation method defined in equation (3.10), when written as a matrix equation, is

$$\underline{u}^{(t+1)} = \underline{u}^{(t)} + \omega \left[B^{-1} \left(P\underline{u}^{(t+1)} + P^T \underline{u}^{(t)} + \underline{k} \right) - \underline{u}^{(t)} \right] \tag{3.16}$$

The error after t iterations is

$$\underline{e}^{(t)} = L_\omega \, \underline{e}^{(t-1)} = L_\omega^t \, \underline{e}^{(o)} \tag{3.17}$$

where

$$L_\omega = (I - \omega B^{-1} P) \left\{ (1-\omega) I + \omega B^{-1} P^T \right\} \tag{3.18}$$

It can be shown that successive overrelaxation method converges to $\underline{u}$ independent of $\underline{u}^{(o)}$ if the method of simultaneous displacements

converges.[23] Let the eigenvalues and eigenvectors of L_ω be denoted by η_i and $\underline{y}_i$, i.e.,

$$L_\omega \underline{y}_i = \eta_i \underline{y}_i \qquad i = 1,2, \ldots , m \tag{3.19}$$

Let η_1 be the eigenvalue with the largest modulus. Expanding $\underline{e}^{(o)}$ in terms of the eigenvectors $\underline{y}_i$ and substituting it into equation (3.17), we obtain

$$\begin{aligned} \underline{e}^{(t)} &= L_\omega{}^t \sum_{i=1}^{m} a_i \underline{y}_i \\ &= \sum_{i=1}^{m} a_i \eta_i{}^t \underline{y}_i \\ &= \eta_1{}^t \sum_{i=1}^{m} a_i \left(\frac{\eta_i}{\eta_1}\right)^t \underline{y}_i \end{aligned} \tag{3.20}$$

As t increases the eigenvectors with eigenvalues smaller than η_1 damp out with respect to $\underline{y}_1$.

$$\underline{e}^{(t)} \longrightarrow \eta_1{}^t a_1 \underline{y}_1 \tag{3.21}$$

If $\omega \neq 0$, a nonzero eigenvalue of L_ω, η, is related to an eigenvalue of M_B, λ, by[23,24,27]

$$(\eta + \omega - 1)^2 = \omega^2 \lambda^2 \eta \tag{3.22}$$

The optimum relaxation factor ω_b, for which the spectral norm of L_ω is the smallest, is found from equation (3.22).

$$\omega_b = 1 + \left[\frac{\bar{\lambda}}{1+\sqrt{1-\bar{\lambda}^2}}\right]^2 \tag{3.23}$$

To find ω_b numerically,[27] we choose ω_o which is less than an anticipated ω_b. (For example $\omega_o = 1.$) Iterate with successive overrelaxation with $\omega = \omega_o$. The convergence rate is measured in terms of

$$\frac{\delta^{(t)}}{\delta^{(t-1)}} = \frac{\left[\|\underline{u}^{(t)} - \underline{u}^{(t-1)}\|\right]^2}{\left[\|\underline{u}^{(t-1)} - \underline{u}^{(t-2)}\|\right]^2} = \frac{\left[\|\underline{e}^{(t)} - \underline{e}^{(t-1)}\|\right]^2}{\left[\|\underline{e}^{(t-1)} - \underline{e}^{(t-2)}\|\right]^2} \tag{3.24}$$

where $\|\ \|$ indicates the Euclidean length of a vector. Using equation (3.21), we obtain

$$\frac{\delta^{(t)}}{\delta^{(t-1)}} \longrightarrow \eta_{1,\omega_o}^2 \tag{3.25}$$

The spectral norm of M_B can now be evaluated from equation (3.22).

$$\bar{\lambda} = \frac{(\eta_{1,\omega_o} + \omega_o - 1)}{\omega_o\ \eta_{1,\omega_o}^{1/2}} \tag{3.26}$$

ω_b is then computed by equation (3.23).

III-1-c Nonlinear Equations

If equation (3.2) is nonlinear, the system of equations generated in Step 4 is also nonlinear.

$$f_i(u_1, u_2, \ldots, u_m) = 0 \qquad i = 1,2, \ldots, m \tag{3.27}$$

Let $f_{ii} \equiv \frac{\partial f_i}{\partial u_i} \neq 0$. Then for a fixed, real constant ω, the generalized Newton's method is defined by the following iteration scheme.[26]

$$u_1^{(t+1)} = u_1^{(t)} - \omega \frac{f_1(u_1^{(t)}, u_2^{(t)}, \ldots, u_m^{(t)})}{f_{11}(u_1^{(t)}, u_2^{(t)}, \ldots, u_m^{(t)})}$$

$$u_2^{(t+1)} = u_2^{(t)} - \omega \frac{f_2(u_1^{(t+1)}, u_2^{(t)}, \ldots, u_m^{(t)})}{f_{22}(u_1^{(t+1)}, u_2^{(t)}, \ldots, u_m^{(t)})} \tag{3.28}$$

$$u_m^{(t+1)} = u_m^{(t)} - \omega \frac{f_m(u_1^{(t+1)}, u_2^{(t+1)}, \ldots, u_{m-1}^{(t+1)}, u_m^{(t)})}{f_{mm}(u_1^{(t+1)}, u_2^{(t+1)}, \ldots, u_{m-1}^{(t+1)}, u_m^{(t)})}$$

where $\underline{u}^{(o)}$ is the initial approximation. Note that this iteration scheme reduces to successive overrelaxation method for a linear case. The generalized Newton's method has been used successfully to solve equation (2.6) with ω determined by the same process as in the linear case and with arbitrary initial approximation. This solution may be used as the starting approximation, Ψ_a, of equation (2.26).

III-2 Integration Technique and Simultaneous Solution

Due to the large magnitudes of the bias voltages of a JFET, the electro-static potential varies over such a wide range that the integrands in equations (2.37), (2.39), and (2.40) become larger than the largest number which can be handled in most digital computers.[30] This difficulty can be removed by dividing the interval of integration into smaller subintervals and choosing appropriate reference levels for the subintervals.

Let

$$\xi(x) = - \ln \int_{-1}^{1} e^{\Psi(x,y)-\Psi(x,0)} \mu_n \, dy \tag{3.29}$$

$F(x)$ defined in equation (2.37) and $\xi(x)$ are related by

$$F(x) = e^{\Psi(x,0)-\xi(x)} \tag{3.30}$$

Since $\Psi(x,y) - \Psi(x,0) \leq 0$ for $-1 \leq y \leq 1$, the integral in equation (3.29) can be handled by a computer.

Let the interval $0 \leq x \leq \ell_o$ be divided into M subintervals T_i, $i = 1, 2, 3, \ldots, M$.

$$\begin{aligned} T_1 &= \{x \mid 0 \leq x \leq x_1\} \\ T_i &= \{x \mid x_{i-1} < x \leq x_i\} \quad i = 2,3, \ldots, M \end{aligned} \tag{3.31}$$

where

$$0 < x_1 < x_2 < \cdots < x_M = \ell_o .$$

Let also QN_i be the reference level for φ_n in the interval T_i. When T_i and QN_i are chosen appropriately, the integral

$$\int_{x_{i-1}}^{x_i} \exp\left[-\Psi(t,0) + QN_i + \xi(t)\right] dt \quad i = 1,2, \ldots, M$$

can be evaluated without any difficulty. Let

$$W(x) = \int_{x}^{\ell_o} \exp\left[-\Psi(t,0) + QN_i + \xi(t)\right] dt \quad x \in T_i \tag{3.32}$$

In terms of $W(x)$, $\varphi_n(x)$ and I_D are

$$\varphi_n(x) = QN_i - \ln\left[e^{-\varphi_n(\ell_o)+QN_i} + \alpha I_D W(x)\right] \quad x \in T_i \tag{3.33}$$

$$I_D = \frac{1}{\alpha} \frac{e^{-\varphi_n(o)+QN_1} - e^{-\varphi_n(\ell_o)+QN_1}}{W(o)} \tag{3.34}$$

If the integrand of equation (3.29) is written as

$$\exp\left[\Psi(x,y) - \Psi(x,o) + \ln \mu_n\right]$$

it is of the same functional form as the integrand of equation (3.32). Therefore only one subroutine is necessary for the integrations. The integration by Gaussian quadrature with the argument of the exponential function approximated by a quadratic function has been used.

The dependence of the drift velocity on the electric field, E, is usually described by[7]

$$v \propto E \qquad E \leq E_{c1} \qquad \text{(Thermal)}$$

$$v \propto E^{1/2} \qquad E_{c1} \leq E \leq E_{c2} \qquad \text{(Tepid)}$$

$$v = v_s \qquad E_{c2} \leq E \qquad \text{(Hot)}$$

where v_s is the saturation velocity and E_{c1} and E_{c2} are two critical fields. Their values for n-type silicon are E_{c1} = 2.5 Kv/cm and E_{c2} = 15 Kv/cm. A somewhat simpler description has been proposed by Denda and Nicolet[31] which contains only one critical field and gives the drift velocity for the whole range of electric field by a single function.

$$v = v_s(1 - e^{-E/E_c}) \tag{3.35}$$

For a small electric field, equation (3.35) can be approximated by

$$v = v_s \frac{E}{E_c} \tag{3.36}$$

which gives

$$\mu_{no} = \frac{v_s}{E_c} \tag{3.37}$$

When the experimental results[32,33] for v_s and μ_{no}

$$v_s = 1.05 \times 10^7 \text{ cm/sec}$$

$$\mu_{no} = 1350 \text{ cm}^2/\text{Volt-sec}$$

are used in equation (3.37), E_c has the value between E_{c1} and E_{c2}.

$$E_c = 7.77 \text{ Kv/cm}$$

The normalized electron mobility, μ_n, is obtained from equation (3.35) by dividing it with the electric field.

$$\mu_n = \frac{1 - e^{-E/E_c}}{E/E_c} \tag{3.38}$$

A revised form of equation (3.38) suitable for the machine calculation

$$\begin{aligned} \mu_n &= 1 - \frac{1}{2}\frac{E}{E_c} && E/E_c < 10^{-4} \\ \mu_n &= \frac{1 - e^{-E/E_c}}{E/E_c} && E/E_c \geq 10^{-4} \end{aligned} \tag{3.39}$$

will be used in actual computation.

We now describe the iterative method to solve equations (2.6) and (2.39) simultaneously. The variations of the two equations, which are to be used in the computation, are collected here for convenient references.

$$\nabla^2 \Psi = - 2\alpha \left[N(x,y) - e^{\Psi - \varphi_n} \right] \tag{3.40}$$

$$\nabla^2 \delta\Psi - 2\alpha\, e^{\Psi_a - \varphi_n}\, \delta\Psi = - \nabla^2 \Psi_a - 2\alpha \left[N(x,y) - e^{\Psi_a - \varphi_n} \right] \tag{3.41}$$

$$\Psi = \Psi_a + \delta\Psi \tag{3.42}$$

$$\varphi_n(x) = QN_i - \ln\left[e^{-\varphi_n(\ell_o)+QN_i} + \alpha I_D\, W(x)\right] \quad x \in T_i \tag{3.43}$$

$$I_D = \frac{1}{\alpha}\,\frac{e^{-\varphi_n(o)+QN_1} - e^{-\varphi_n(\ell_o)+QN_1}}{W(o)} \tag{3.44}$$

$$W(x) = \int_x^{\ell_o} \exp\left[-\Psi(t,o) + QN_i + \xi(t)\right] dt \quad x \in T_i \tag{3.45}$$

$$\xi(x) = -\ln \int_{-1}^{1} \exp\left[\Psi(x,y) - \Psi(x,o) + \ln \mu_n\right] dy \tag{3.46}$$

The first step is to obtain the boundary conditions by solving equation (3.40) one-dimensionally along $X = 0$ and $X = L_o$ as discussed in section III-3-a using the generalized Newton's method. The iteration of this method is terminated when

$$\underset{(x,y)\in R_n}{\text{Max}} \left|\Psi^{(t)} - \Psi^{(t-1)}\right| < \text{EPSB}$$

where EPSB is a small constant to be determined from the nature of the problem.

The overall iteration scheme starts from a guess of the quasi-Fermi level for electrons, $\varphi_n^{(o)}(x)$. This is used to

determine the sizes of the subintervals and the reference levels. Equation (3.40) is then solved for Ψ with $\varphi_n = \varphi_n^{(o)}$ by the generalized Newton's method. Let the solution be denoted by $\Psi^{(1)}$. An improved solution for φ_n, $\varphi_n^{(1)}$, and the drain current $I_D^{(1)}$ are computed using equations (3.43) - (3.46) with $\Psi = \Psi^{(1)}$. By solving equation (3.41) for $\delta\Psi$ by successive overrelaxation method with $\varphi_n = \varphi_n^{(1)}$ and $\Psi_a = \Psi^{(1)}$, the improved electro-static potential $\Psi^{(2)}$ is obtained from equation (3.42). $\varphi_n^{(2)}$ and $I_D^{(2)}$ are then computed from $\Psi^{(2)}$. The above iteration scheme can be summarized as follows.

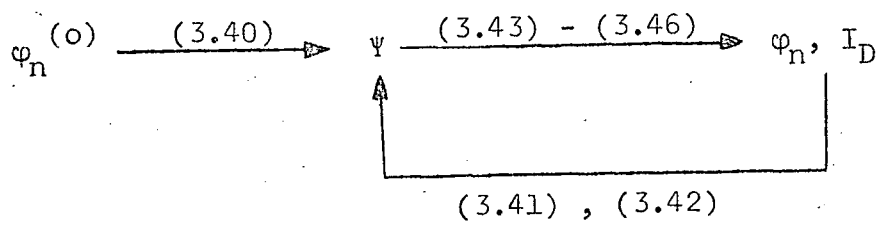

Note that there are two kinds of iterations in this process, i.e., one for solving equation (3.40) or (3.41) and the other for the overall solution. The former may be called as 'inner iteration' while the latter as 'outer iteration'. Let t and k denote the iteration indices for the inner and outer iterations respectively. Let

$$EER^{(t)} = \max_{(x,y)\in R_n} \left| \delta\psi^{(t)} - \delta\psi^{(t-1)} \right|$$

$$DMAX^{(t)} = \max_{(x,y)\in R_n} \left| \delta\psi^{(t)} \right|$$

$$RMAX^{(k)} = \max_{(x,y)\in R_n} \left| \frac{-\nabla^2\psi^{(k)} - 2\alpha\left[N(x,y) - e^{\psi^{(k)}-\varphi_n^{(k)}}\right]}{2\alpha\, N(x,y)} \right|$$

The following conditions are used to terminate the various iterations.

$$\max_{(x,y)\in R_n} \left| \psi^{(t)} - \psi^{(t-1)} \right| < EPSI \quad \text{for (3.40)}$$

$$EER^{(t)} / DMAX^{(t)} < EPSD \quad \text{for (3.41)}$$

$$RMAX^{(k)} < EPS \quad \text{for outer iteration}$$

where EPSI, EPSD, and EPS are some specified small constants.

Because ψ is normalized by kT/q, $|\psi|$ is in the order of $\alpha = \frac{V_p}{kT/q}$. The devices considered in Chapter IV have $\alpha = 50$. From these considerations, EPSB and EPSI are chosen as

$$EPSB = 10^{-4}$$

$$EPSI = 5 \times 10^{-3}$$

Since the boundary conditions require more accuracy, a smaller

number has been given for EPSB. EPSD is a measure of the relative accuracy and

$$EPSD = 10^{-2}$$

is used. The accuracy of the final solution is determined by EPS and the choice of EPSD is somewhat arbitrary. The value of EPS may be chosen by observing the convergence of the drain current. Fig. 3.1 shows the convergence of $I_D^{(k)}$ and the reduction of $RMAX^{(k)}$ for the short device considered in Chapter IV with $V_{gs} = 0$ and $V_{ds} = 1$. $\varphi_n^{(o)}$ for this example is

$$\varphi_n^{(o)}(x) = \varphi_n^{(o)} + [\varphi_n(\ell_o) - \varphi_n(o)] \frac{x}{\ell_o}$$

From the figure, we see that

$$EPS = 10^{-3}$$

may be used for this example. From similar considerations, the above value of EPS has been found to be useful for the devices in Chapter IV and V.

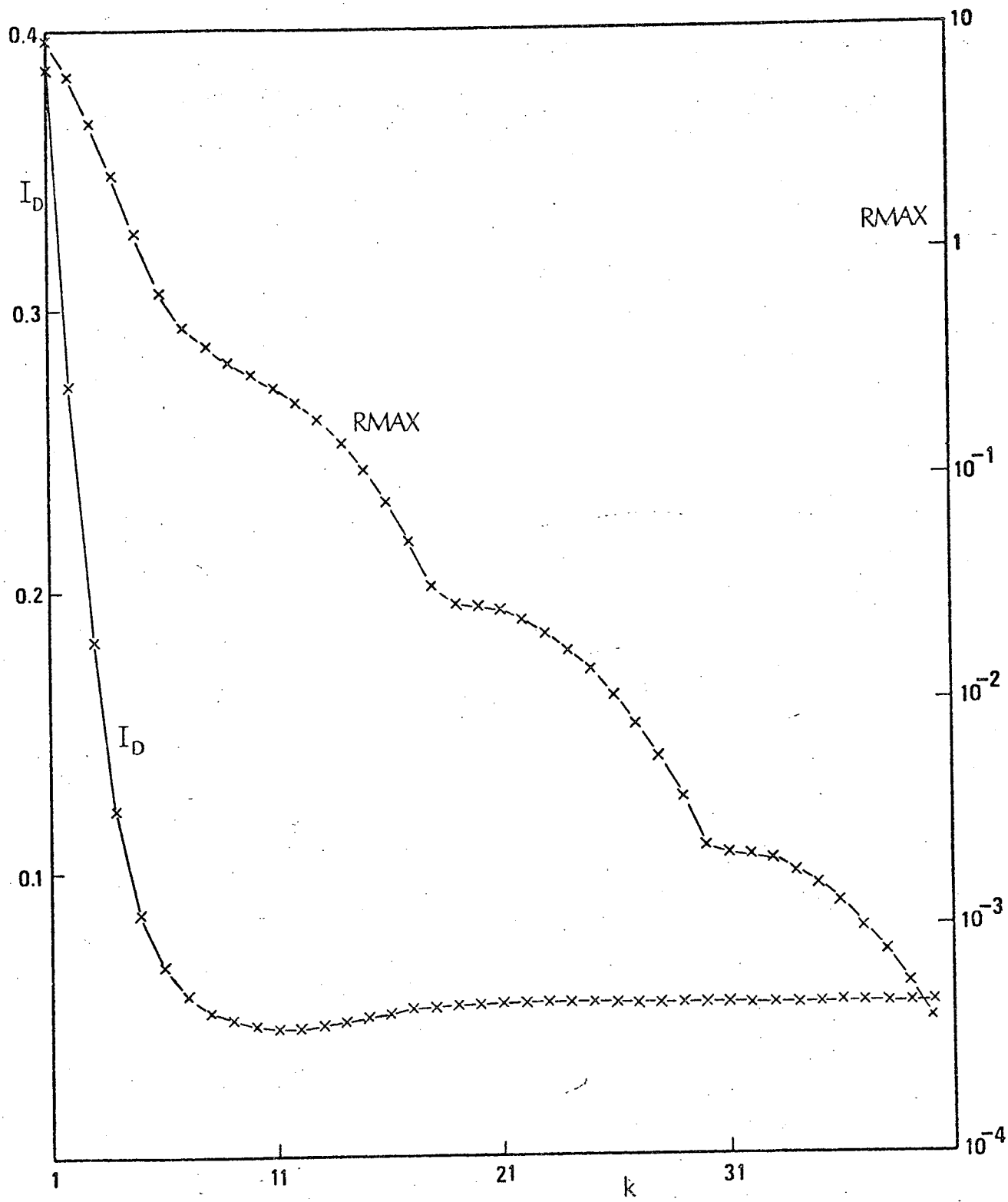

Figure 3.1 Convergence of the Drain Current and Reduction of RMAX with Outer Iteration

Chapter IV: DEVICES WITH UNIFORM AND NON-UNIFORM DOPING PROFILE IN THE CHANNEL

The method developed has been applied to two silicon devices with uniform doping profile in the channel and the same α but different L/a ratios. The parameters of these two devices are

N_D = donor concentration of the N-region
$= 10^{15}$ atoms/cm^3

N_D^+ = donor concentration at the source and the drain contacts $= 5 \times 10^{15}$ atoms/cm^3

N_A = acceptor concentration of the P-region
$= 10^{17}$ atoms/cm^3

$\alpha = 50$

$L/a = 2, 8$

The device with L/a = 2 will be referred to as 'short device' while the one with L/a = 8 as 'long device'. Another device with the same parameters as the short device but with non-uniform doping profile along the channel is also considered. This device will be called the 'graded-channel device'. V_p and a for these devices are computed by

$$V_p = \alpha \frac{kT}{q} = 1.293 \text{ Volts}$$

$$a = \sqrt{\frac{2\epsilon\epsilon_o V_p}{qN_D}} = 1.310 \text{ Microns}$$

The small value of α and the low doping level in N^+-regions have been chosen mainly for the simplicity of the numerical computation and reasonable computing time.* More realistic values may be chosen at the cost of these factors. For the short and the long device, a constant mesh size equal to half of the intrinsic Debye length in the N-region is used for all bias conditions. This mesh size is 1.11 times the extrinsic Debye length in the N^+-regions. The mesh size for the graded-channel device has been chosen to be one third of the extrinsic Debye length in the N-region. Since the size of the N^+-region at the source contact is larger for the graded-channel device (see Fig. 4.16), a smaller mesh size than the short and the long device is necessary. The mesh size chosen is equal to 0.745 times the extrinsic Debye length in the N^+-regions.

The computation has been carried out on the IBM System 360/91. The program has been written in FORTRAN IV and compiled by the FORTRAN G compiler. When the mesh sizes are chosen as discussed above, the total memory requirements are approximately 250K bytes for the long and the graded-channel device and 150K bytes for the short device. The computing time depends on the

---

* Larger α requires more storage space and computing time. Higher doping level in N^+-regions requires the use of different mesh sizes in N- and N^+-regions.

rate of convergence of the iteration schemes and the first approximation of the quasi-Fermi level for electrons. It has been observed that the convergence is faster for a smaller drain current. For the example shown in Fig. 3.1, the CPU time is about 3 minutes.

The accuracy of the results has been tested by solving the short device with $V_{gs} = 0$ and $V_{ds} = 3$ with the mesh size equal to that of the graded-channel device, i.e., with the mesh size reduced by 2/3. The difference between the two results is less than 1%. The choice of the mesh size, therefore, is considered to be appropriate.

IV-1 Devices with Uniform Doping Profiles

Fig. 4.1 shows the distribution of the donor concentration for the short device with the precise definition of L to be used for the L/a ratios. As can be seen in the figure, the source and the drain N^+-regions are excluded in the definition of L so that L is the length of the N-region. Except for larger L, the donor distribution is the same for the long device.

In Figs. 4.2 through 4.25, the signs and the normalization constant of the bias voltages are the same as in equations (2.30) and (2.31). The electro-static potential, and the electron density are normalized by V_p and N_D respectively.

Figs. 4.2 and 4.3 are the drain characteristics for the short and the long device respectively. In these figures, the drain current is normalized by Shcokley's saturation current. The results of the gradual-channel approximation are shown by the dashed curves for comparison. The source and the drain resistance have been included in the gradual-channel approximation by matching the slope of the two curves at the origin. The computed results are significantly different from the result of the gradual-channel approximation in the saturation region. The reason for this difference can be seen most clearly in Figs. 4.8-a and 4.14-a which show the electron concentrations on the X-axis for the short and the long device respectively for the bias conditions $V_{gs} = 0$, and $V_{ds} = 3$. The minima of electron concentration in these figures are $n = 0.632$ for the short device and $n = 0.168$

for the long device. Since the bias condition is well beyond the pinch-off point, the minimum of the electron concentration on the X-axis predicted by the gradual-channel approximation is negligibly small. This significant departure from the gradual-channel approximation regarding the electron concentration appears in the drain characteristics as non-zero differential drain conductance. It can also be seen that the gradual-channel approximation is a better approximation for the long device than for the short device regarding not only the drain characteristics but also the distribution of the electron concentration.

The maximum of electric fields in X-direction for the bias conditions considered before are 12.3 Kv/cm for the short device and 11.2 Kv/cm for the long device. Therefore, the drift velocity of the electrons is not saturated completely for both devices but is in the tepid region. Consequently, the saturation of the drift velocity is not the dominant factor in determining the drain characteristics of these devices. As compared to the long device, the larger differential conductance for the short device is due to the smaller L/a ratio.

Comparing Fig. 4.7 with Figs. 4.5 and 4.9 we see that the potential distribution is almost unchanged in the source region as the drain bias voltage is increased. It is more apparent for the long device as can be seen in Figs. 4.13 and 4.15. This is a well known fact and is the cause of the saturation of the drain current. (See equation (2.40).)

The effect of the bias voltages to the distribution of the electron concentration can be seen in Figs. 4.4, 4.6, 4.8, and 4.10 for the short device and in Figs. 4.12 and 4.14 for the long device. The first point to be noted is that the transition from the space-charge region to the conductive channel is not abrupt. In order to facilitate the discussion, we define the 'channel' as the portion of the region surrounded by the source, drain, and gate where the free carrier concentration is greater than half of the impurity concentration of that region. Therefore, the maximum possible channel length is L and the maximum possible channel width is 2a. (See Fig. 4.1.) Table 4.1 gives the minimum channel width and channel length for both the short and the long device at various bias conditions. In this table, the channel length modulation can be seen clearly. It can also be seen that, for the short device, the channel is not pinched-off, i.e., the channel length is L, for $V_{gs} = 0$ and $V_{ds} \leq 3$. The zero channel width in this table only means that the electron concentration becomes less than $0.5N_D$ along the X-axis and does not mean the total depletion of the electrons. From Figs. 4.8, 4.10, 4.12, and 4.14, we see that there is always a conduction path with appreciable electron concentration connecting the source and the drain contacts. In Figs. 4.8, 4.10, and 4.14, the electron concentration in the drain N^+-region is significantly smaller than that of the thermal equilibrium condition. This indicates the space-charge region in the drain N^+-region.

V_{ds} \ V_{gs}	0.0	0.5	1.0
1.0	0.220a / 2a	0 / 1.16a	0 / 0
2.0	0.126a / 2a	0 / 1.07a	0 / 0
3.0	0.110a / 2a	0 / 1.05a	0 / 0

Table 4.1-a Minimum channel width/channel length for the short device

V_{ds} \ V_{gs}	0.0	0.5	1.0
1.0	0 / 7.07a	0 / 4.09a	0 / 0
2.0	0 / 6.49a	0 / 3.80a	0 / 0
3.0	0 / 6.25a	0 / 3.69a	0 / 0

Table 4.1-b Minimum channel width/channel length for the long device

This space-charge region is particularly important for the model chosen here because of the large potential drop in the region. If there were no space charge in the drain N^+-region, complete depletion of electrons near drain would be necessary to support the large drain potential. This result is the consequence of including the N^+-regions in the analysis.

The effect of the gate bias voltage can be seen by comparing Figs. 4.8 and 4.9 with Figs. 4.10 and 4.11. The channel width and the electron concentration decrease uniformly from the source to the drain with increasing gate bias voltage. In fact, the operation of a JFET with a non-zero gate voltage can be interpreted as the operation of another JFET with correspondingly smaller a and zero gate voltage.

The major advantage of the present method is that it gives the potential distribution and the free carrier distribution directly from the geometry of the device and the bias conditions without any intermediate assumptions. The method, therefore, can be used to explain the conflicting descriptions of the channel shape after pinch-off. According to Wu and Sah[6], the channel is essentially neutral and completely pinched-off when the drain voltage is greater than the pinch-off voltage. The finite differential drain conductance is attributed to the channel length modulation. Hauser[14], on the other hand, assumed a minimum channel width of the order of $2L_{DE}$ at pinch-off. Further increase in drain voltage decreases the free carrier concentration in the

channel. The results of the present analysis are in general agreement with Hauser's qualitative description. The results also show that the neutrality and the complete pinch-off of the channel are not strictly accurate. They can, however, be regarded as first order approximations and the channel length modulation can be seen with a proper definition of the channel.

It has been found that the saturation of the drift velocity has not occurred for the particular model chosen and for the bias conditions considered. By noting the poor saturation of the drain current of the short device, we can conclude that a good saturation of the drain current of a short device is due to the drift velocity saturation.

The computed drain characteristics shown in Figs. 4.2 and 4.3 are now compared with the experimental measurements in terms of the differential drain resistances. The test units are 2N3459 from Siliconix Incorporated. The values of the parameters for these devices are

$$V_p = 2.7 \text{ Volts}$$

$$V_B = 0.7 \text{ Volts}$$

$$L \sim 5.1 \text{ Microns}$$

$$a \sim 0.8 \text{ Microns}$$

From these data, we find

$$L/a \sim 6.4$$

$$V_B/V_p = 0.26$$

On the other hand, the device models used for the theoretical computation have

$$L/a = 2 \text{ and } 8$$

$$V_B/V_p = 0.536$$

The difference in V_B/V_p ratios between the device model and the test unit can be taken care of by reverse biasing the gate junction of the test unit properly. Then, the normalized differential drain resistances of the test units are expected to have values between those for L/a = 2 and those for L/a = 8.

The differential drain resistances of the device models obtained from the computed drain characteristics with $V_{gs} = 0$ are shown in Fig. 4.16. The results of two experimental units with V_{gs} determined by

$$\left(\frac{V_{gs} + V_B}{V_p}\right)_{\text{test unit}} = \left(\frac{V_B}{V_p}\right)_{\text{device model}}$$

are also shown in the figure for comparison. In the figure, the differential drain resistances and the drain-to-source voltages are normalized by V_p/I_{DO} and V_p respectively where

$$I_{DO} = \frac{2a}{3L} q\mu_{no} N_D V_p Z$$

Z = width of the device in Z-direction

The values of I_{DO} for the test units have been determined by the experimental procedure used by Wu and Sah[6].

As can be seen in the figure, the experimental results for

$L/a \sim 6.4$ lie between the two lines for $L/a = 2$ and $L/a = 8$. Because of the fabrication process, the L/a ratios and the doping levels vary slightly for the test units. This is considered to be the cause of the variation in drain characteristics between the test units.

Although the comparison made here is crude, it clearly shows the correct order of magnitude and the dependence of the computed differential drain resistances on the drain-to-source voltages. From these observations, we can conclude that the device model and the numerical method developed are adequate to describe the steady state DC operations of various JFETs in detail.

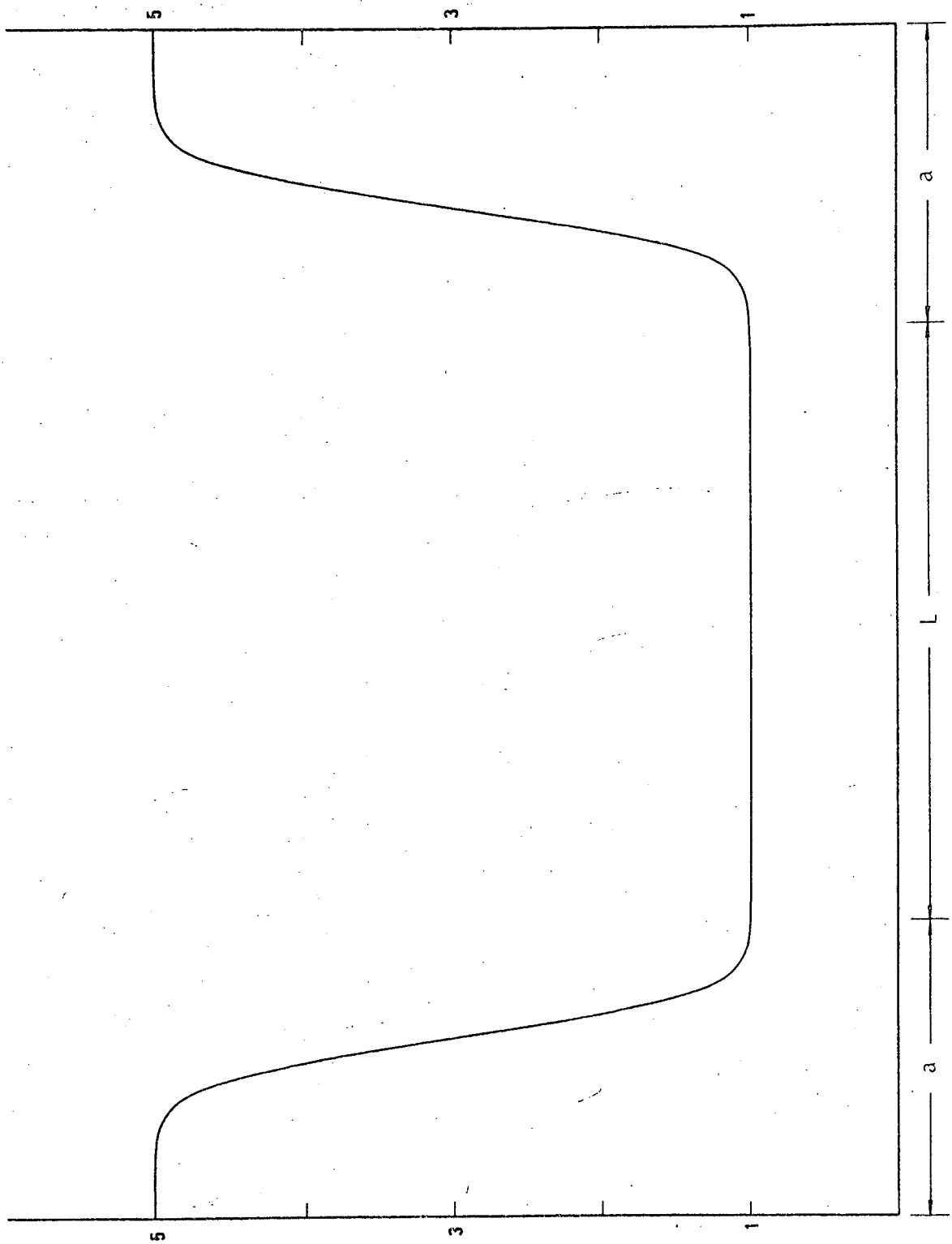

Figure 4.1-a Donor concentration on X-axis vs. x for the long and the short device

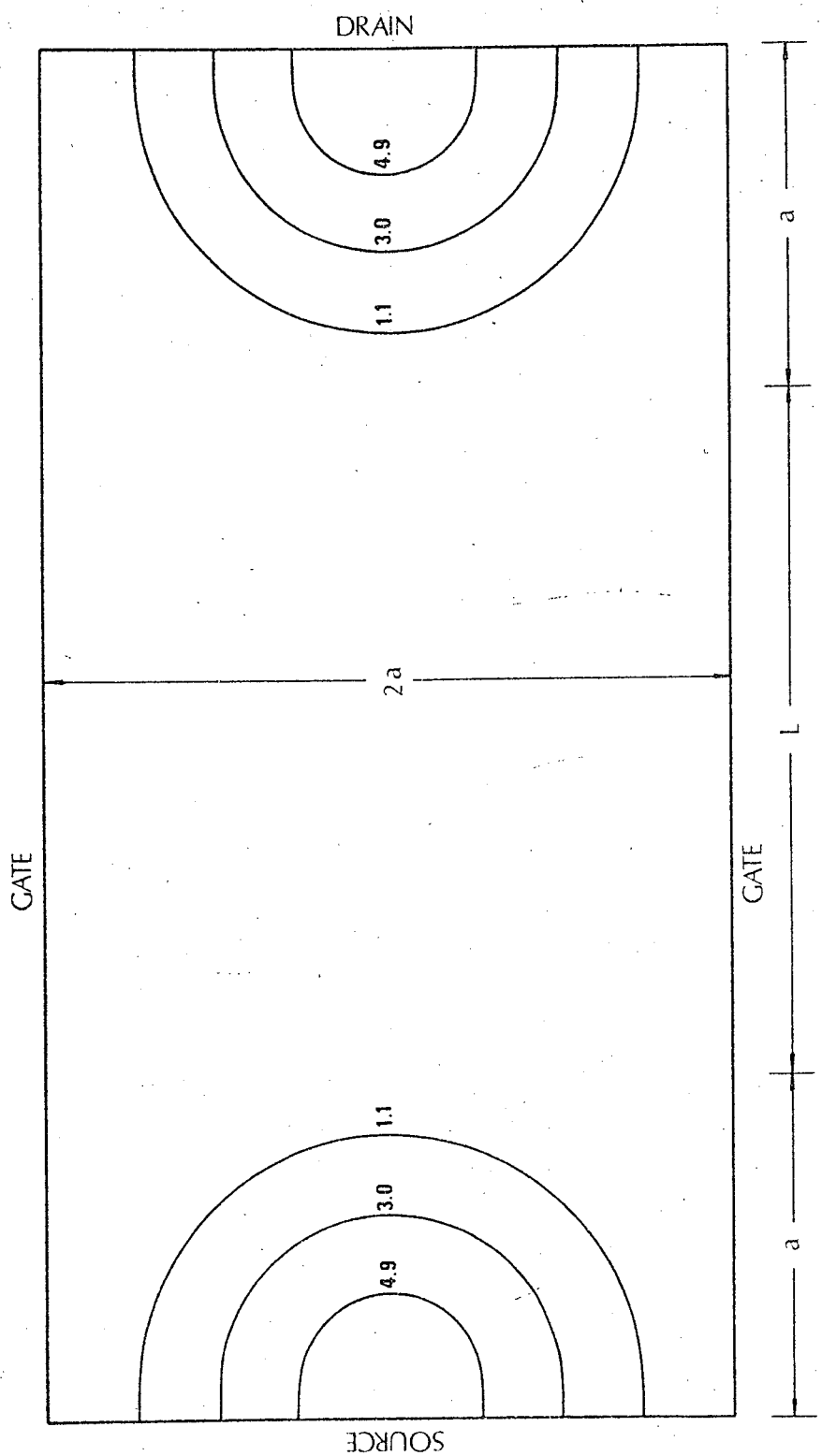

Figure 4.1-b Distribution of donor concentration and the definition of L for the long and the short device

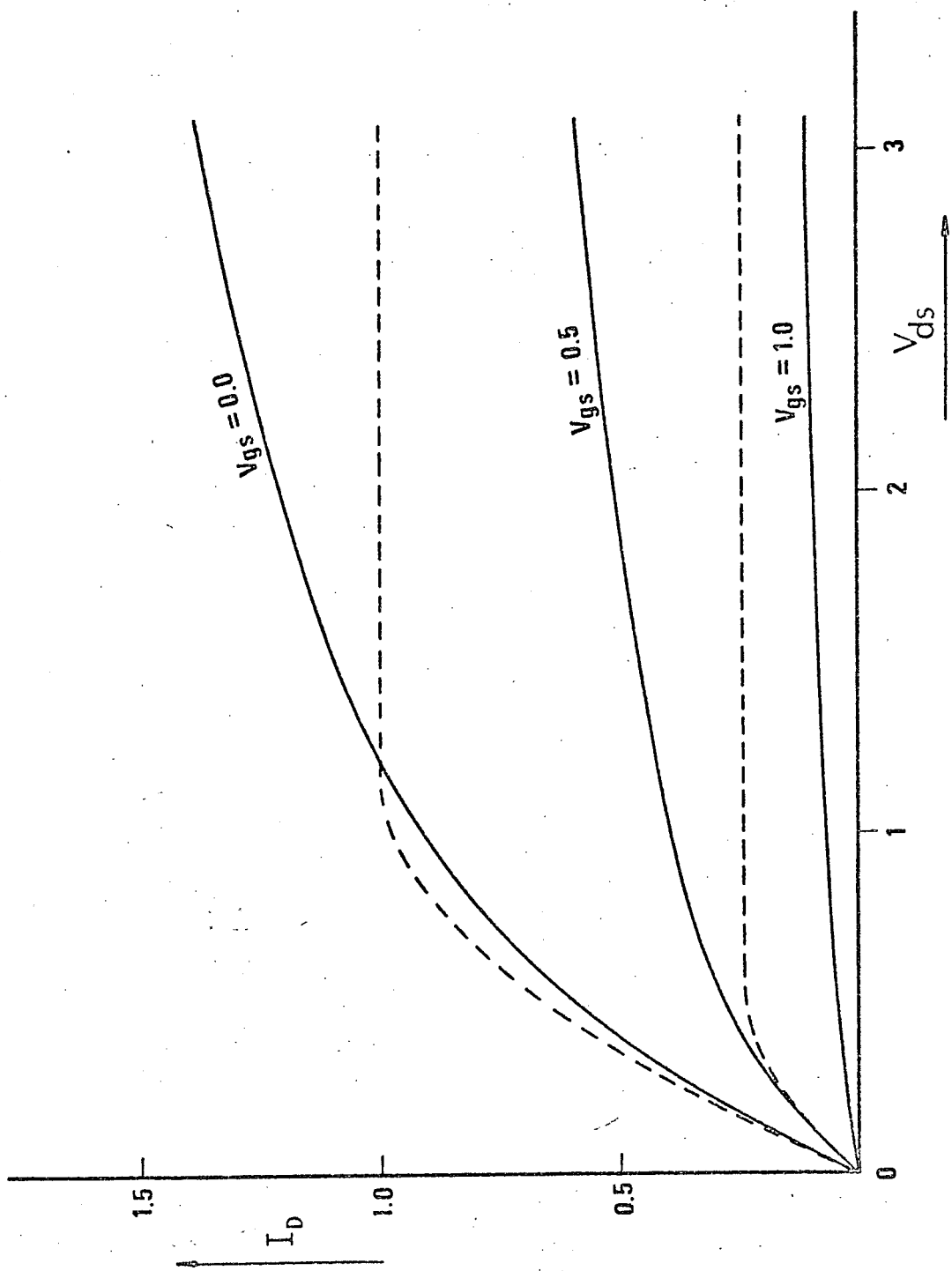

Figure 4.2 Drain Characteristics of the Short Device

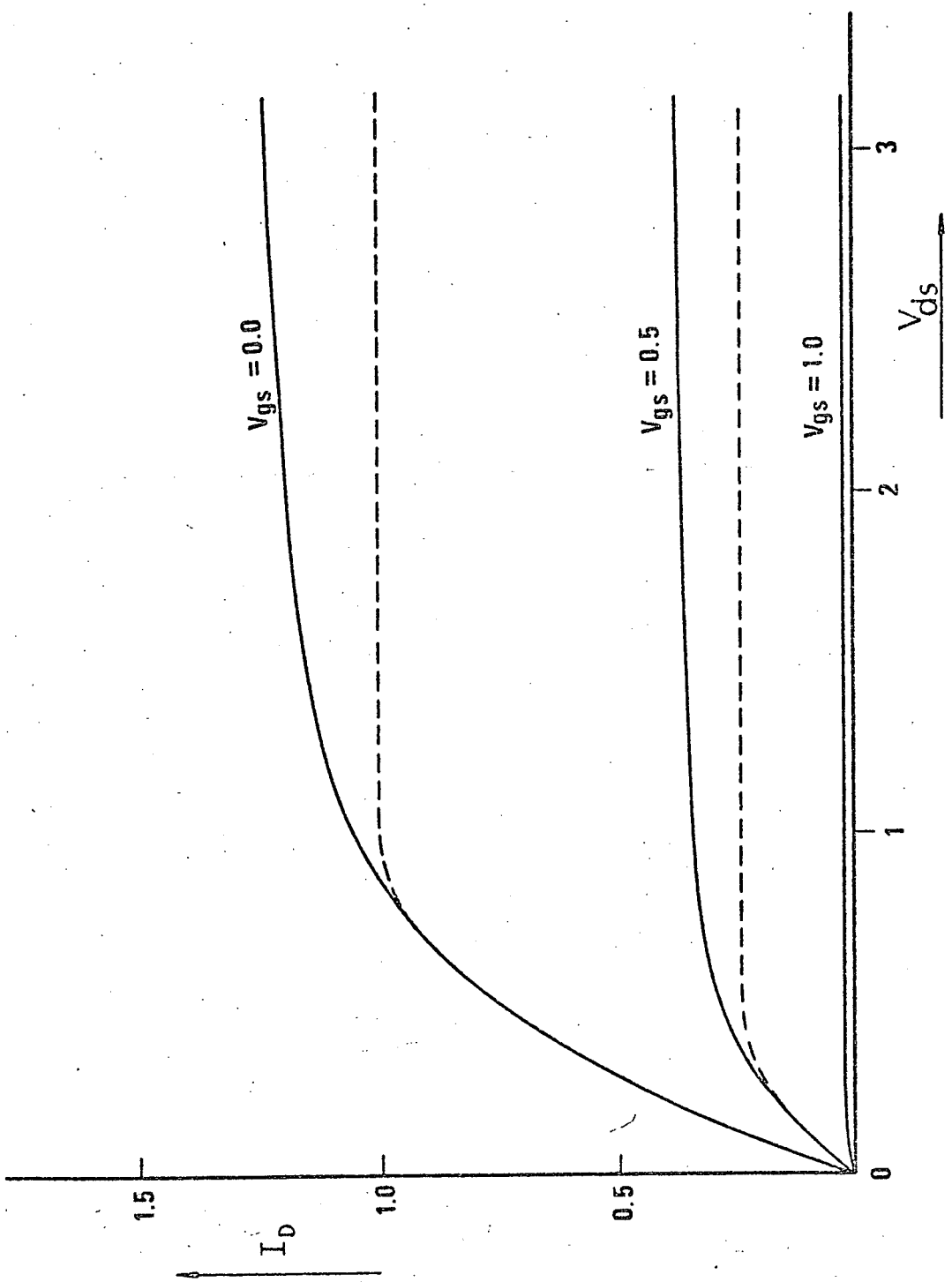

Figure 4.3 Drain Characteristics of the Long Device

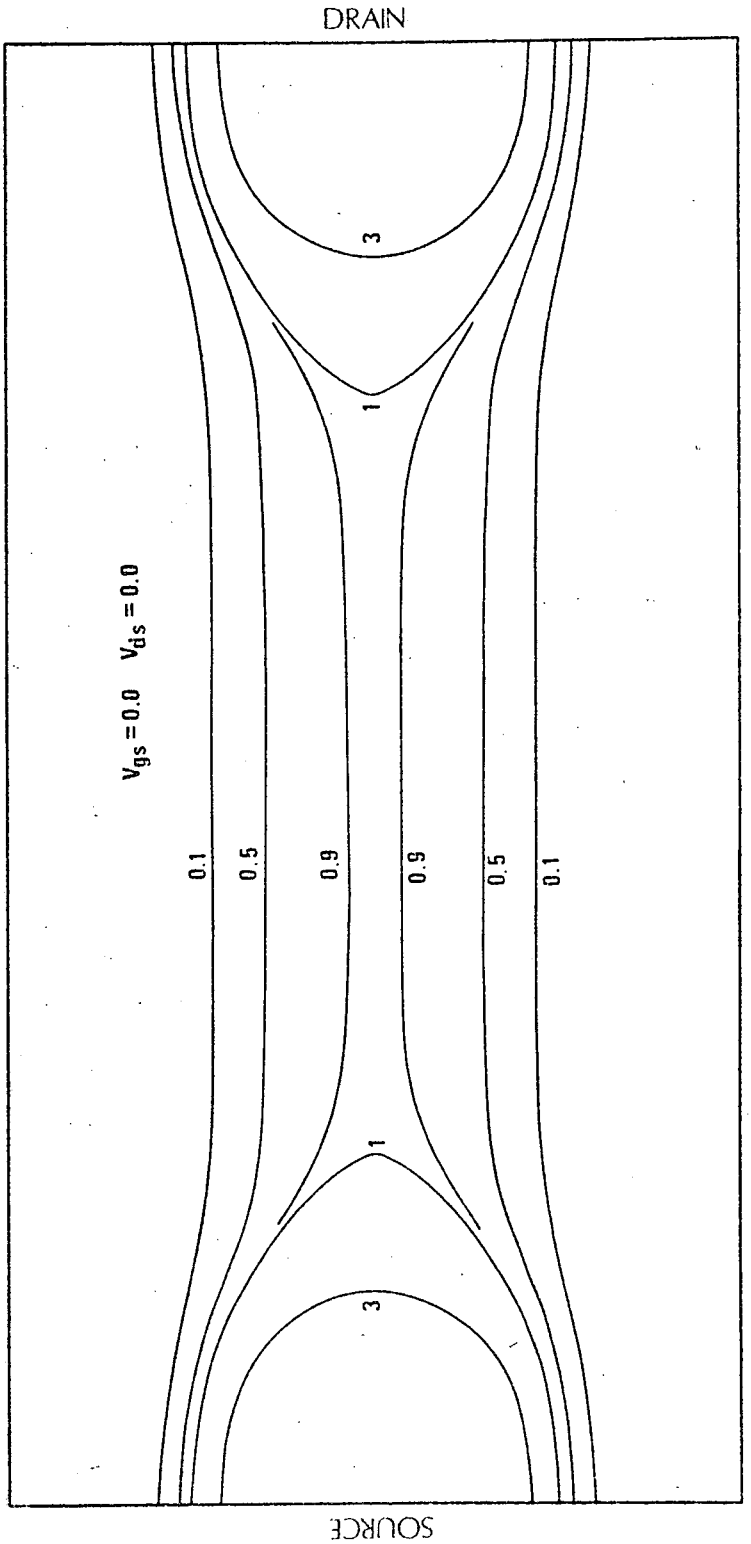

Figure 4.4 Distribution of the electron concentration for thermal equilibrium condition. The space-charge region is due to the built-in potential.

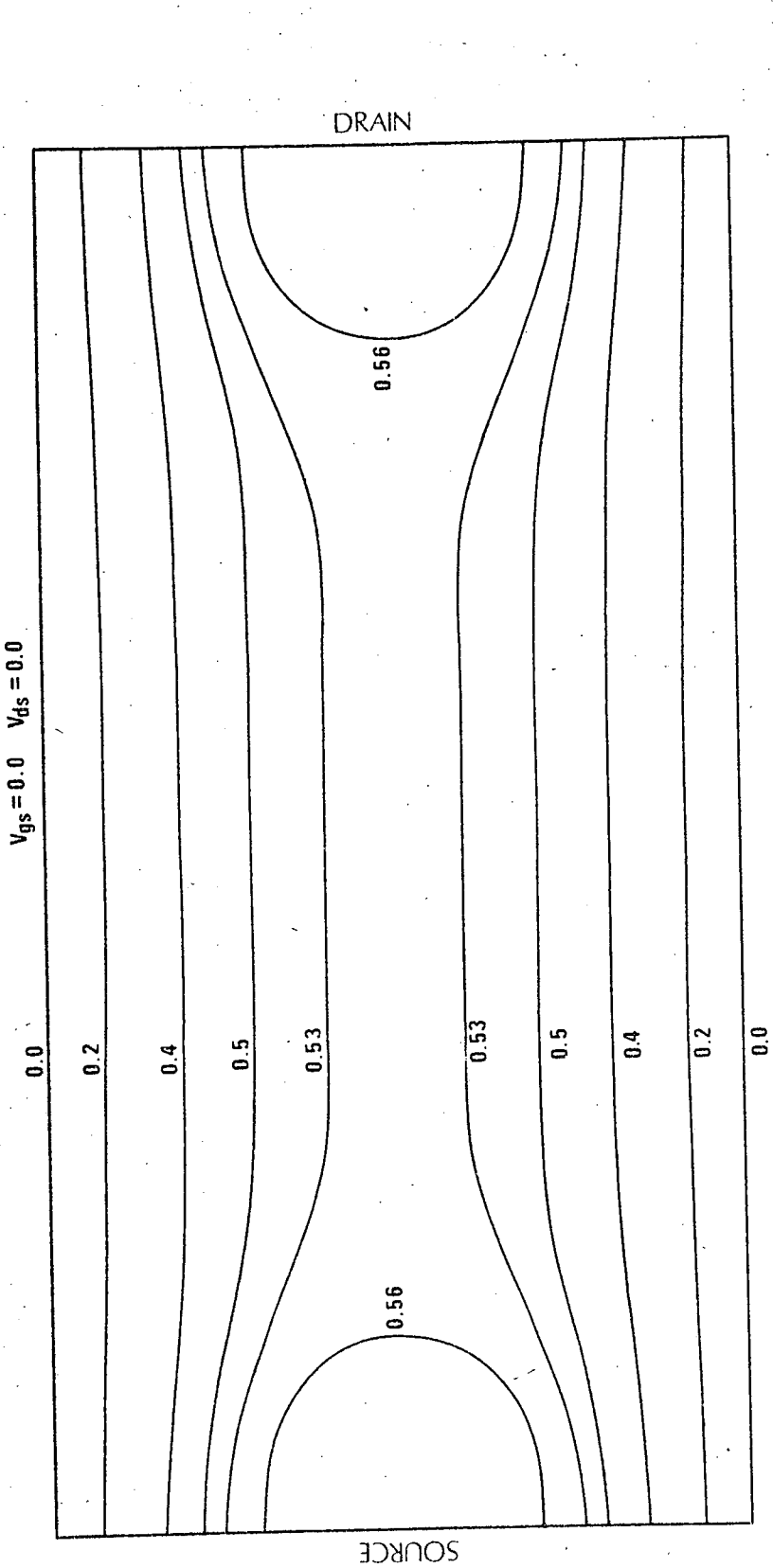

Figure 4.5 Potential distribution for thermal equilibrium condition. The slight potential rise at the source and the drain contacts are the built-in potential of the N+ -N junction.

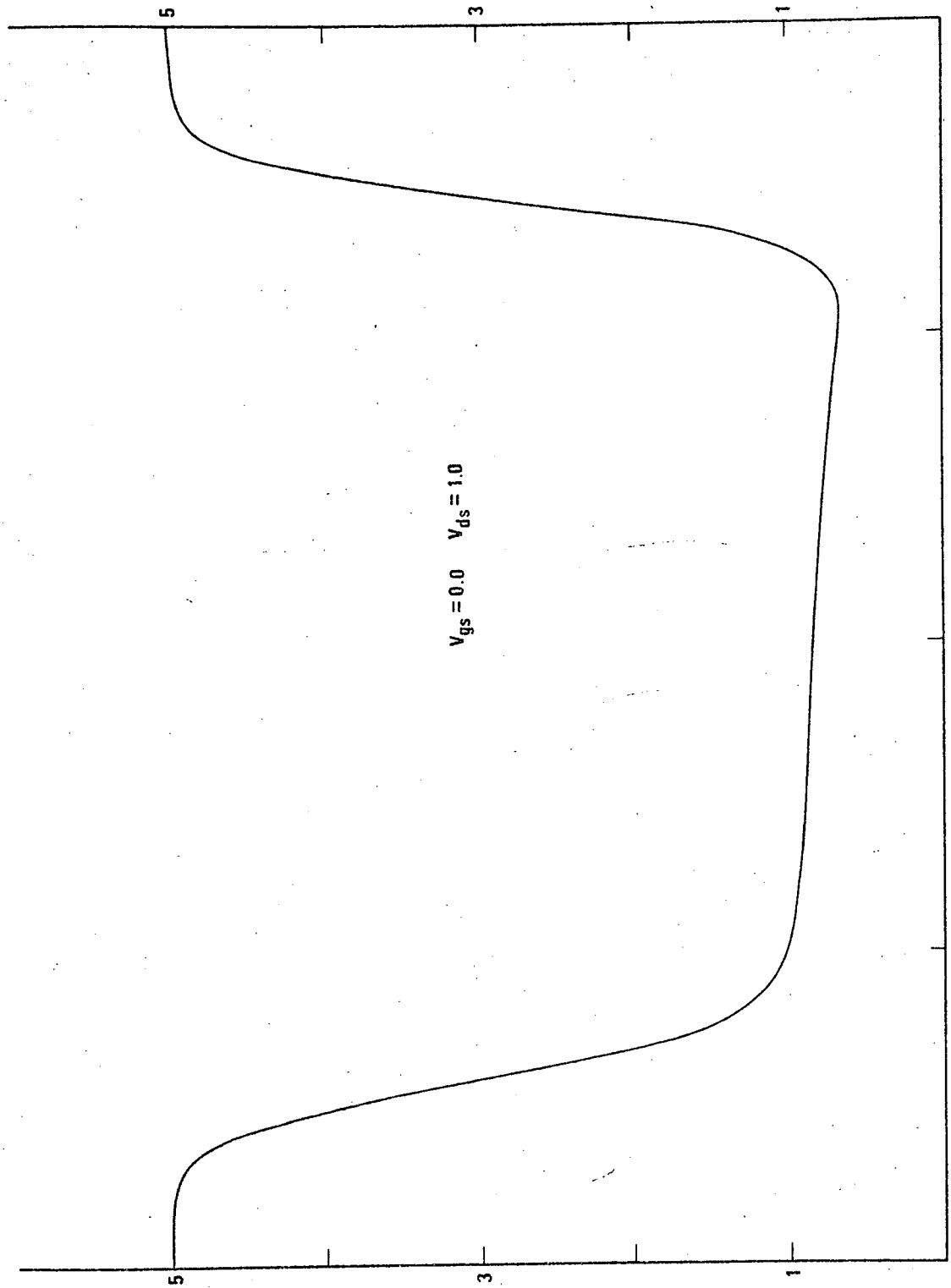

Figure 4.6-a Electron concentration on X-axis vs. x for the short devices

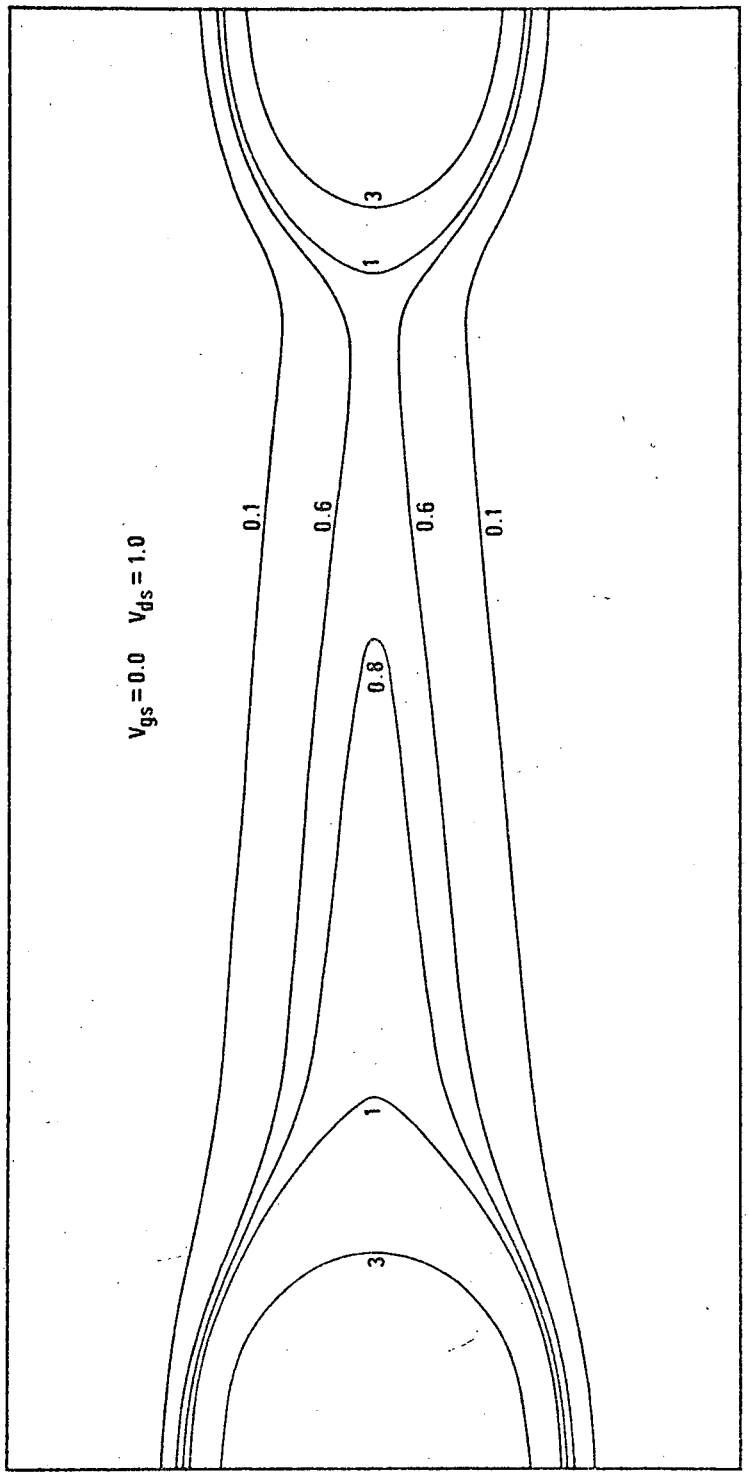

Figure 4.6-b Distribution of the electron concentration for the short device

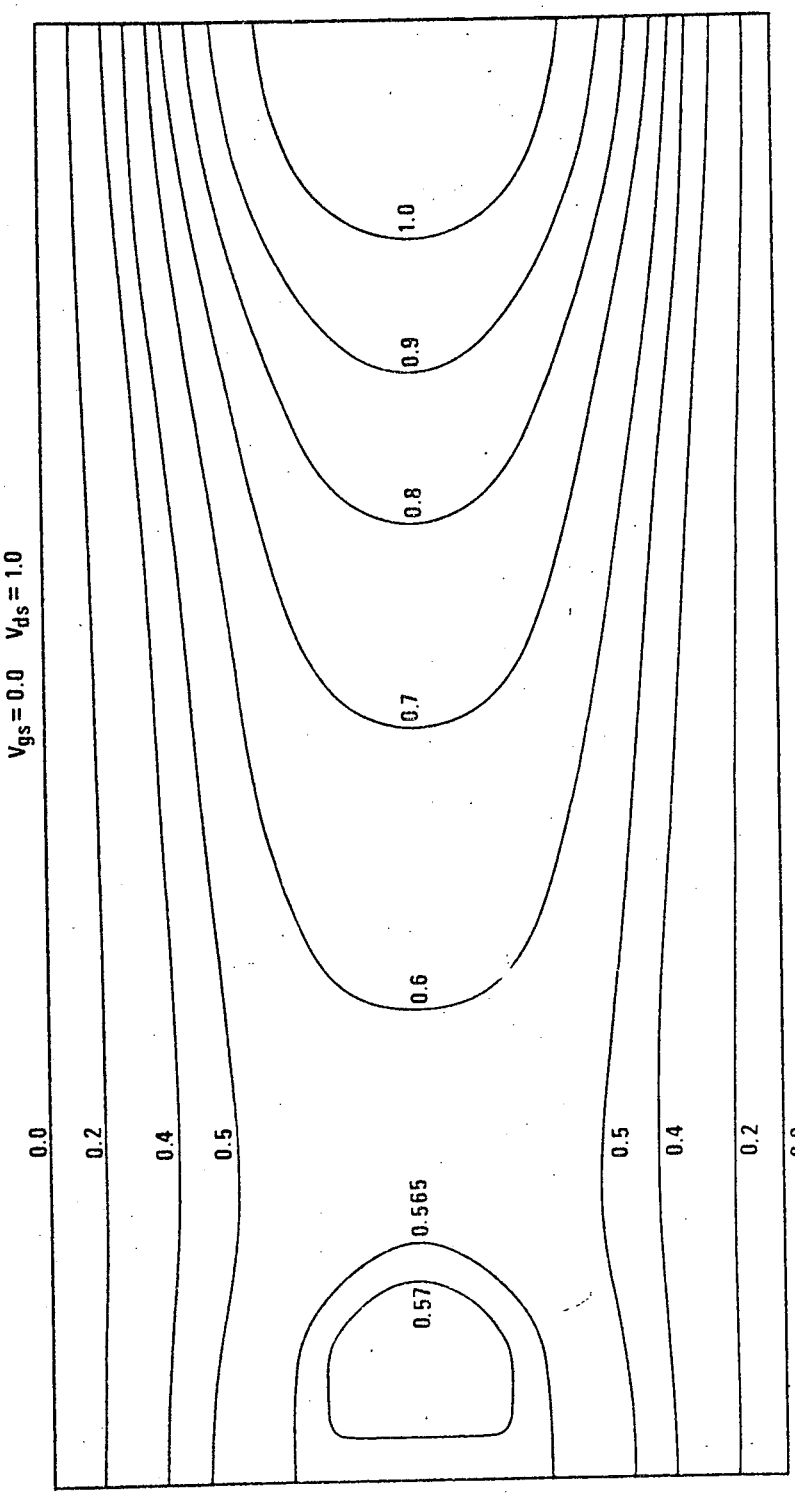

Figure 4.7 Potential distribution for the short device. The loop in the source region is due to the built-in potential of the N^+ -N junction.

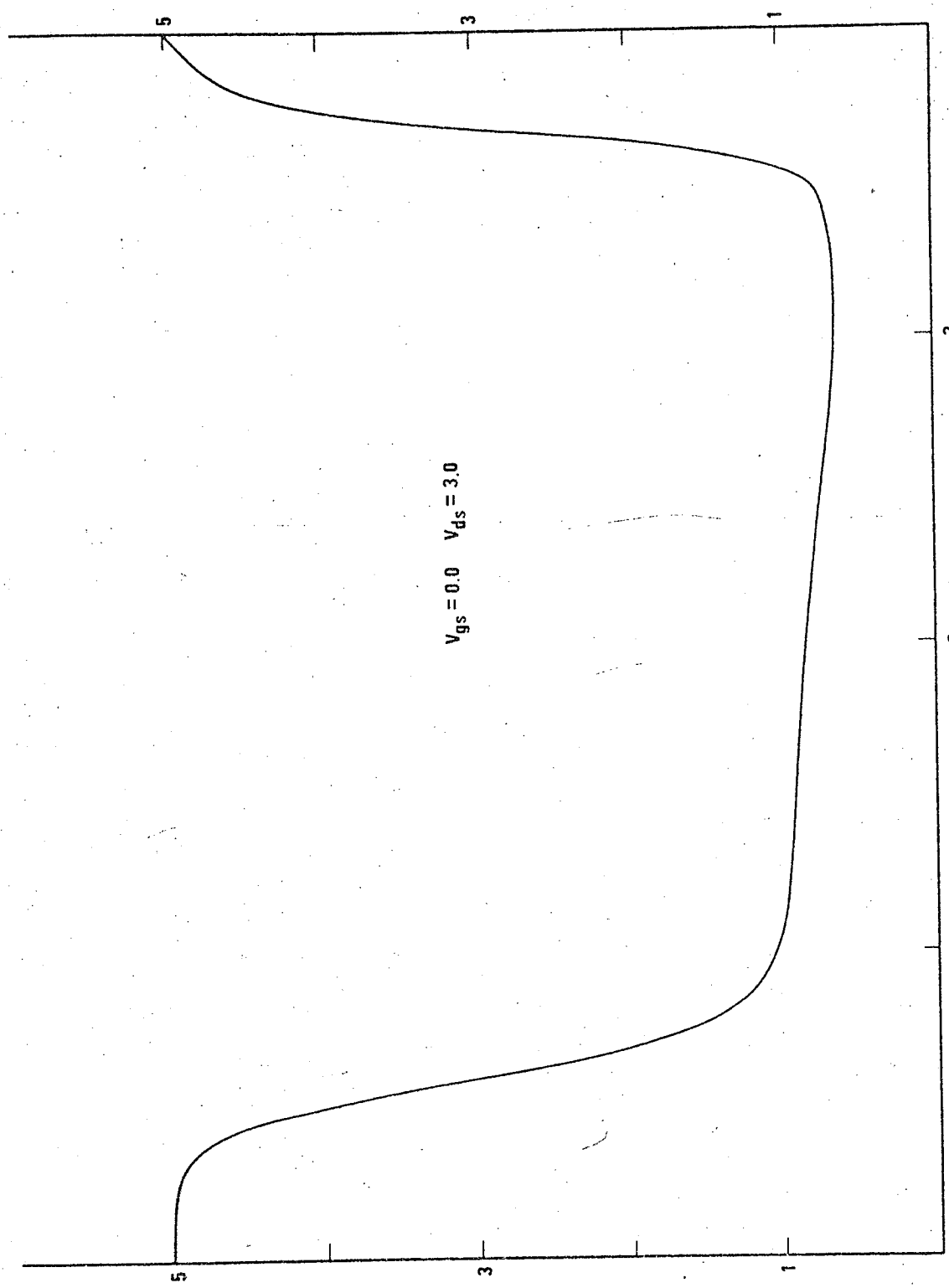

Figure 4.8-a Electron concentration on X-axis vs. x for the short device

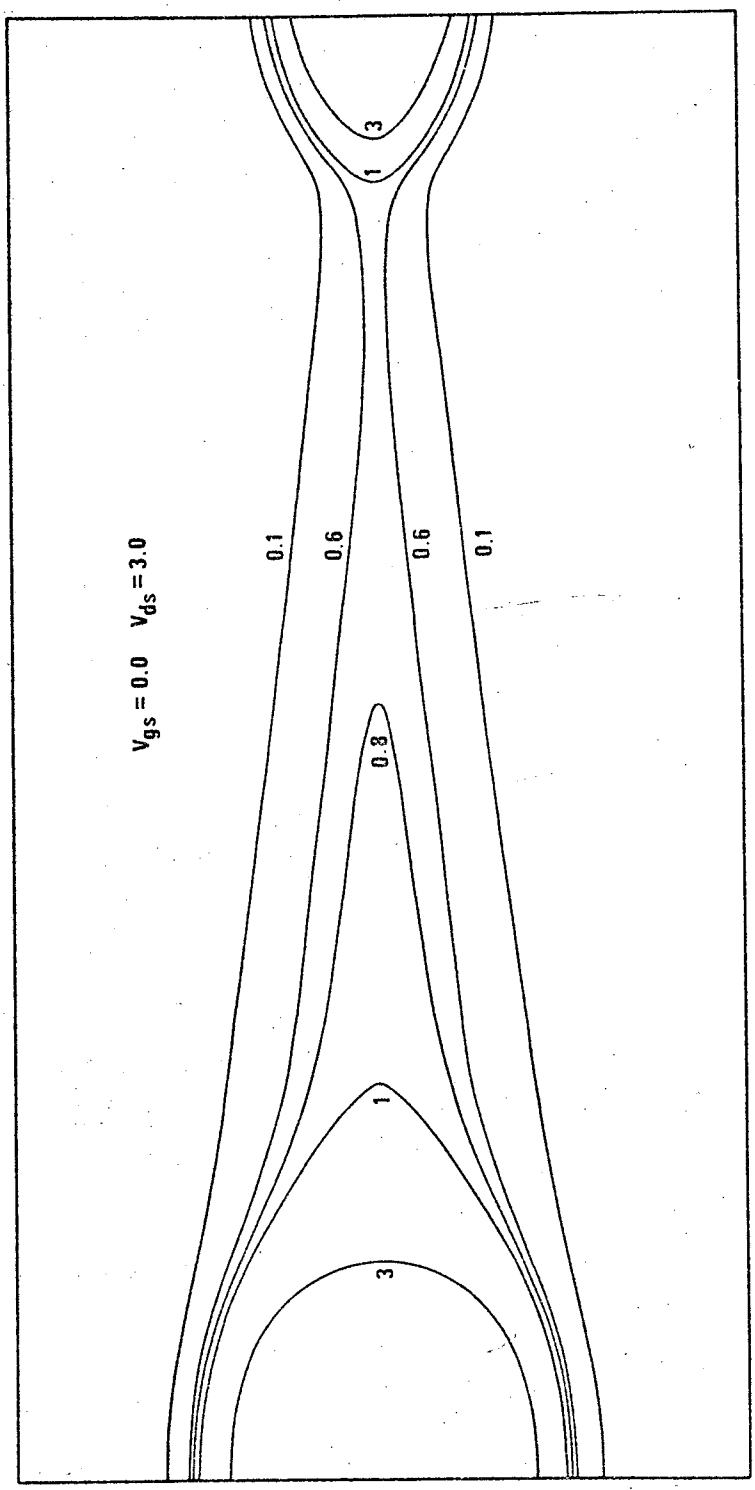

Figure 4.8-b Distribution of the electron concentration for the short device

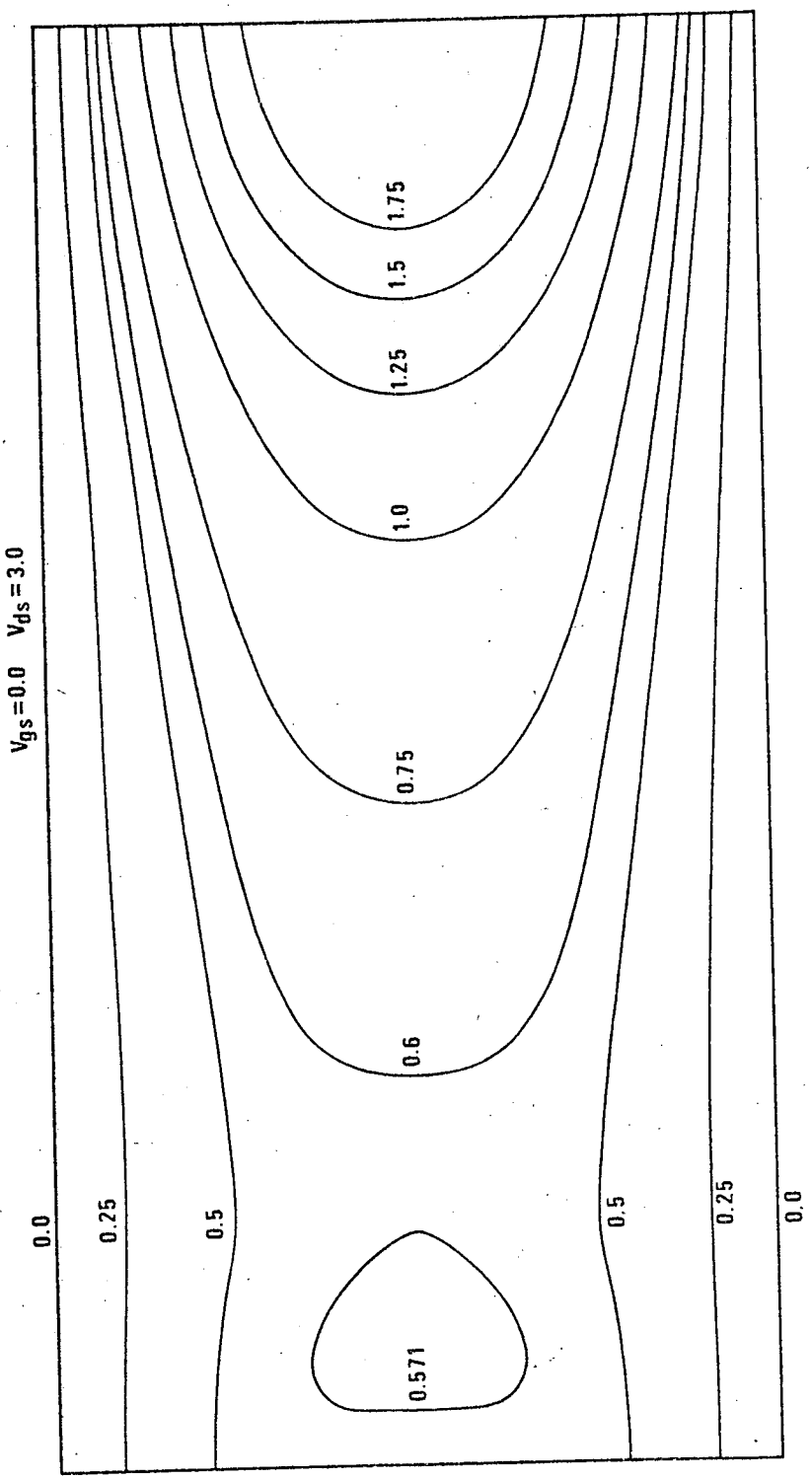

Figure 4.9 Potential distribution for the short device. The loop in the source region is due to the built-in potential of the N^+-N junction.

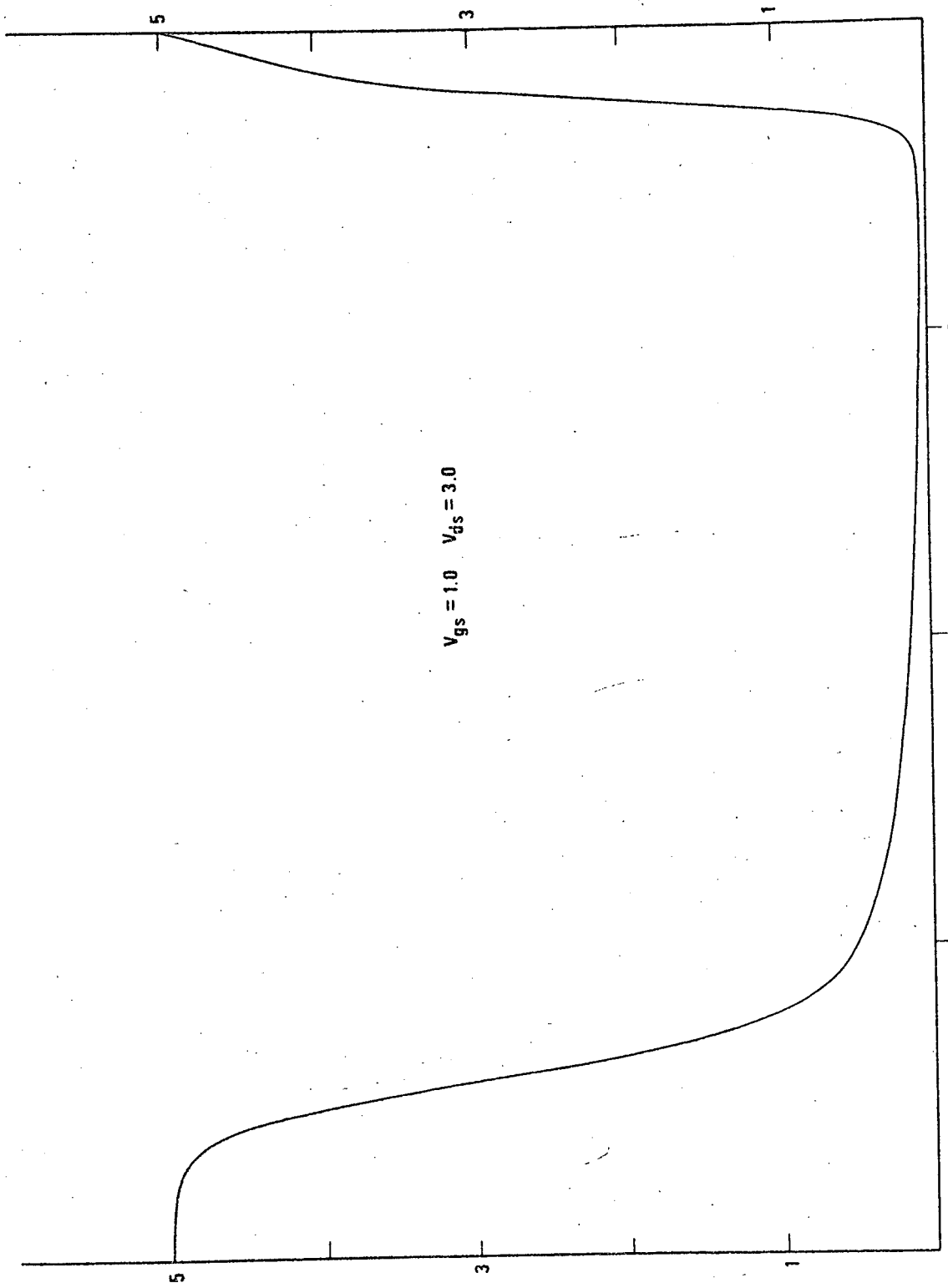

Figure 4.10-a Electron concentration on X-axis vs. x for the short device

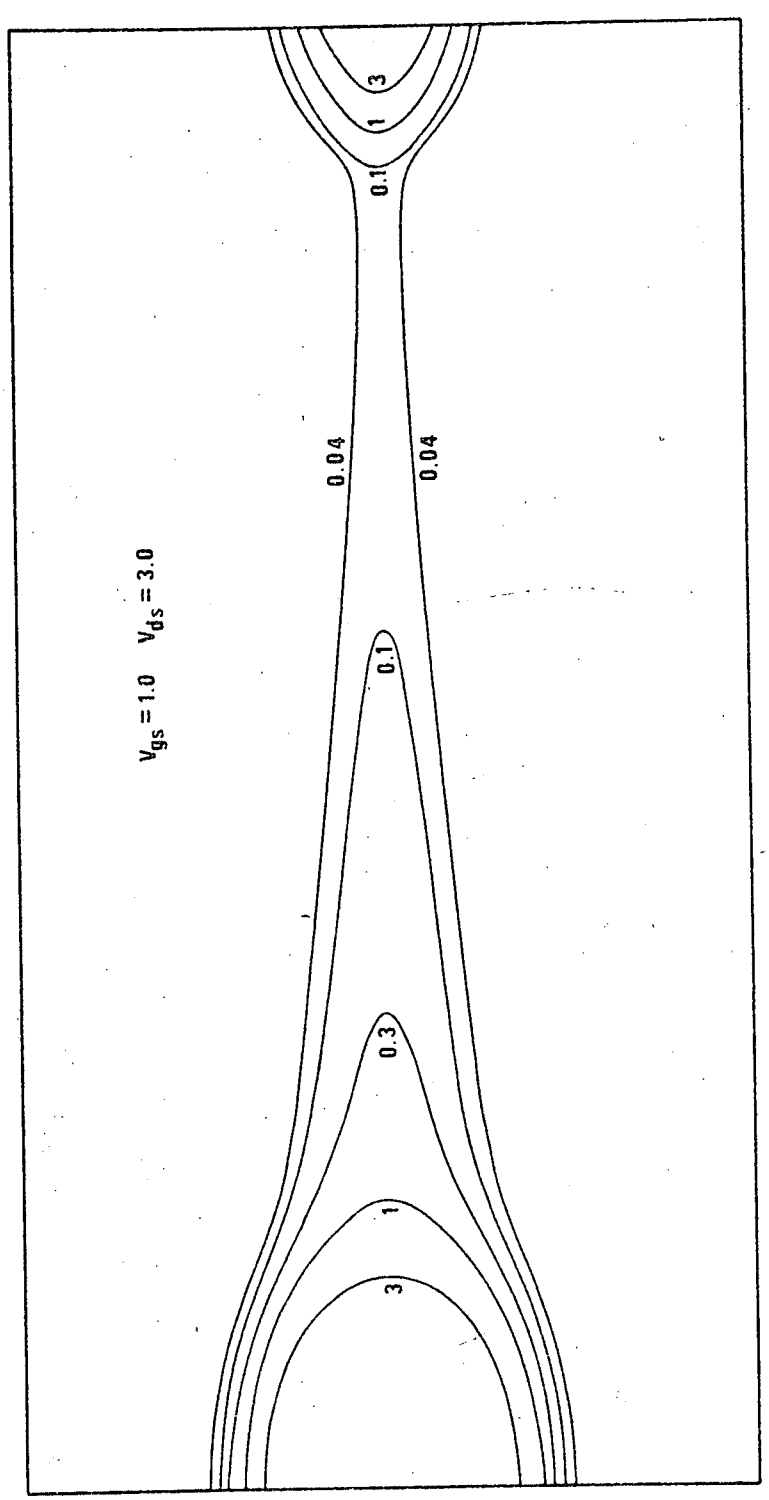

Figure 4.10-b Distribution of the electron concentration for the short device

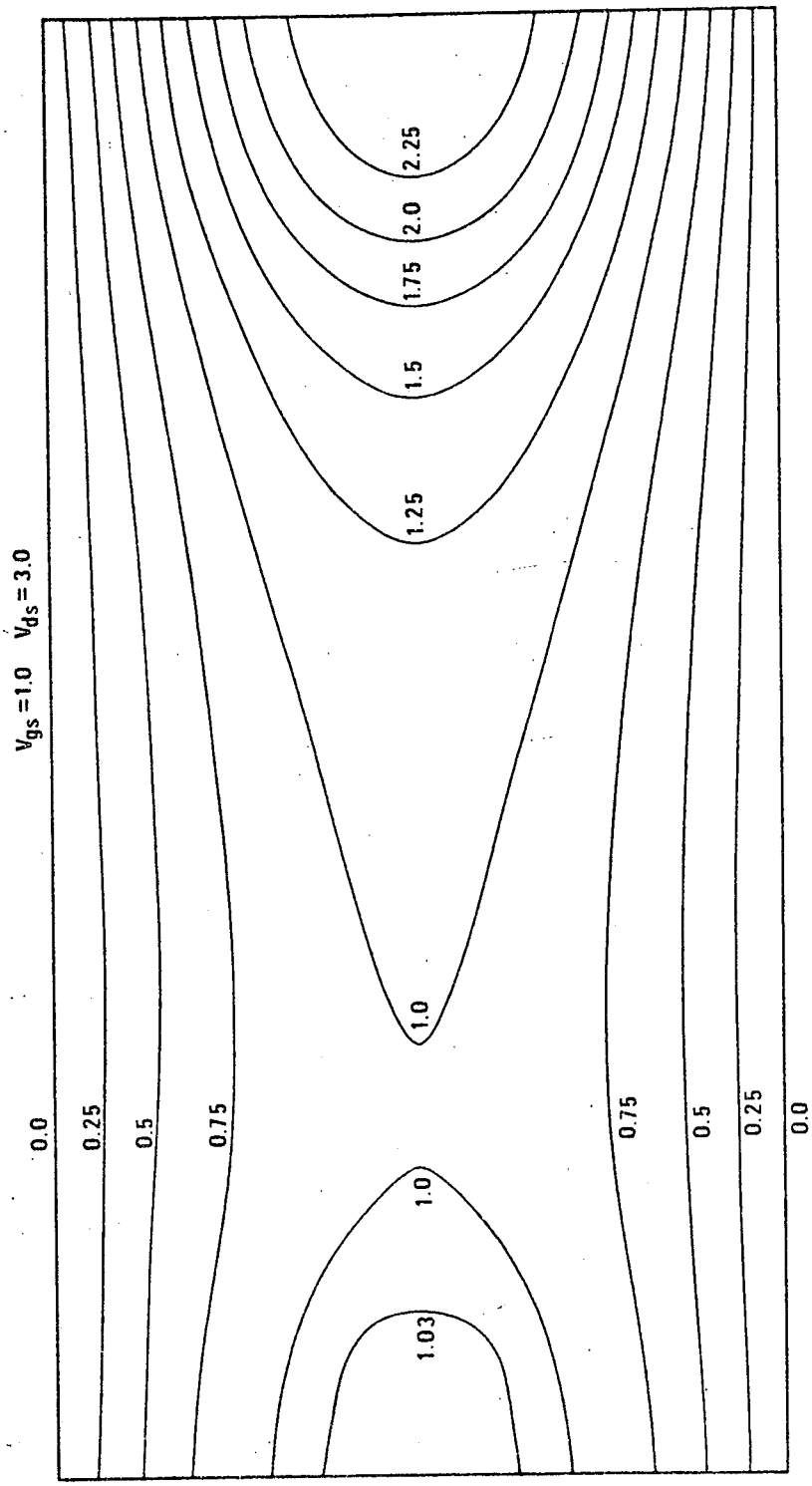

Figure 4.11 Potential distribution for the short device

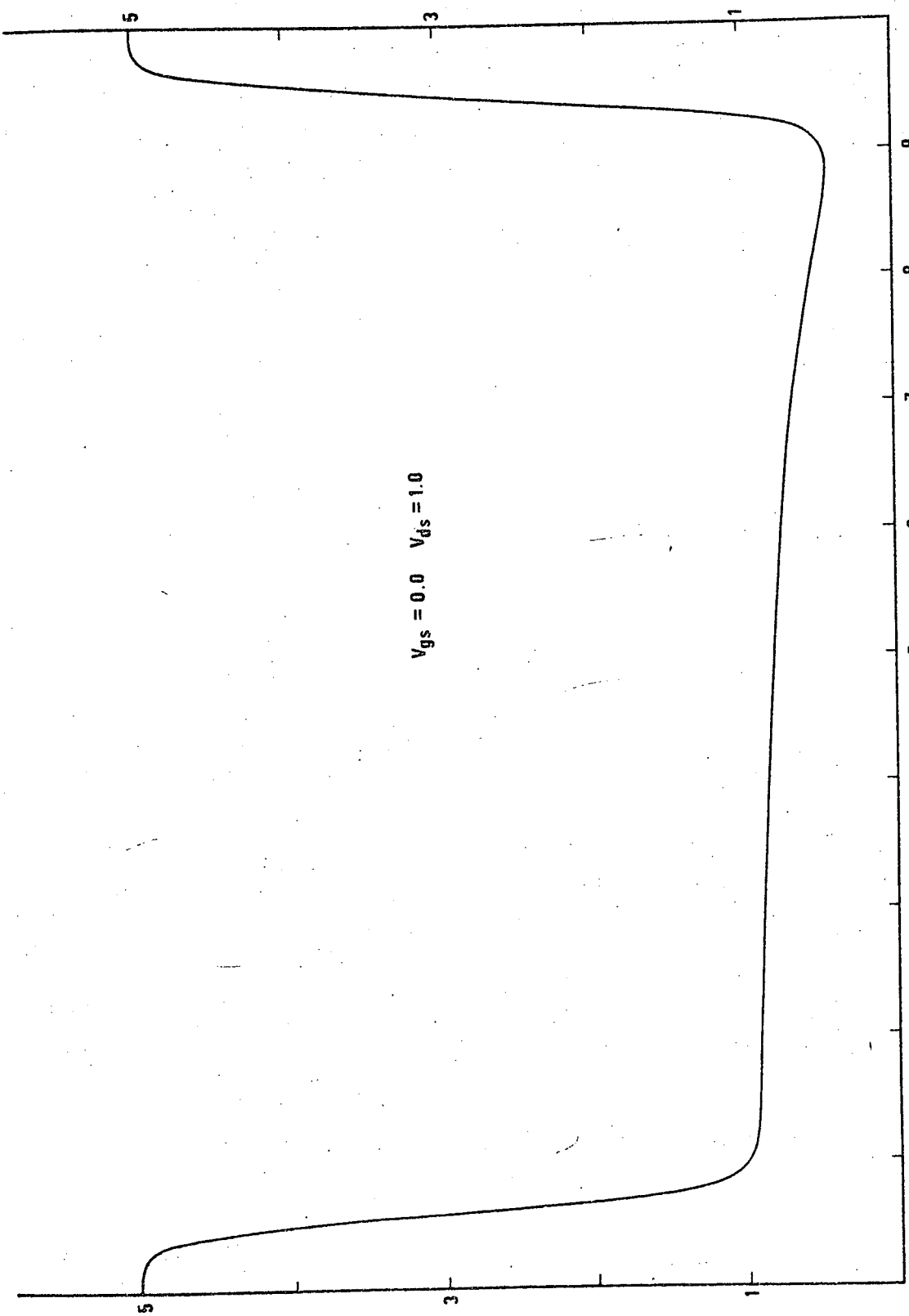

Figure 4.12-a Electron concentration on X-axis vs. x for the long device

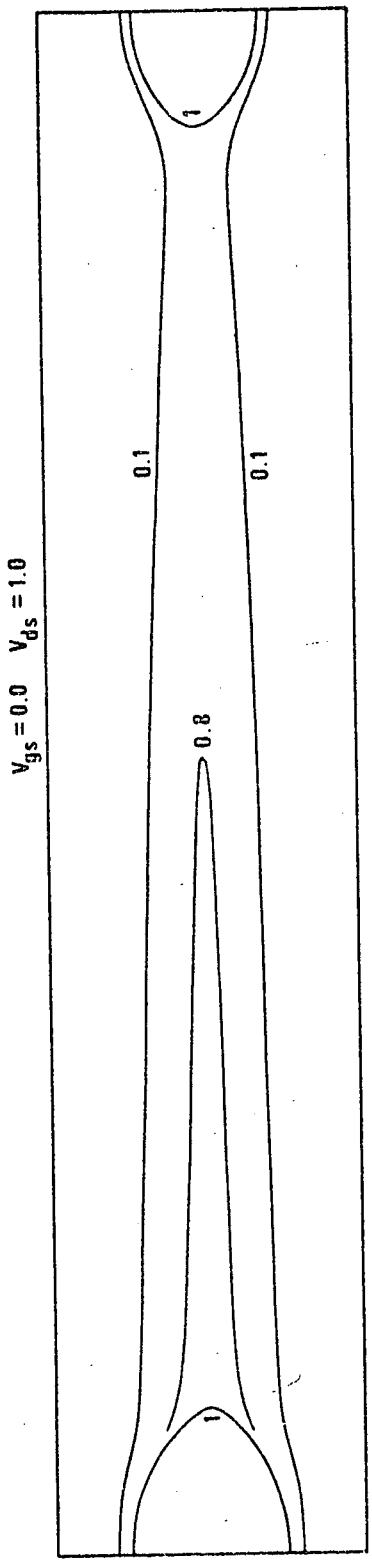

Figure 4.12-b Distribution of the electron concentration for the long device

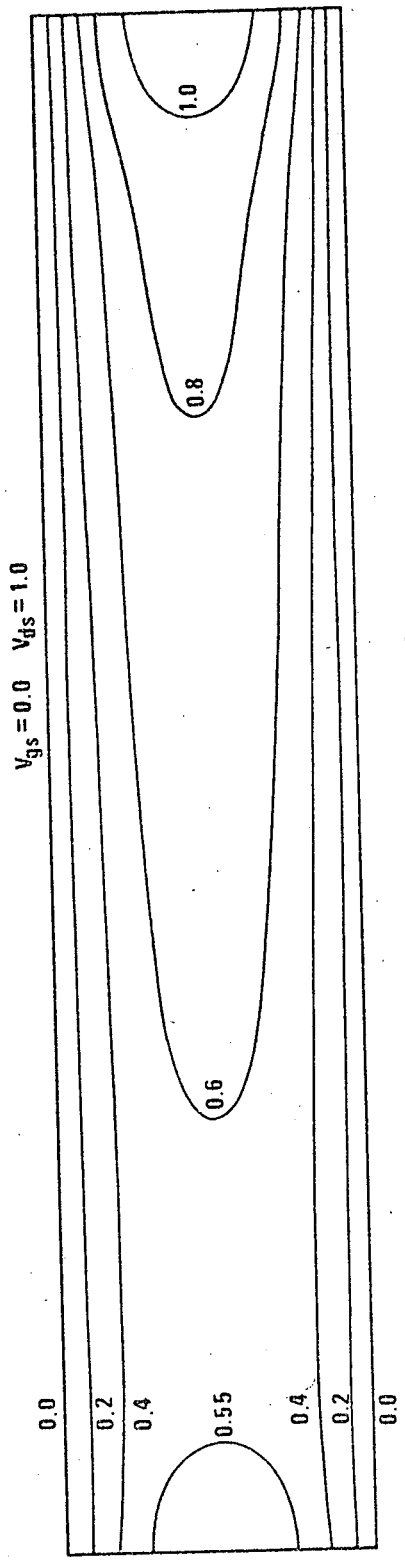

Figure 4.13 Potential distribution for the long device

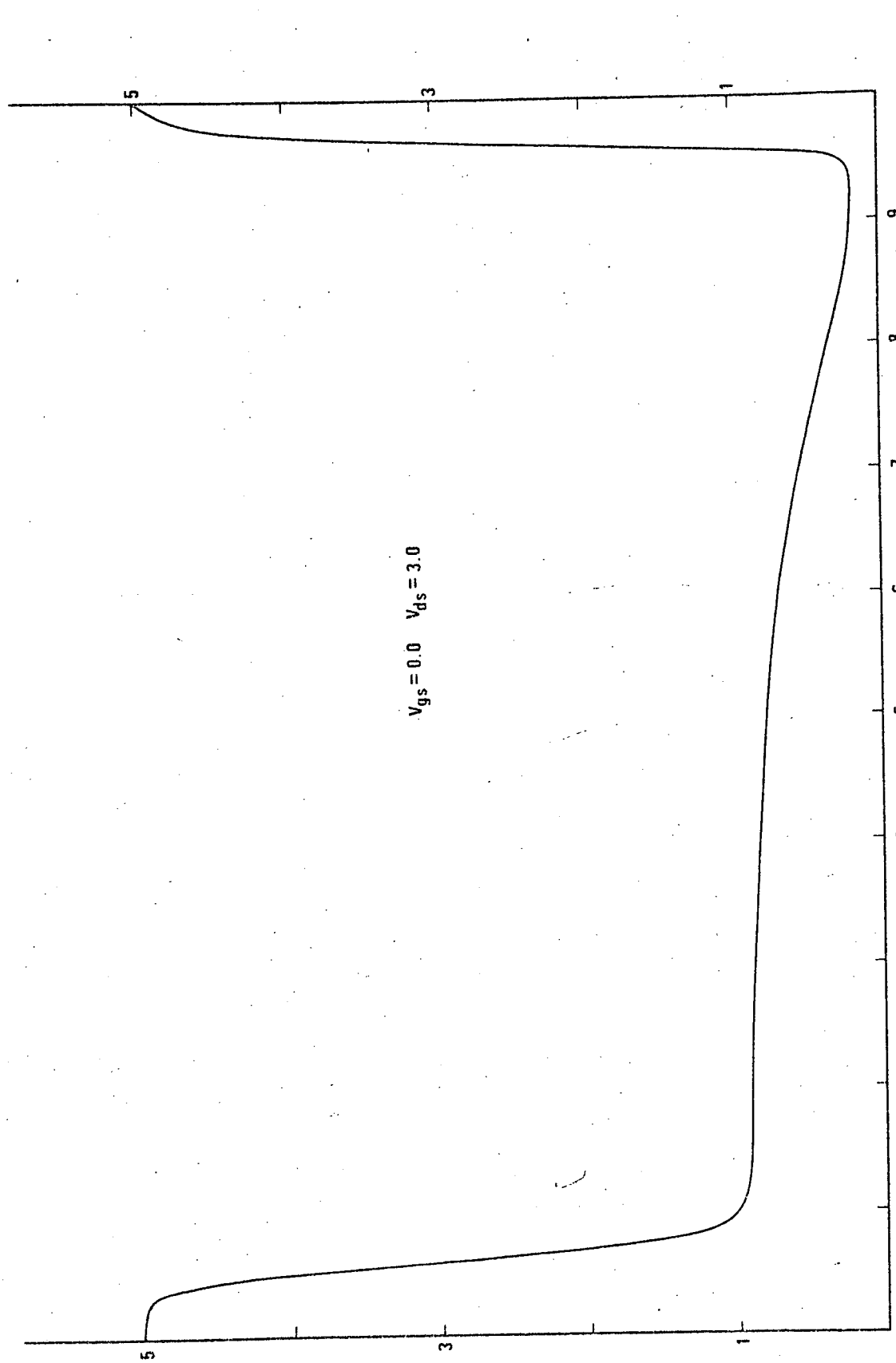

Figure 4.14-a Electron concentration on X-axis vs. x for the long device

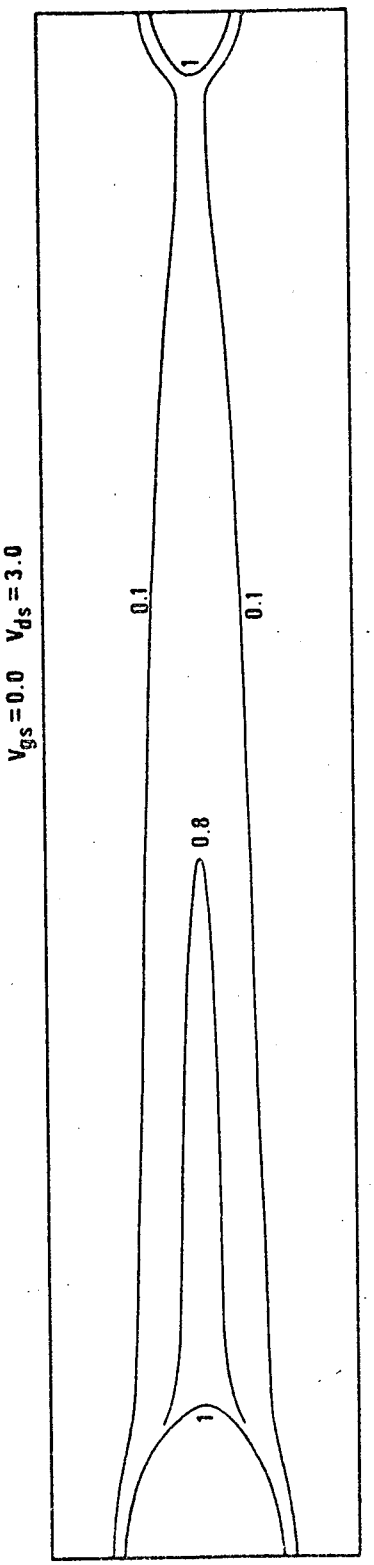

Figure 4.14-b Distribution of the electron concentration for the long device

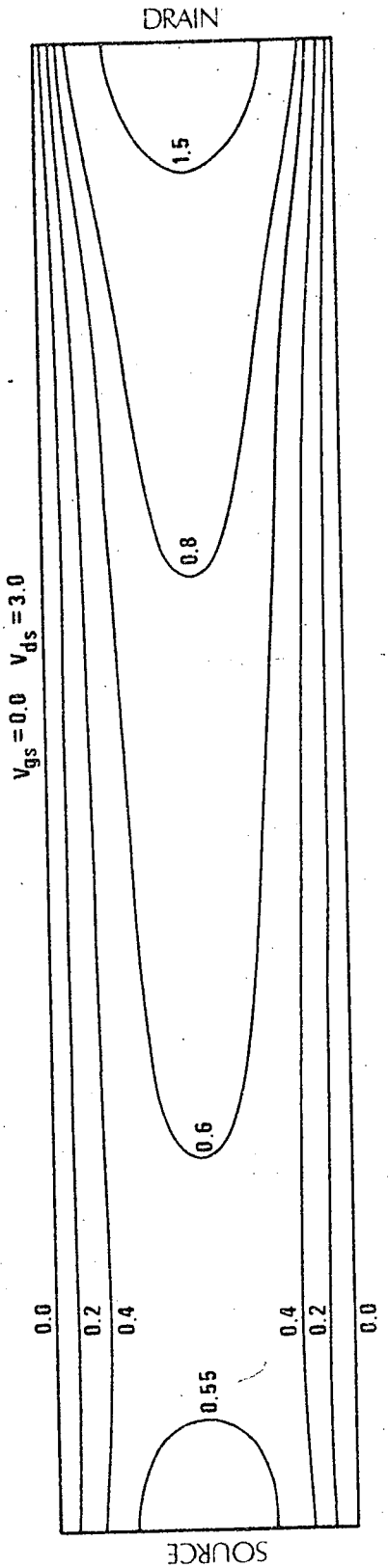

Figure 4.15 Potential distribution for the long device

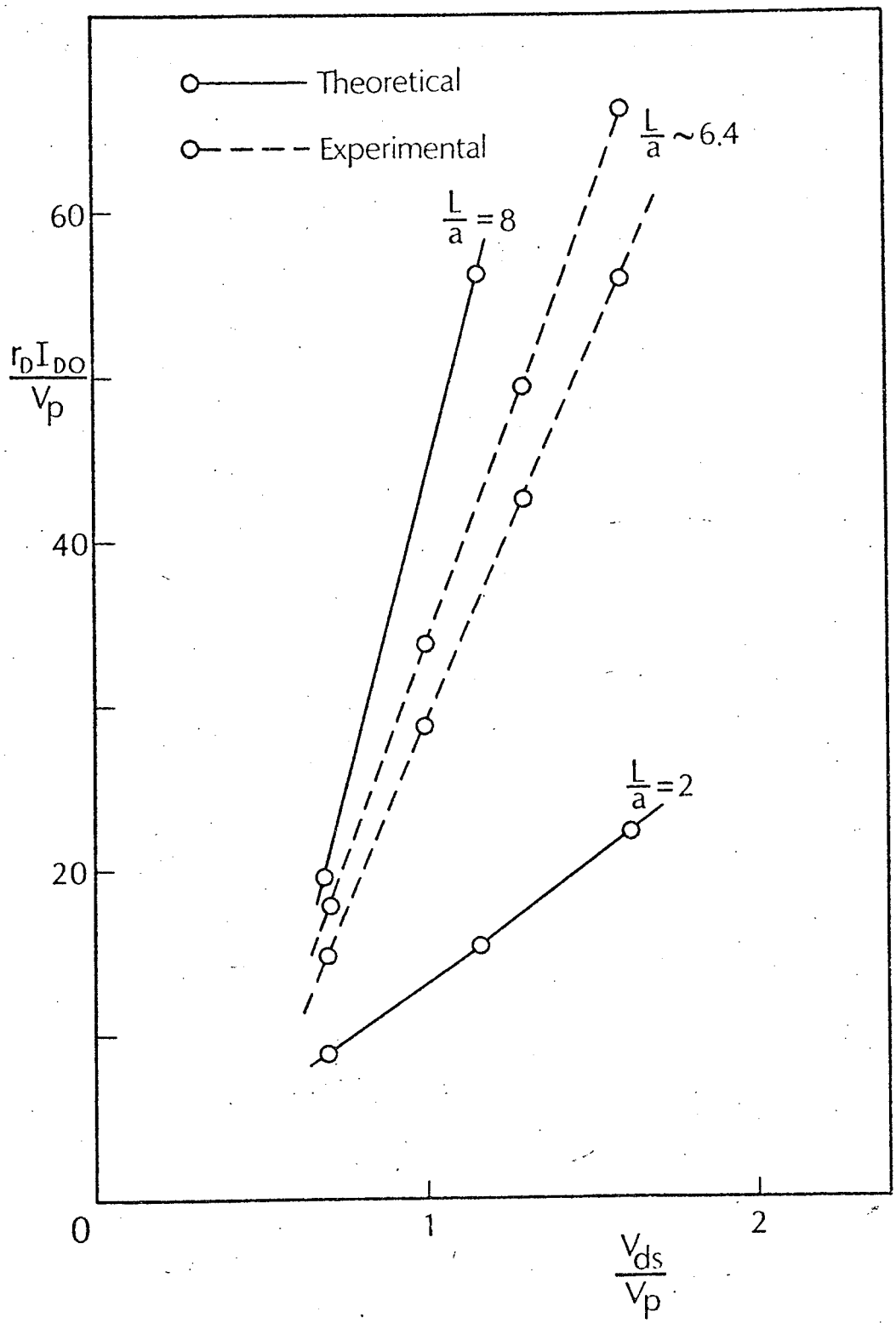

Figure 4.16 Differential drain resistance versus Drain-to-source voltage

IV-2 Graded-Channel Device

The devices with very small length-to-width ratios can be constructed by lateral diffusion of the source N^+-region and the gate P^+-regions into the N-type epitaxial layer which is grown over the N^+ substrate.[13,16,34] As a result of this process the impurity distribution is non-uniform along the channel and the current flows parallel to the gradient of the impurity distribution.

To study these devices, a device model with the same dimensions as the short device and with the distribution of the donor concentration as shown in Fig. 4.17 is analyzed in this section. In the figure the donor concentration is normalized by $N_D = 10^{15}$ atoms/cm^3. Although the model chosen here is somewhat unrealistic due to the low doping level in the N^+-regions, the results are significantly different from those in the previous section and indicate the possibility of a SCL-triode which will be the subject of the next chapter.

Fig. 4.18 shows the drain characteristics of the device. The dashed curves are the results of the gradual-channel approximation with $L/a = 0.794$. This value is obtained by defining L of the device as the length of the region where $N(x,0) \leq 1.05$. Due to the low doping level in the N^+-regions the drain and the source resistance are large. The effect of these resistances are seen in the gradual-channel approximations as the shift of the saturation point to the right of the figure.

The comparison of Fig. 4.20 with 4.22 and Fig. 4.24 with 4.26 shows a considerably large change in the potential distribution in the source region with increasing drain voltage. This appears in the drain characteristics as the large differential drain conductance. The maximum electric field in X-direction for $V_{gs} = 0$ and $V_{ds} = 3$ is 13.3 Kv/cm and the drift velocity is not saturated. The field dependent mobility, therefore, is not an important factor for the operation of the device up to the bias condition $V_{ds} = 3$.

The most interesting result of the device is the variation of the distribution of the electron concentration with the bias voltages. From Table 4.2, we see that for small drain voltages, the electron concentration in the conductive channel decreases with increasing drain voltages while for large drain voltages it increases with increasing drain voltage. In Figs. 4.19, 4.21, 4.23, and 4.25, we also see that the distribution of the electron concentration is similar to that of the short device for small drain voltages while it is significantly different for large drain voltages. It can be concluded from these observations that a new current conduction is in operation for large drain voltages, i.e., the SCL current starts to build up. Because of the low doping level of the source N^+-region and the gradual transition from the source N^+-region to the N-region, however, the SCL current is not dominant for the device. This is also seen in the drain characteristics. If the SCL current were

V_{ds} \ V_{gs}	0.0	0.5	1.0
0.1	0.9194	0.7011	0.2706
1.0	0.8217	0.5280	0.2096
2.0	0.9160	0.6188	0.2958
3.0	1.0160	0.7185	0.3754

Table 4.2 Minimum electron concentration on the X-axis for various bias conditions

dominant, the drain current would be proportional to the square of the drain voltage which gives the triode characteristics. The drain characteristics shown in Fig. 4.18 are the result of the competition of two different physical mechanisms; the normal field-effect transistor operation where the free carrier concentration in the conductive channel decreases with increasing drain voltage and the SCL current where it increases with increasing drain voltage. Previously, the large differential drain conductance was attributed to the large change of the potential distribution in the source region. This, however, is due to the increase of the electron concentration in the channel.

The ratio of the length of the N-region to the extrinsic Debye length, L/L_{DE}, is about 8 for this device. If the N^+-N junction at the source is abrupt and L/L_{DE} is decreased, the drain and the source N^+-regions will interact with each other and the SCL current can easily be realized. A device satisfying the above conditions will be considered in Chapter V.

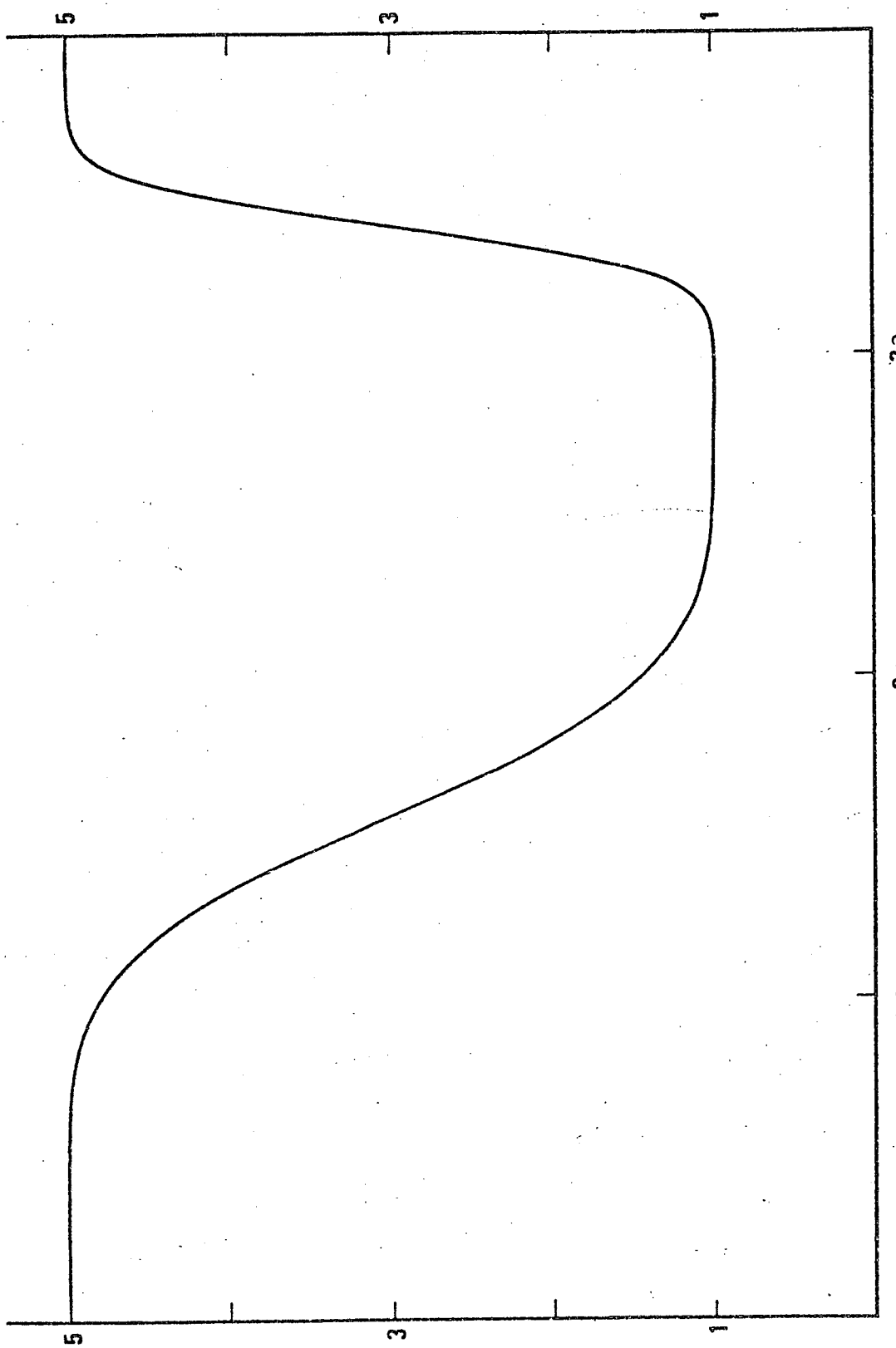

Figure 4.17-a Donor concentration on X-axis vs. x
for the graded-channel device

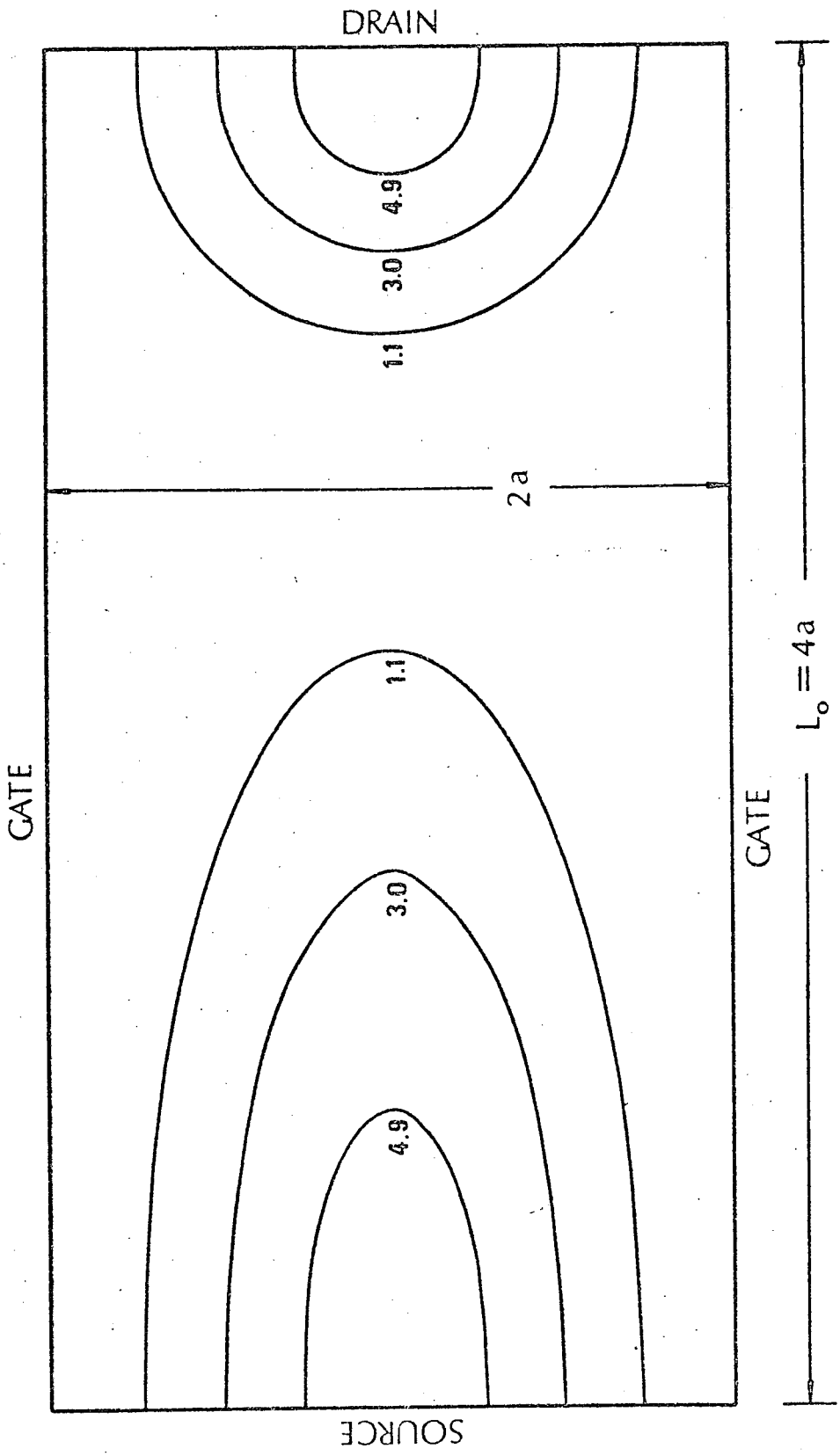

Figure 4.17-b Distribution of the donor concentration for the graded-channel device

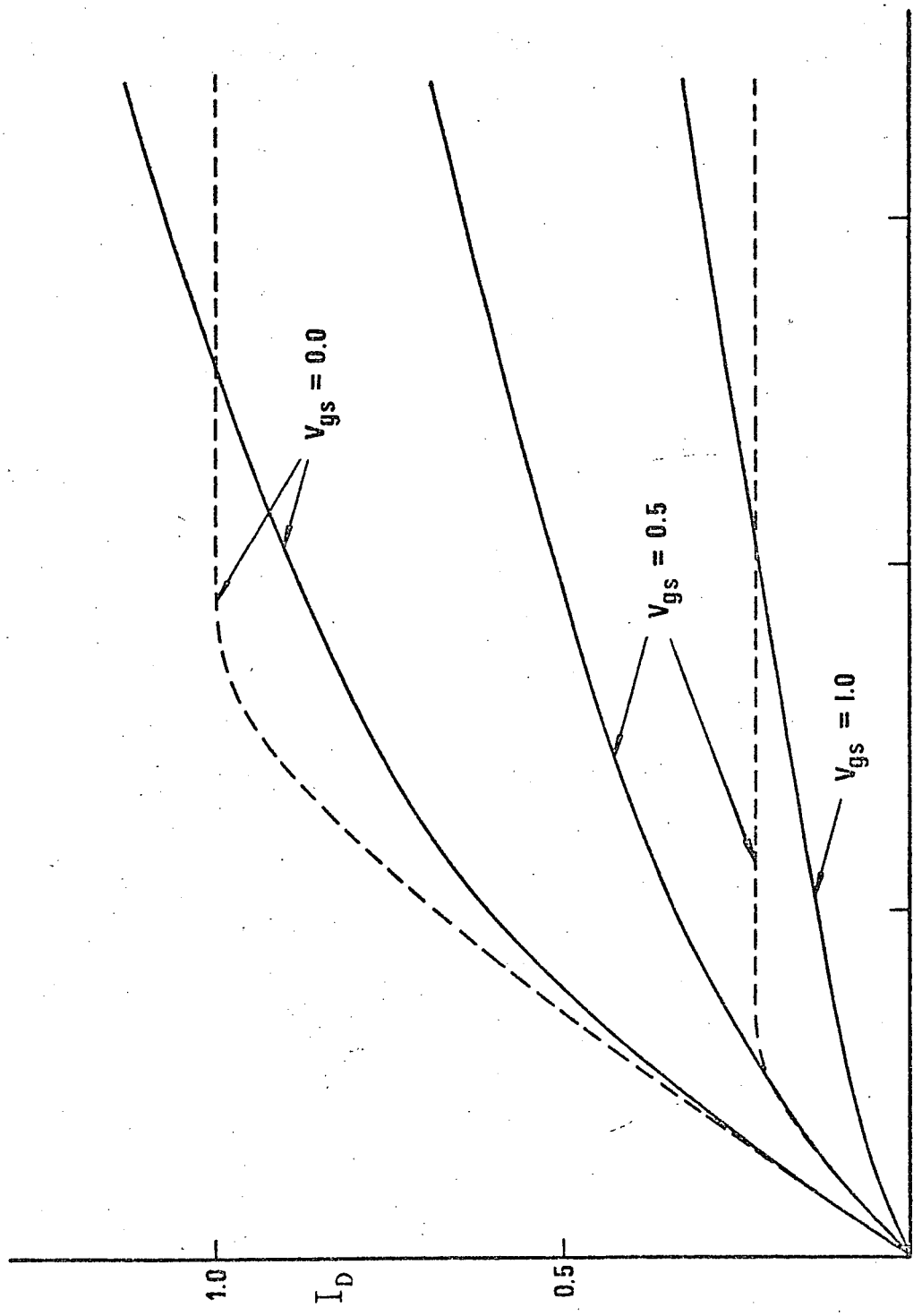

Figure 4.18 Drain characteristics of the graded-channel device

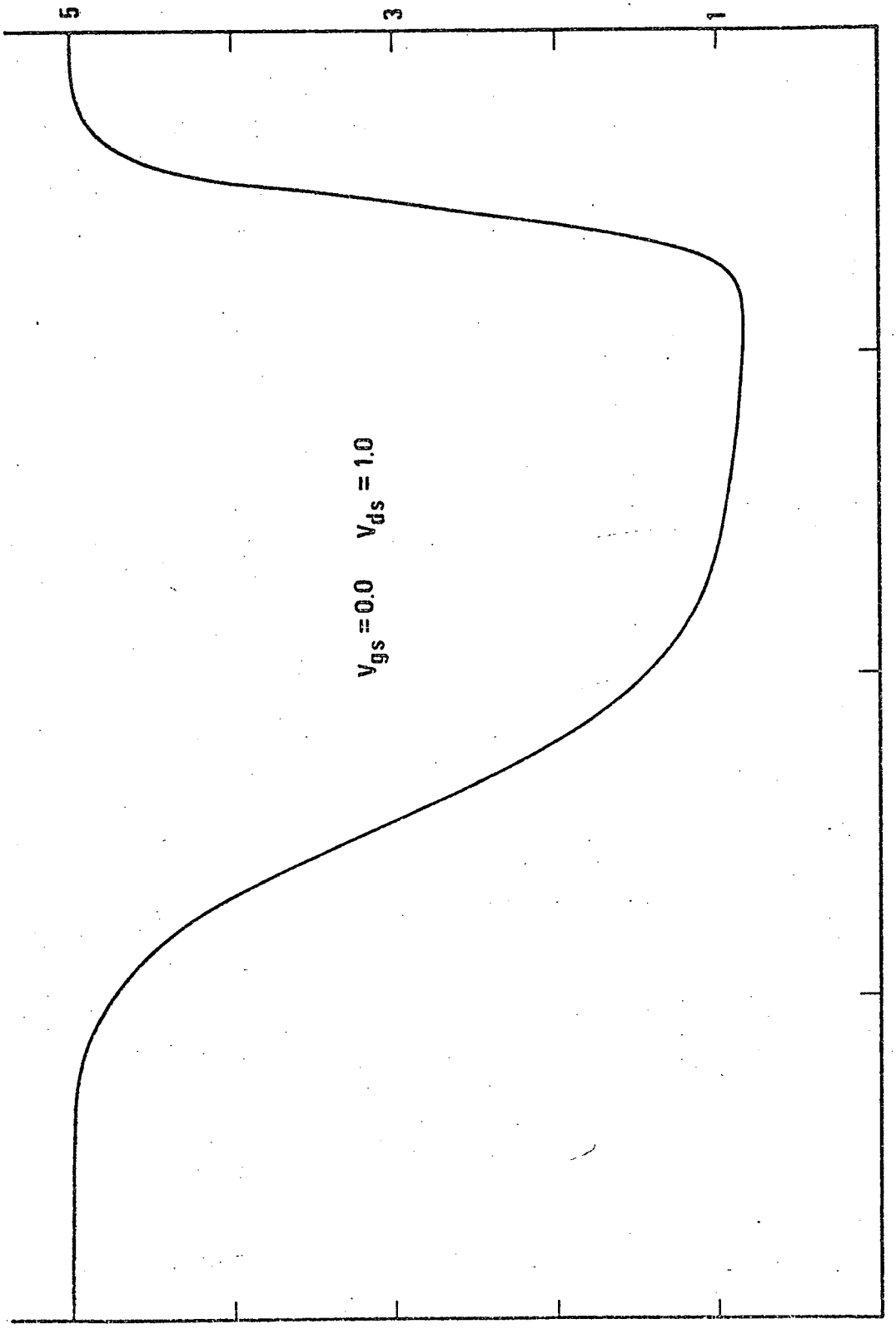

Figure 4.19-a Electron concentration on X-axis vs. x for the graded-channel device

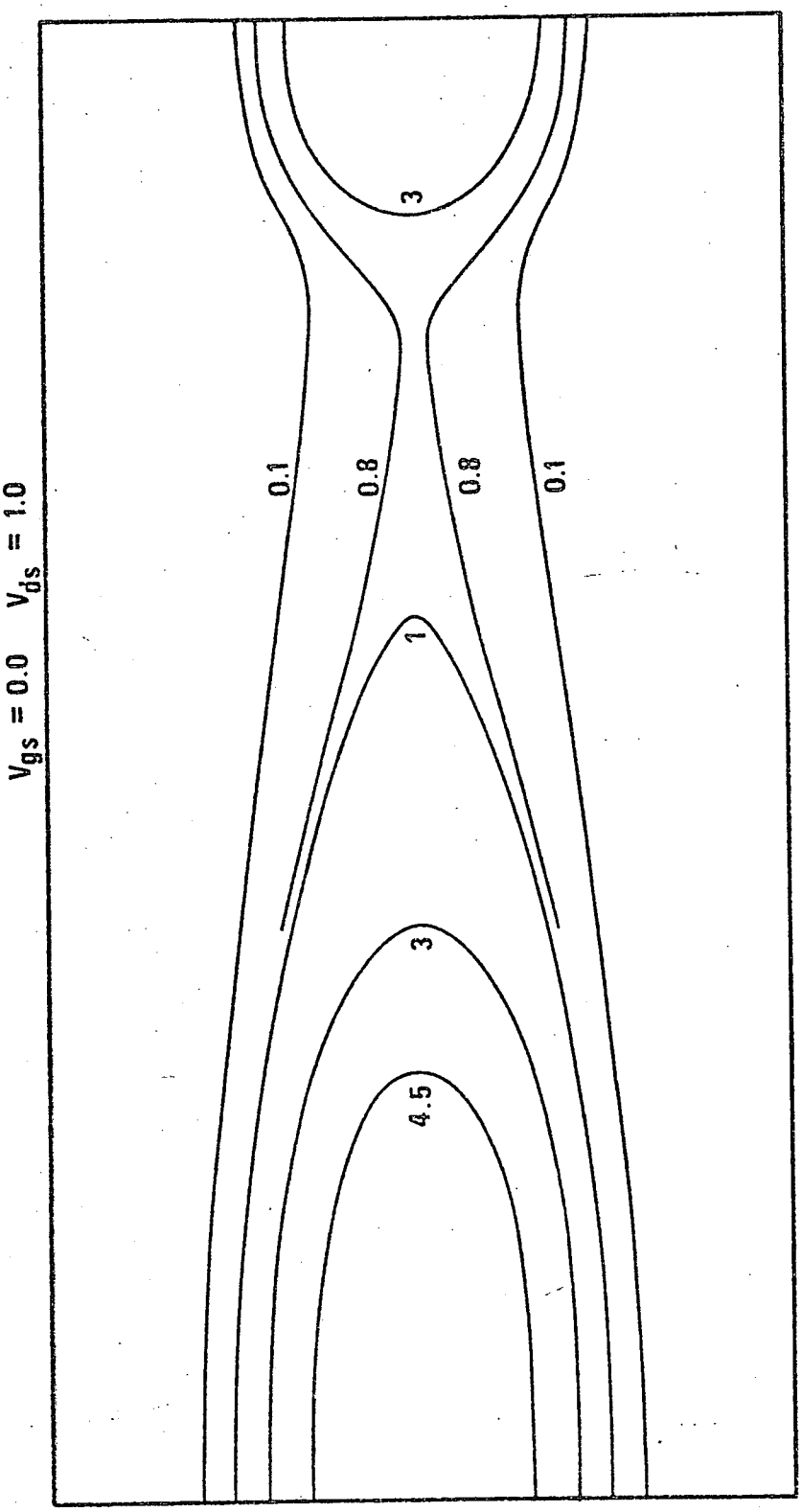

Figure 4.19-b Distribution of electron concentration for the graded-channel device

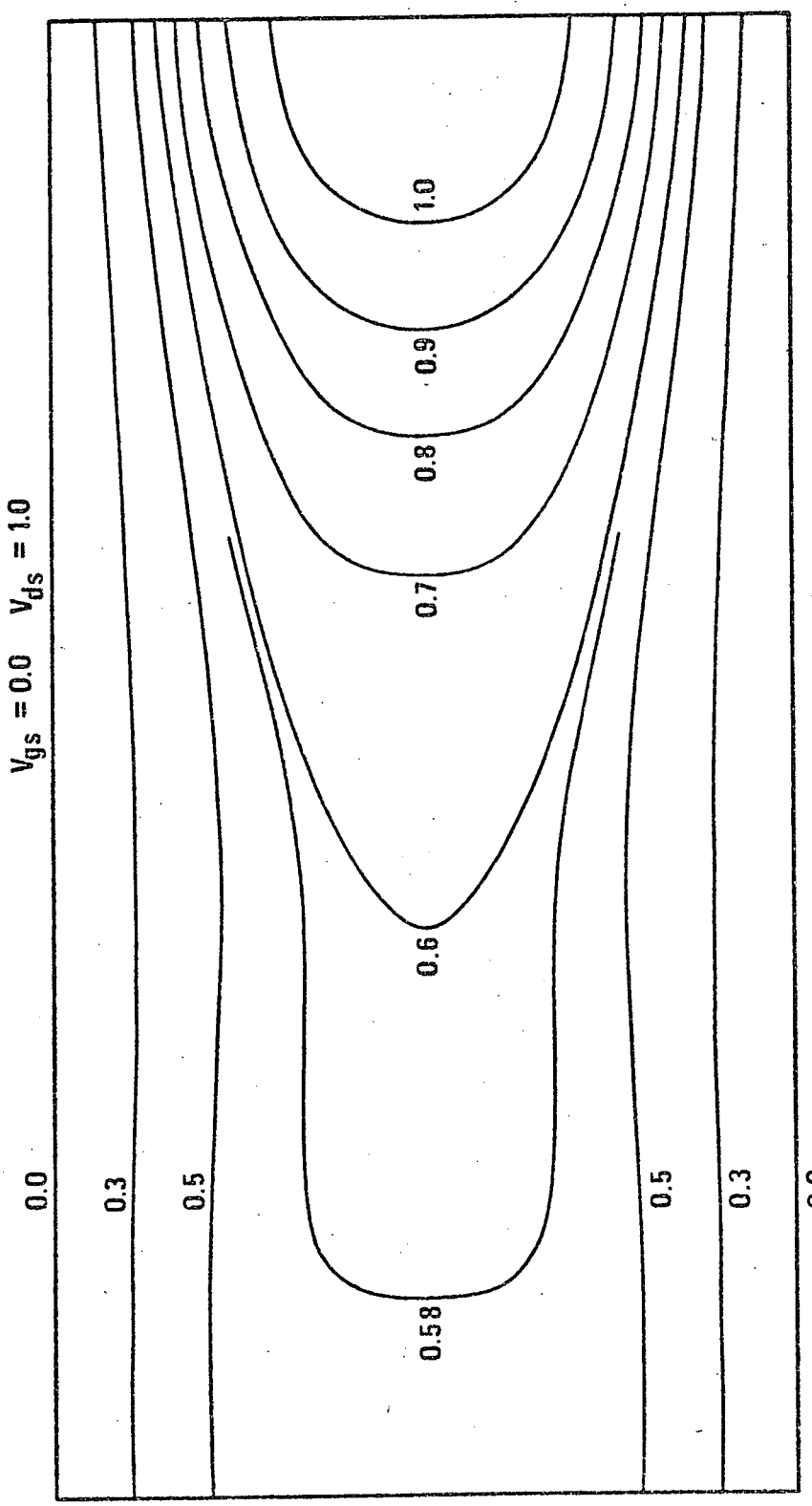

Figure 4.20 Potential distribution for the graded-channel device

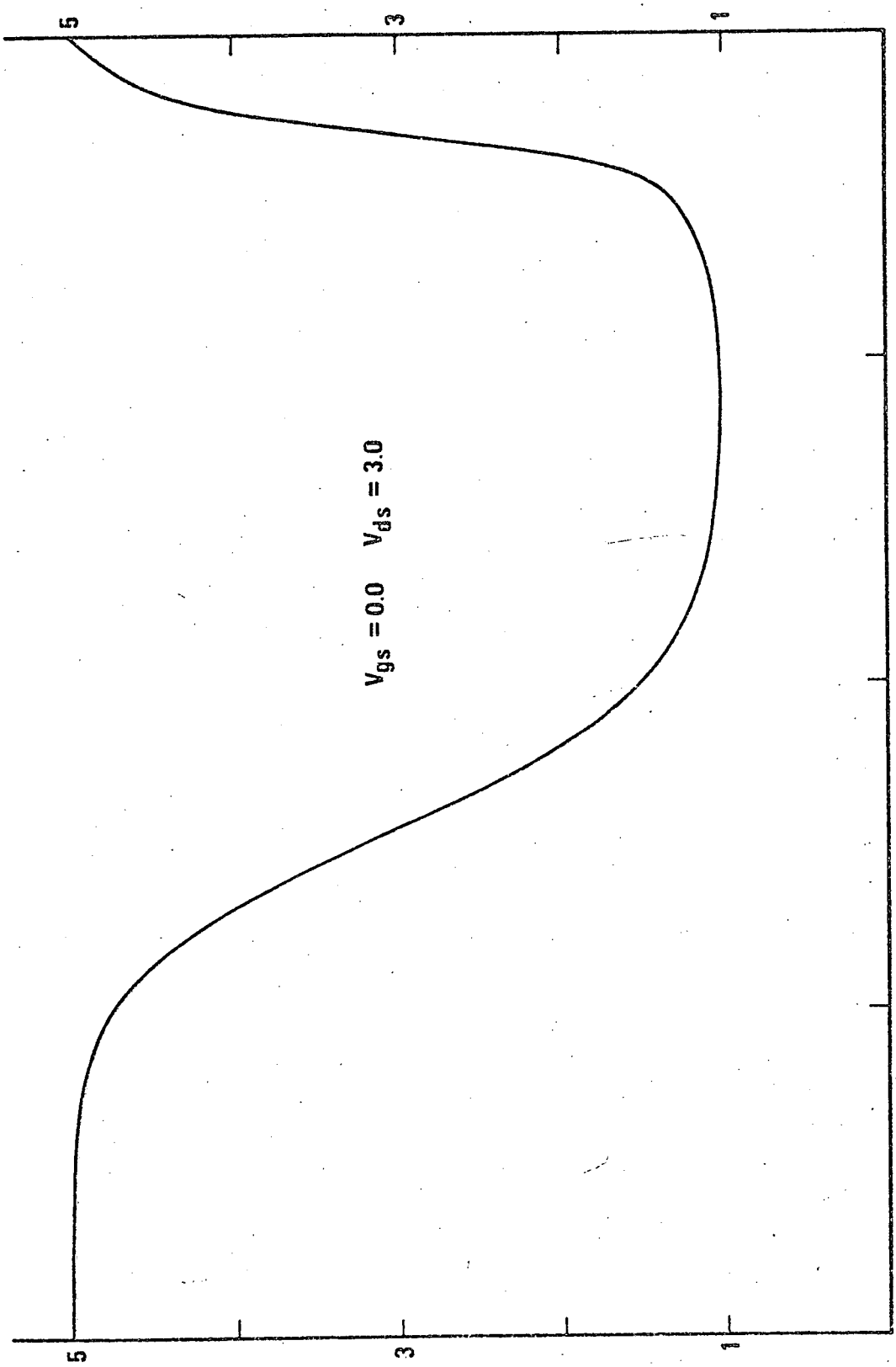

Figure 4.21-a Electron concentration on X-axis vs. x for the graded-channel device

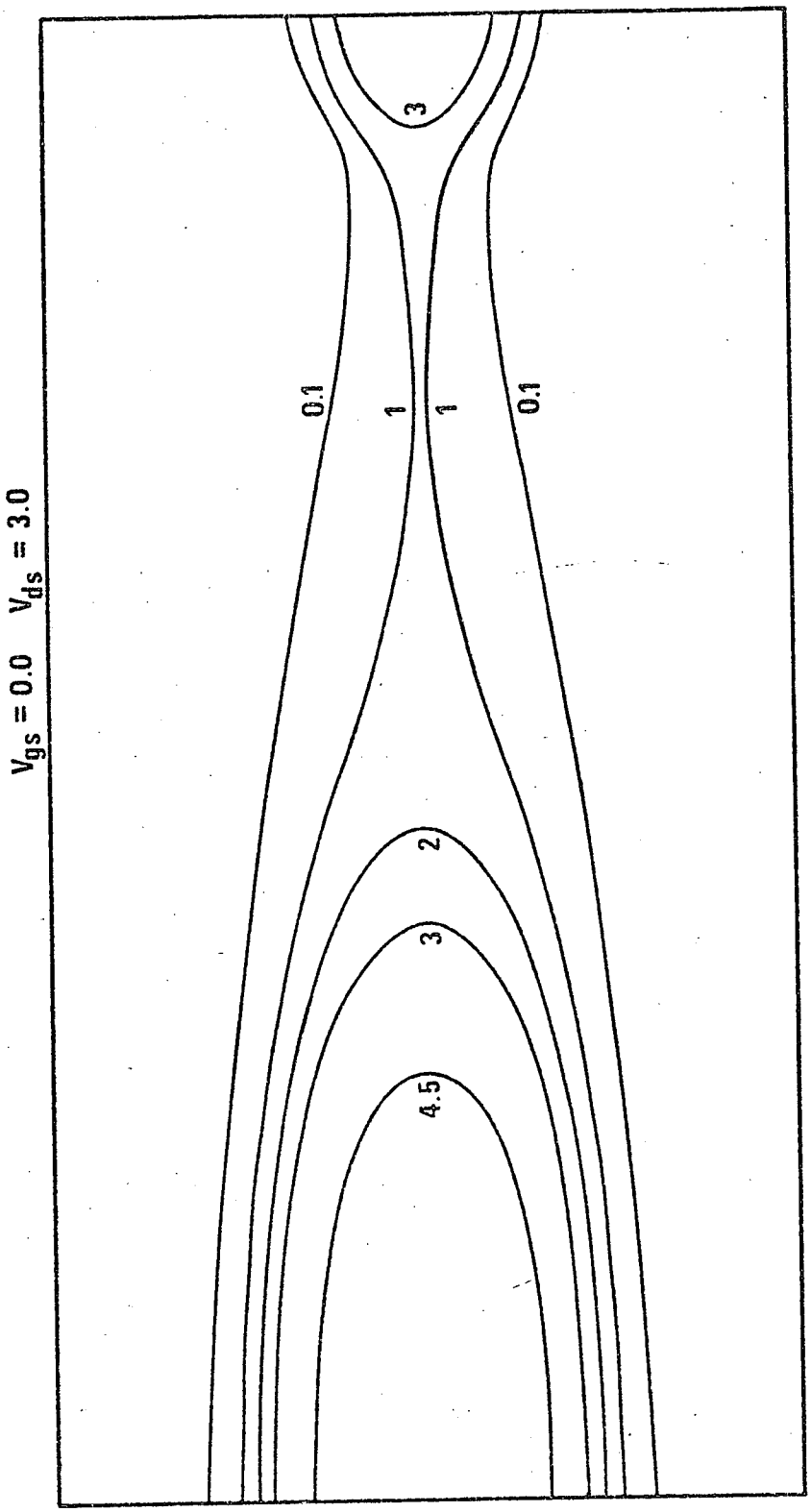

Figure 4.21-b Distribution of electron concentration for the graded-channel device

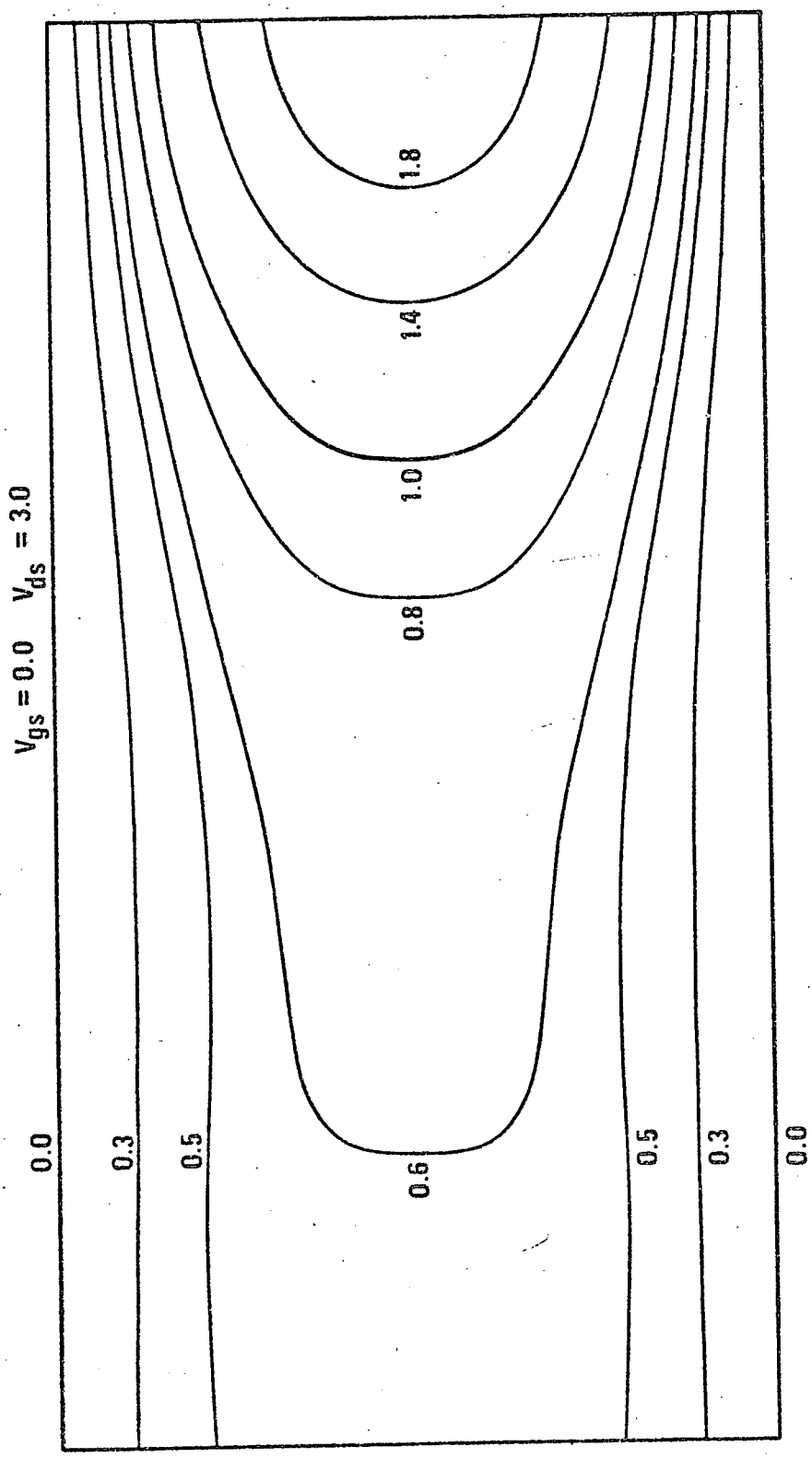

Figure 4.22 Potential distribution for the graded-channel device

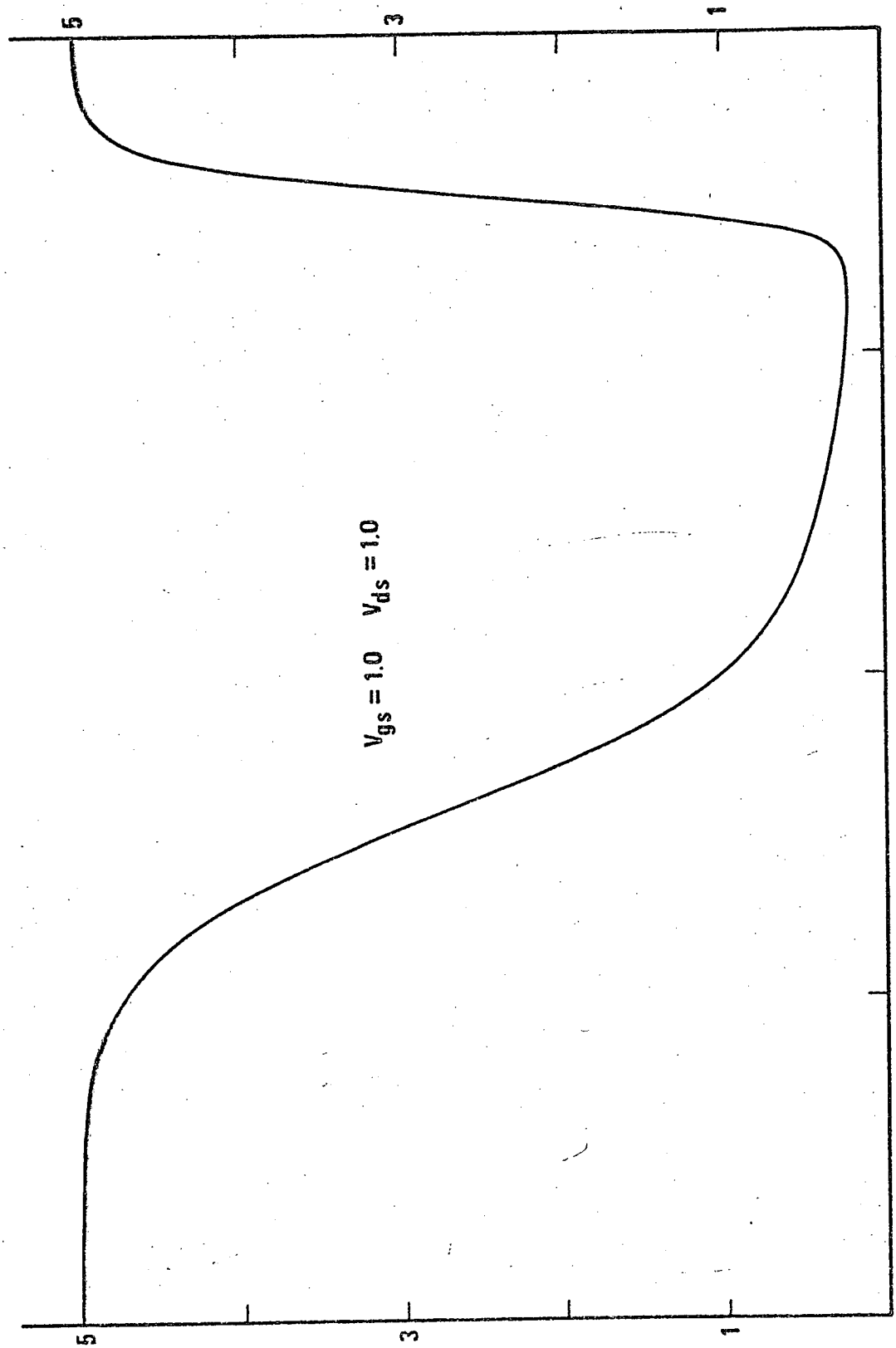

Figure 4.23-a Electron concentration on X-axis vs. x for the graded-channel device

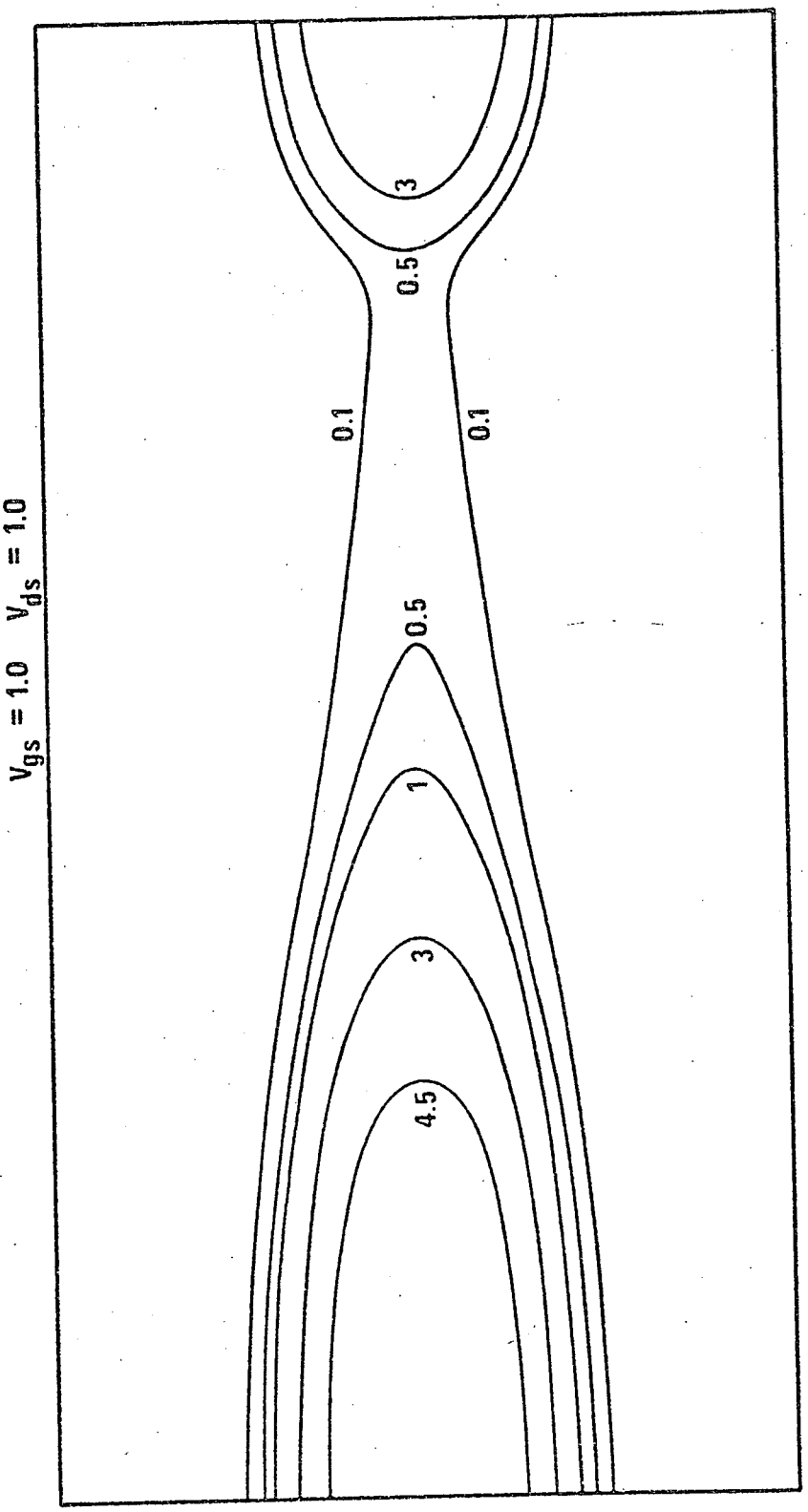

Figure 4.23-b Distribution of electron concentration for the graded-channel device

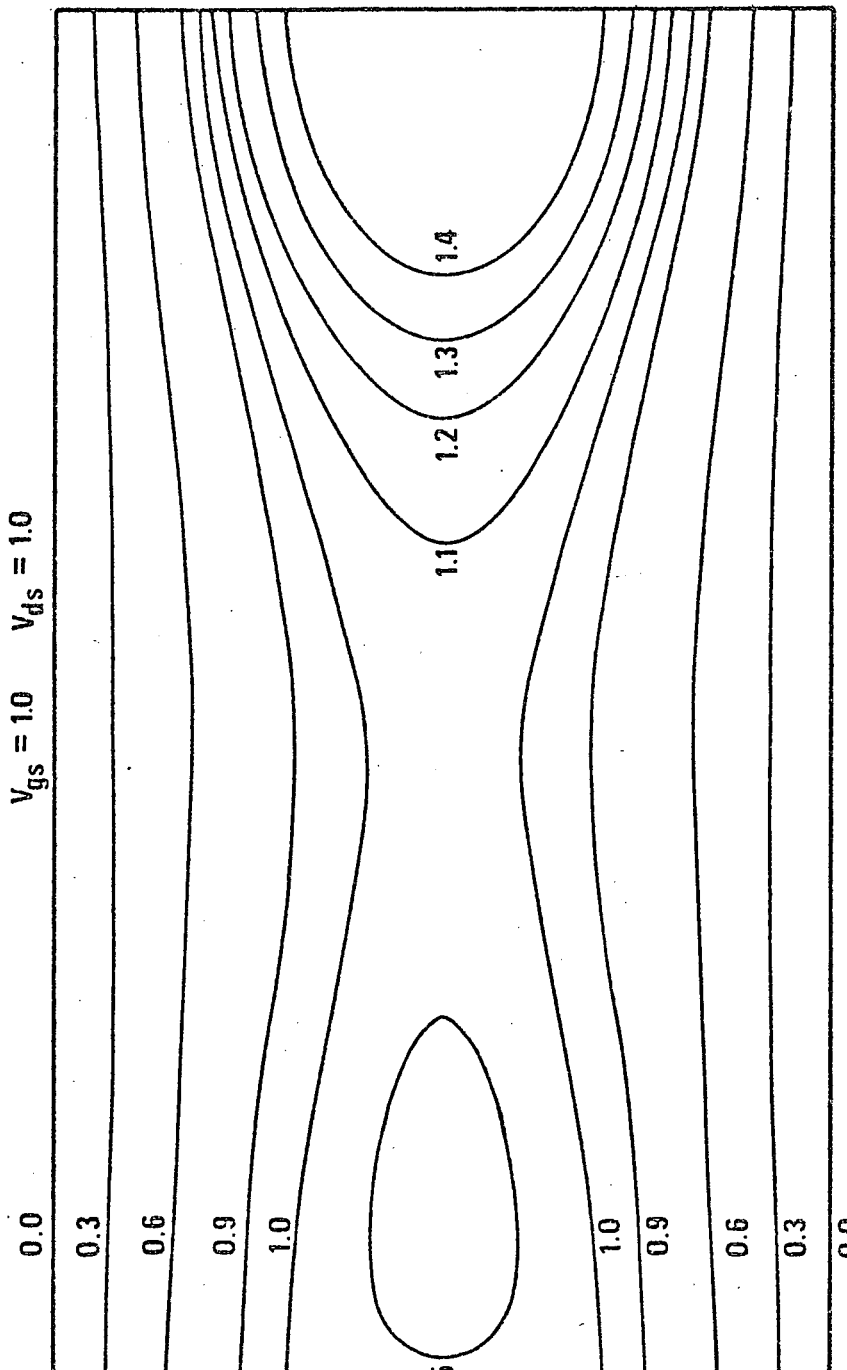

Figure 4.24 Potential distribution for the graded-channel device

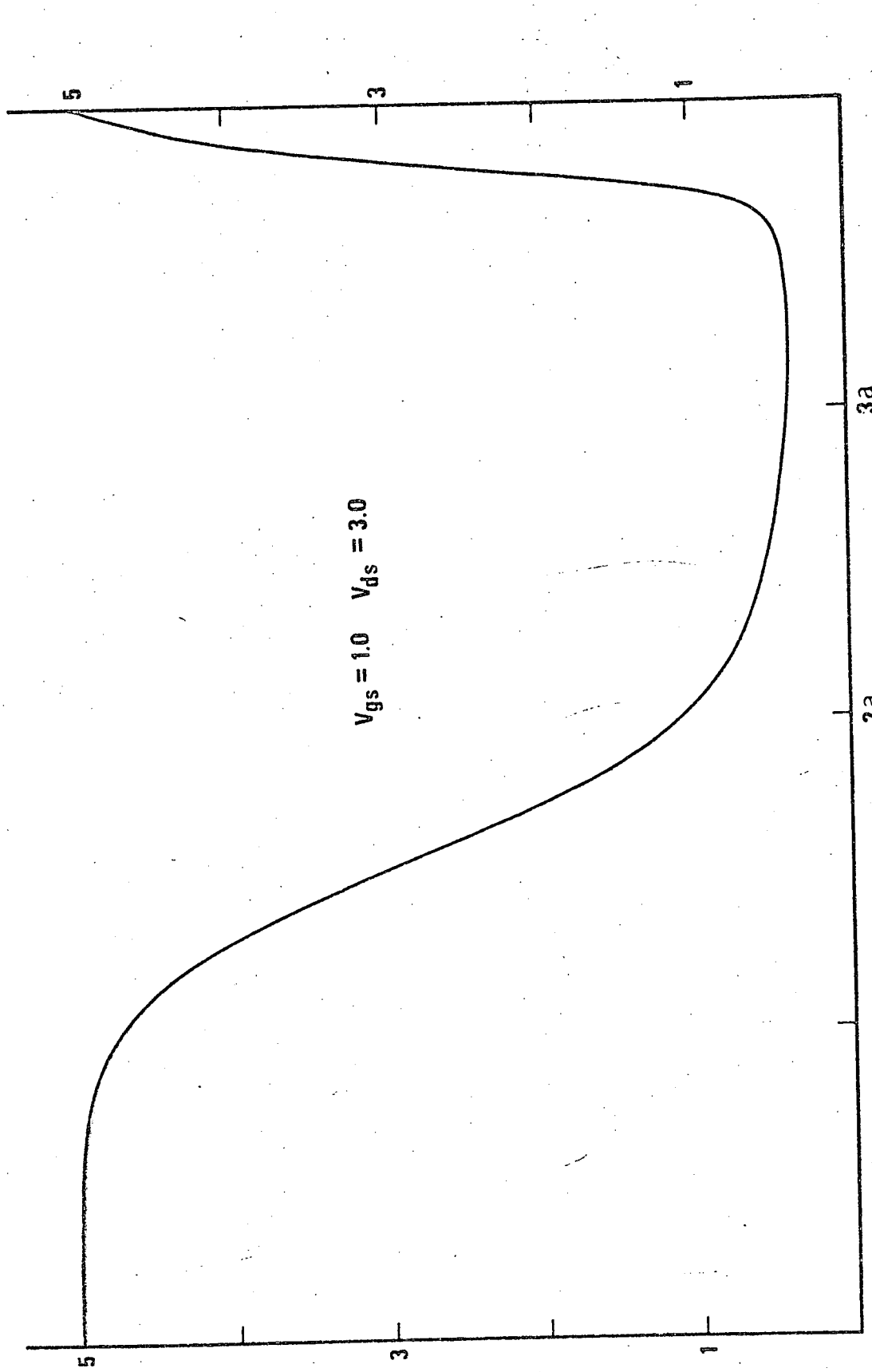

Figure 4.25-a Electron concentration on X-axis vs. x for the graded-channel device

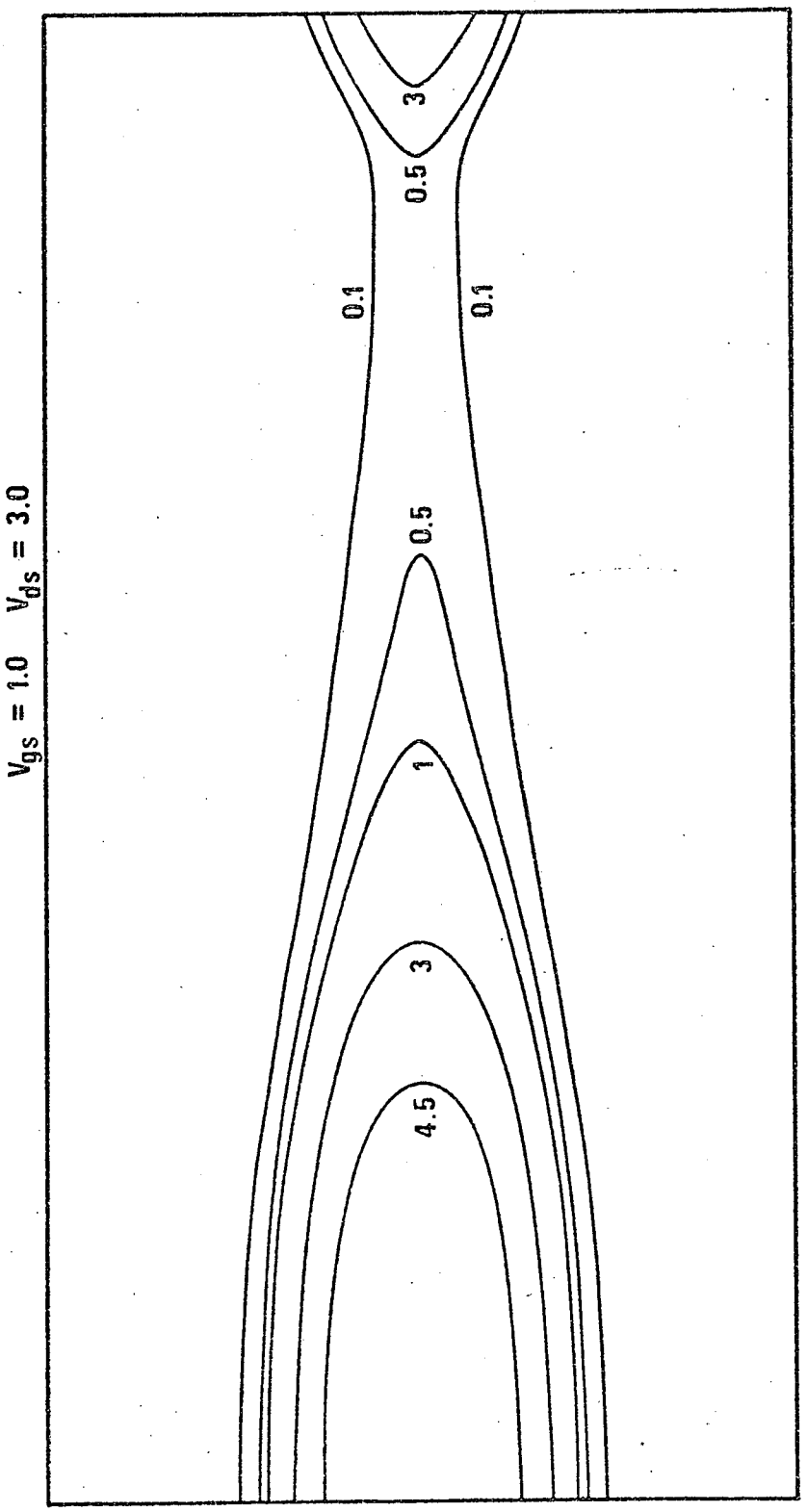

Figure 4.25-b Distribution of electron concentration for the graded-channel device

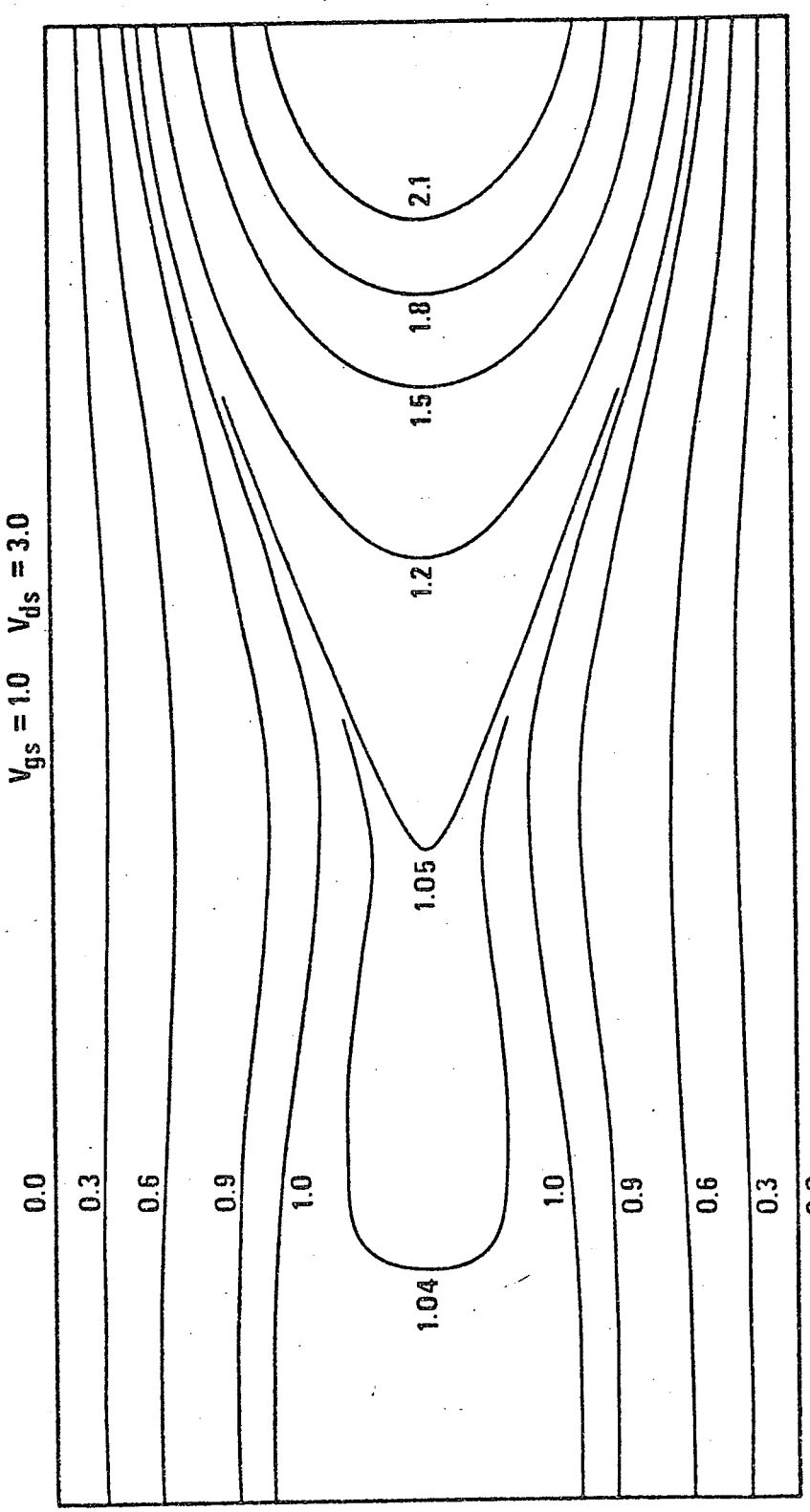

Figure 4.26 Potential distribution for the graded-channel device

Chapter V: SPACE-CHARGE-LIMITED TRIODES

Besides the experimental works of Teszner and Gicquel[16] and Zuleeg[17], there are also some theoretical works about the insulated-gate FETs with triode characteristics. Geurst[35] has analyzed the insulated-gate FETs by choosing a symmetric device model where the current flows on the center line of the device. By using the theory of complex variables, the Laplace's equation is solved rigorously in the insulator gate region with the non-linear boundary condition given along the center line. The solution gives a transcendental equation and the drain characteristics are obtained by finding the roots of the equation. Neumark and Rittner[36,37] have noted that the transcendental equation has two sets of roots of physical interest and that the choice of a set of roots gives either the pentode-like or the triode-like characteristics. These analyses are purely mathematical and lack the physical understanding of the device operation.

We have seen in section IV-2 that the interaction of the source and the drain N^+-regions gives the SCL current. This SCL current is similar to that observed by Gregory and Jordan[38] in their P^+-P-P^+ structure. The SCL triode considered in this chapter is based on the SCL current of the one-dimensional N^+-N-N^+ structure which is analyzed in the first section. In the second section, the effect of a gate P-N junction is combined with the results of the first section to obtain the triode-like characteristics.

V-1 One-Dimensional N^+-N-N^+ Structure

The SCL current can be realized in either N^+-P-N^+ or N^+-N-N^+ structure. The former is equivalent to the bipolar transistor with floating base operating beyond punch-through. This structure forms the basis of Zuleeg's SCL triode[17] and is relatively well understood.[31] In this section, the N^+-N-N^+ structure is discussed including the effect of the fixed space charge of the residual donor concentration and the field-dependent mobility.

Fig. 5.1 shows the model of this structure. The doping profile in the N- and the N^+-regions is constant and the N^+-N junctions are step junctions. The size of the N^+-regions are large enough to have the thermal equilibrium condition at $X = 0$ and $X = L_o$. According to Gregory and Jordan[38], the crossover between the Ohmic and Child's law regions occurs when the applied bias voltage is approximately equal to the crossover voltage, V_Ω.

$$V_\Omega = \frac{qN_D L^2}{2\epsilon\epsilon_o} \tag{5.1}$$

where N_D is the donor concentration in the N-region and L is the length of the N-region. The equations describing the structure are the one-dimensional forms of equations (2.6) and (2.7):

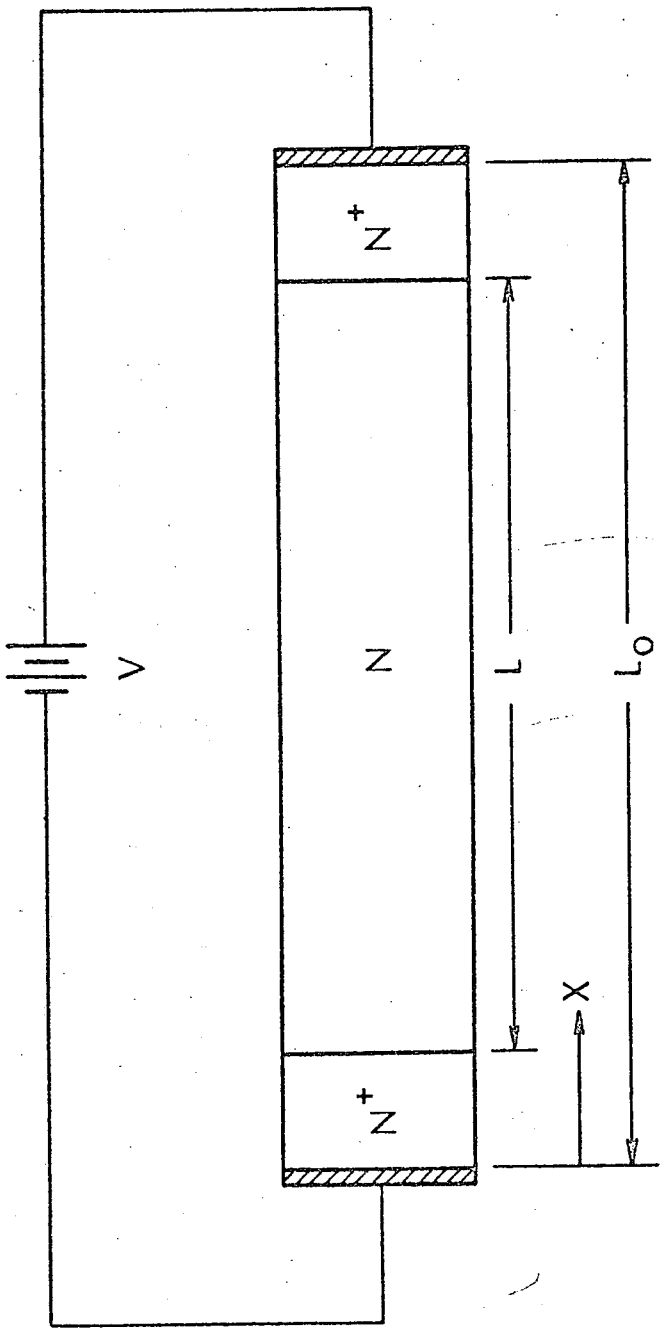

Figure 5.1 One-dimensional N^+-N-N^+ structure

$$\frac{d^2\Psi}{dx^2} = - 2\beta \left[N(x) - e^{\Psi-\varphi_n} \right] \tag{5.2}$$

$$J = \frac{J_o}{\beta} e^{\Psi-\varphi_n} \mu_n \frac{d\varphi_n}{dx} = \text{constant} \tag{5.3}$$

where J is the current density and

$$\beta = \frac{qV_r}{kT}$$

$$J_o = - q \mu_{no} N_D V_r/L$$

The linear dimension, x is normalized by L. All other symbols have the same meaning and the same normalizing constant as in equations (2.6) and (2.7). Integration of equation (5.3) gives

$$e^{-\varphi_n(x)} = e^{-\varphi_n(\ell_o)} + \beta \frac{J}{J_o} \int_x^{\ell_o} e^{-\Psi} \mu_n^{-1} dx \tag{5.4}$$

where $\ell_o = \frac{L_o}{L}$. Putting x = 0 in equation (5.4), we have

$$J = \frac{J_o}{\beta} \frac{e^{-\varphi_n(o)} - e^{-\varphi_n(\ell_o)}}{\int_o^{\ell_o} e^{-\Psi} \mu_n^{-1} dx} \tag{5.5}$$

The boundary conditions for equation (5.2) are obtained from the applied bias voltage and the thermal equilibrium condition

at $X = 0$ and $X = L_o$.

$$\Psi(o) = \varphi_n(o) + \ln \frac{N_D^+}{N_D} \tag{5.6}$$

$$\Psi(\ell_o) = \varphi_n(\ell_o) + \ln \frac{N_D^+}{N_D} \tag{5.7}$$

$$\varphi_n(\ell_o) - \varphi_n(o) = \beta \frac{V}{V_\Lambda} \tag{5.8}$$

where N_D^+ is the donor concentration in the N^+-regions and V is the applied bias voltage.

By applying the method developed in Chapter III, equations (5.2), (5.4), and (5.5) are solved numerically with the boundary conditions given by equations (5.6) - (5.8). The parameters of the particular structure considered here are

$$N_D = 10^{13} \text{ atoms/cm}^3$$

$$N_D^+ = 5 \times 10^{17} \text{ atoms/cm}^3$$

$$L = 8.285 \text{ Microns}$$

$$\beta = 20$$

$$V_\Lambda = 0.517 \text{ Volts}$$

The length of the N-region, L is 6.32 times the extrinsic Debye length of that region. Since a small deviation from the thermal equilibrium condition is damped out in about $3L_{DE}$, L is small enough for the two N^+-regions to interact with each other. The

size of the N^+-regions is 0.148 Microns and is about 25 times the extrinsic Debye length of that region. Therefore, the thermal equilibrium condition is satisfied at the contacts. Because the problem is one-dimensional, different mesh sizes in N- and N^+-regions can be used without much difficulty. The mesh sizes are chosen such that the ratios of the mesh size to the extrinsic Debye length are 0.0253 in the N-region and 0.632 in the N^+-regions.

When the mobility is assumed to be a constant and when the fixed space charge due to the donor impurities is neglected, an approximate analysis[39] gives the SCL current as

$$J = \frac{9}{16} J_o \left(\frac{V}{V_\Omega}\right)^2 \qquad V >> V_\Omega \tag{5.9}$$

If the electron concentration in the N-region is assumed to be equal to the donor concentration for small bias voltage, the current in the Ohmic region is

$$J = J_o \left(\frac{V}{V_\Omega}\right) \qquad V << V_\Omega \tag{5.10}$$

Fig. 5.2 shows the computed I-V characteristic. The current densities given by equations (5.9) and (5.10) are also shown in the figure by two straight lines. In the figure, the current density is normalized by $9J_o/16$. Due to the factor 9/16, the two straight lines intersect each other when the applied voltage

is greater than the crossover voltage. The larger current of the computed result in the linear region is due to the interaction of the two N^+-regions, which gives greater electron concentration than the donor concentration for the zero bias voltage. Denda and Nicolet[31] have shown that for the three cases of thermal, tepid, and hot charge carriers the asymptotic dependences of the I-V characteristics are power laws of V^2, $V^{3/2}$, and V, respectively. For the model considered here, the electric field at the point where the electron concentration is minimum is 15.77 Kv/cm when $V = 15\ V_n$. Therefore, the electric field is in the tepid region for most of the N-region and the rate of increase of the current with increasing voltage is smaller than V^2.

The distribution of the electro-static potential in the N-region is shown in Fig. 5.3 for various bias voltages. In this figure and in Figs. 5.4 and 5.5 the origin of the X-axis is shifted to the metallurgical junction of the left N^+-N junction. The slight decrease of the potential near $X = 0$ is due to the built-in potential of the N^+-N junction.

Fig. 5.4 shows the electron concentration in the N-region for several bias conditions. The increase of the electron concentration with increasing bias voltage is clearly seen. It is also to be noted that the electron density tends to become constant with increasing bias voltage. This is due to the field dependent mobility and when the drift velocity is completely saturated, the electron density should be a constant. This is conformed by

considering another N^+-N-N^+ structure which has the same crossover voltage but has a smaller length (L = 2.62 Microns). Fig. 5.5 shows the electron density and the electric field when V = 15 V_Ω. It is clearly seen in this figure that the electron density is constant when the electric field is greater than about 25 Kv/cm. The current has been found to increase more slowly for this structure than for the one considered before. This is in agreement with the asymptotic dependence of the SCL current for hot charge carriers.

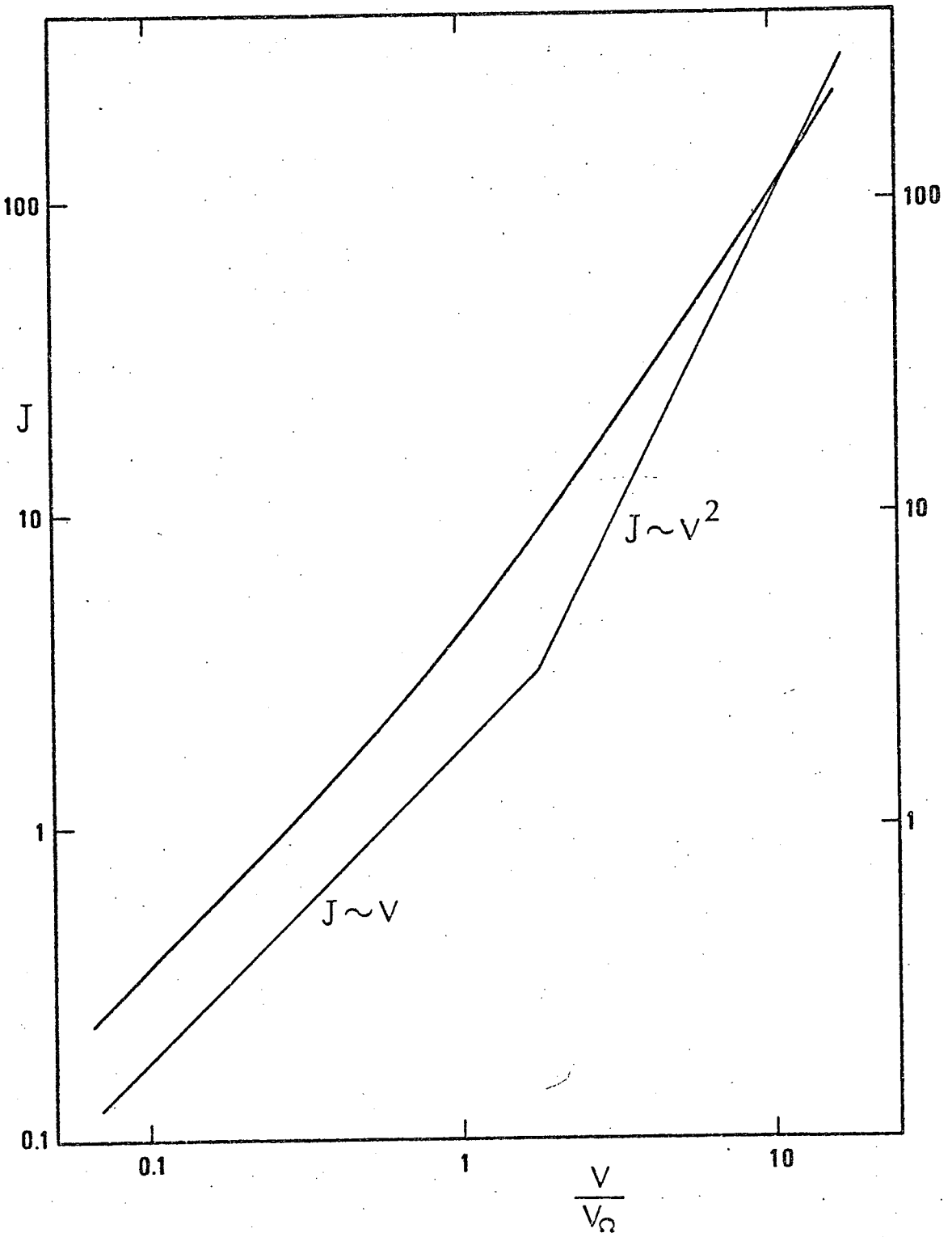

Figure 5.2 I-V characteristic of the N^+-N-N^+ structure

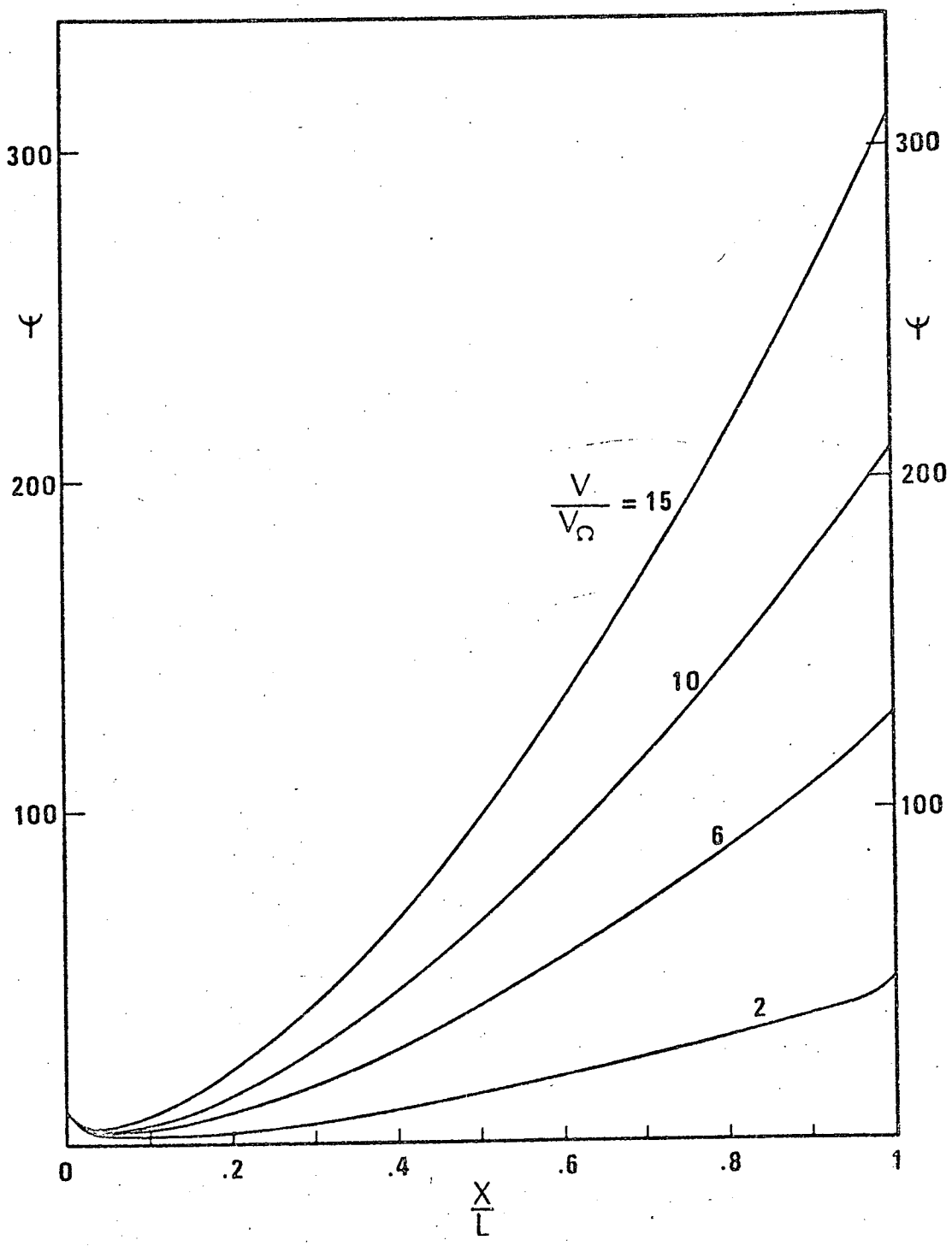

Figure 5.3 Electro-static potential vs. X for the N^+-N-N^+ structure

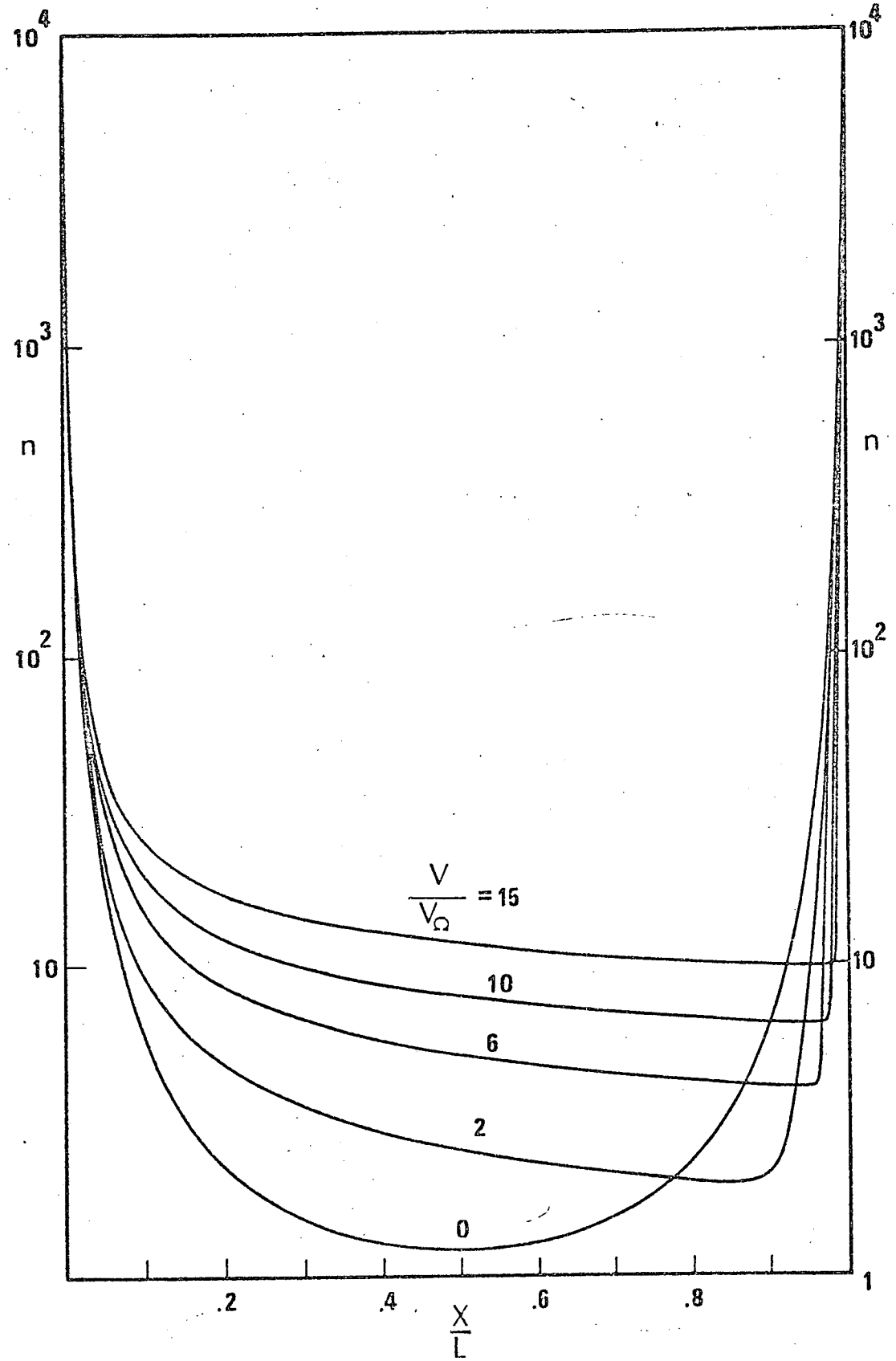

Figure 5.4 Electron concentration vs. X for the N^+-N-N^+ structure

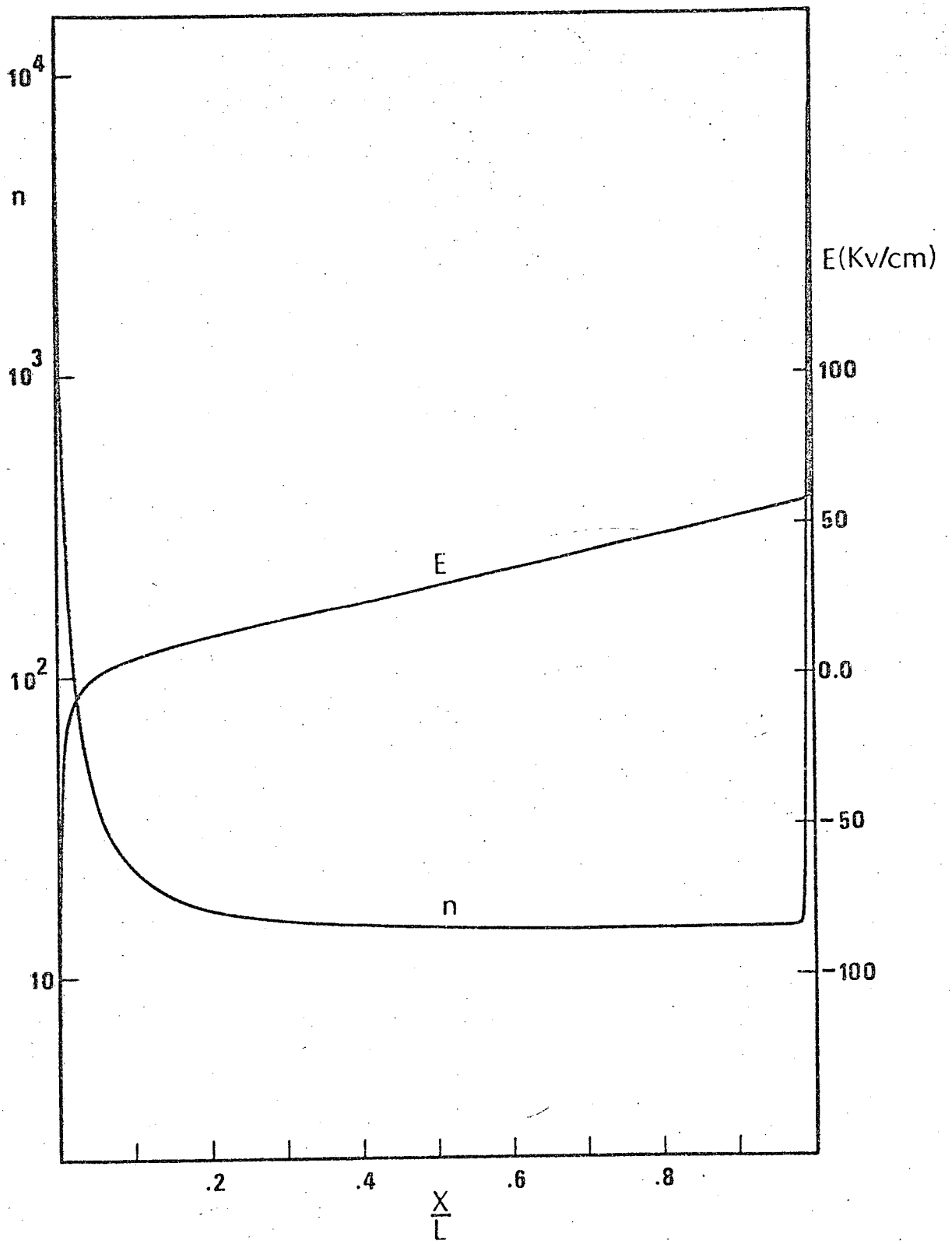

Figure 5.5 Electron concentration and electric field for the N^+-N-N^+ structure with a small L

V-2 Triode Characteristics

In this section we consider a symmetric device in which the N^+-N-N^+ structure discussed in the previous section is sandwiched between two heavily doped P^+ gate regions. Let the width of the structure be 2a. This device will be called the 'SCL triode'. The geometrical structure of this device is essentially the same as a normal JFET with pentode-like characteristics. The important difference is the L/L_{DE} ratio of the N-region. For the long and the short device considered in Chapter IV, L/L_{DE} is 80 and 20 respectively. Therefore, the two N^+-regions do not interact with each other and the N^+-N junctions are simple Ohmic junctions. On the other hand, L/L_{DE} for the SCL triode is only about 6 and the SCL current flow can easily be realized.

The correct description of this device should be based on the two-dimensional analysis similar to those for the normal JFETs. Due to the high doping level of the N^+-regions, however, the numerical method becomes extremely complicated. Instead of solving the pertinent equations exactly, an approximate but simple analysis is presented in this section which can give the general behavior of the external drain characteristics.

We have seen in Chapter IV that devices with small L/a ratios have poor saturation of the drain current when the drift velocity is not saturated. When the drain voltage is increased,

the decrease of the channel width and the free carrier concentration inside the channel have been found to be smaller for the short device than for the long device. In the graded-channel device, the carrier accumulation has been observed in the channel with a slight interaction of the source and the drain N^+-regions.

Suppose the SCL triode has a relatively small length-to-width ratio ($L/a \sim 1$). Due to the small L/a ratio and the strong interaction of the N^+-regions, the drain current is determined mainly by the current density of the N^+-N-N^+ structure with the gate junction controlling the width of the conductive channel. Let 2b be the width of this channel. Then, the drain current per unit length in the Z-direction can be written as

$$I_D = 2\, J_{SCL}(V_{ds})\, \bar{b}(V_{ds},V_{gs}) \tag{5.11}$$

where J_{SCL} is the magnitude of the current density obtained in previous section and $\bar{b}$ is an average of b. V_{ds} and V_{gs} in equation (5.11) and in the rest of this chapter are the magnitudes of the unnormalized drain-to-source and the gate-to-source voltage. In evaluating b, one should note that a larger potential is required to deplete the increased carrier concentration in the conductive channel. This can be taken care of by introducing

$$V_p' = n\, V_p \tag{5.12}$$

Here n is the normalized electron concentration in the conductive channel and V_p is the pinch-off voltage of the device. By using

the results of a one-dimensional analysis with V_p replaced by V_p', one obtains

$$b = a\left(1 - \sqrt{\frac{V}{V_p'}}\right) \tag{5.13}$$

where V is the potential drop across the space-charge region. Let

$$V_{pc} = n\left(\frac{L_o}{2}\right) V_p \tag{5.14}$$

A reasonable estimate of $\bar{b}$ can be obtained by using V_{pc} for V_p' and $V_{gs} + V_B$ for V in equation (5.13).

$$\bar{b} \simeq a\left(1 - \sqrt{\frac{V_{gs} + V_B}{V_{pc}}}\right) \tag{5.15}$$

The triode characteristics shown in Fig. 5.6 are the result of applying equations (5.11) and (5.15) to a device with L/a = 1. The doping level of the gate P^+-regions is $N_A = 10^{20}$ atoms/cm^3. The drain current for the bias conditions such that $V_{gs} + V_B \geq V_{pc}$ is taken to be zero.

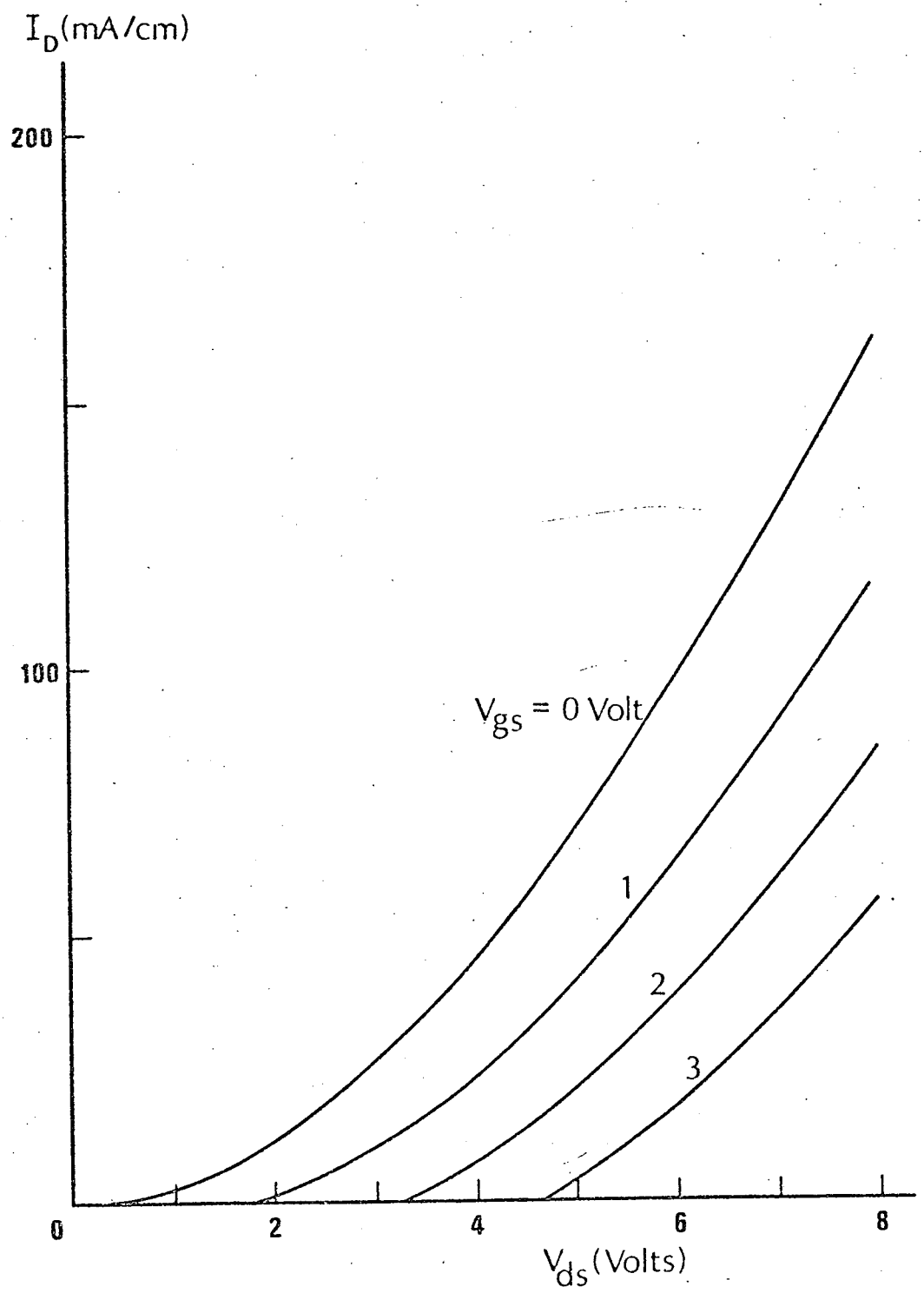

Figure 5.6 Drain characteristics of the SCL triode

V-3 Comparison of the Drain Characteristics

The important parameters characterizing a JFET are

L/a = length-to-width ratio

V_p = pinch-off voltage = $\frac{qN_D}{2\epsilon\epsilon_o} a^2$

V_Λ = crossover voltage = $\frac{qN_D}{2\epsilon\epsilon_o} L^2$

L_{DE} = extrinsic Debye length of the channel

$$= \sqrt{\frac{\epsilon\epsilon_o kT}{q^2 N_D}}$$

$\alpha = qV_p/kT$

$\beta = qV_\Lambda/kT$

These parameters are related as

$$\frac{a}{L_{DE}} = \sqrt{2\alpha}$$

$$\frac{L}{L_{DE}} = \sqrt{2\beta}$$

$$\frac{V_\Lambda}{V_p} = \frac{\beta}{\alpha} = \left(\frac{L}{a}\right)^2$$

Depending on the choice of these parameters and the bias voltages both pentode-like and triode-like drain characteristics can be obtained. The long device considered in Chapter IV has good pentode-like characteristics. The values of the parameters

for this device are

$$L/a = 8$$

$$V_p = 1.293 \text{ Volts}$$

$$V_\Omega = 83.75 \text{ Volts}$$

$$\alpha = 50$$

$$\beta = 3200$$

The applied bias voltages are less than 5 Volts. On the other hand, the SCL triode considered in this chapter has

$$L/a = 1$$

$$V_p = V_\Omega = 0.517 \text{ Volts}$$

$$\alpha = \beta = 20$$

and the applied bias voltages are less than 10 Volts.

From the above comparison, it is clear that one can design a field-effect device having pentode- or triode-like characteristics by choosing the parameters appropriately. The importance of this observation is that both characteristics can be obtained without changing the configuration of the device.

Chapter VI: CONCLUSION

A numerical method of analyzing JFETs has been developed and applied to several device models to determine the physical mechanism of the current conduction. The conventional JFETs with N-channel have been analyzed including the source and the drain N^+-regions. The results show that

i) In the region near drain, the channel width and the electron concentration decrease with increasing drain-to-source voltage. As a result, space-charge region is formed not only in the N-region but also in the drain N^+-region and most of the voltage drop occurs in these space-charge regions, leaving the potential distribution in the source region unchanged. This gives the saturation of the drain current.

ii) Although the electron concentration decreases with the increasing drain and gate voltage, there is always a conduction path connecting the source and the drain contacts.

iii) When the drift velocity is not saturated, the differential drain conductance and the minimum of the electron concentration along the center line of the device are greater for a shorter device for the drain voltage beyond the pinch-off voltage.

iv) Increasing the gate voltage decreases the channel width uniformly from the source to the drain and the operation of a JFET with non-zero gate voltage is equivalent to the operation of another JFET with correspondingly smaller a and the same L and zero gate voltage.

The application of the method to a device model with non-uniform doping profile along the channel shows the carrier accumulation in the conductive channel. This indicates the possibility of the space-charge-limited current which is a different conduction mechanism from that of the conventional JFETs. From the study of one-dimensional N^+-N-N^+ structures, the L/L_{DE} ratio and the crossover voltage have been recognized as important parameters in realizing the space-charge-limited current. The drain characteristics of a device model with a small crossover voltage and a small L/L_{DE} ratio are obtained by a simple analysis. Triode-like characteristics have been found for this model as expected.

The variation of the mobility with the impurity concentration is of secondary importance for the purpose of the present investigation and has been neglected accordingly. The effect of the temperature to the mobility and the free carrier concentration has also been neglected. When the power handling capability of a JFET is under investigation, these temperature dependences may be important due to the high current density near the drain. For

the present investigation, a constant temperature equal to the room temperature has been assumed throughout the whole device.

The numerical method developed can also be applied to insulated-gate FETs with minor revisions when the boundary conditions are known. When the storage space and the computing time available are large enough, a two-dimensional analysis of the SCL triode will become possible.

REFERENCES

1. W. Shockley, "A unipolar field-effect transistor," Proc. IRE vol. 40, pp. 1365-1376, November 1952.
2. G. C. Dacey and I. M. Ross, "Unipolar field-effect transistor," Proc. IRE, vol. 41, pp. 970-979, August 1953.
3. L. Esaki and L. L. Chang, "Ultimate FET structures," Proc. IEEE, vol. 53, pp. 2117-2118, December 1965.
4. B. Buchanan, S. Roosild and R. Dolan, "Maximum gain FET configurations," Proc. IEEE, vol. 54, pp. 802-803, May 1966.
5. R. C. Prim and W. Shockley, "Joining solutions at the pinch-off point in the field-effect transistors," IRE Trans. Electron Devices, vol. PGED-4, pp. 1-4, December 1953.
6. S. Y. Wu and C. T. Sah, "Current saturation and drain conductance of junction-gate field-effect transistors," Solid-State Electronics, vol. 10, pp. 593-609, June 1967.
7. E. J. Ryder, "Mobility of holes and electrons in high electric fields," Phys. Rev., vol. 90, pp. 766-769, June 1953.
8. W. Shockley, "Hot electrons in germanium and the Ohm's law," B.S.T.J., vol. 30, pp. 990-1034, October 1951.
9. G. C. Dacey and I. M. Ross, "The field-effect transistors," B.S.T.J., vol. 34, pp. 1149-1189, November 1955.
10. F. N. Trofimenkoff, "Field dependent mobility analysis of the field-effect transistor," Proc. IEEE, vol. 53, pp. 1765-1766, November 1965.

11. K. Tarney and F. N. Trofimenkoff, "Effects of field dependent mobility on field-effect transistor characteristics," Proc. IEEE, vol. 54, pp. 1077-1078, August 1966.

12. J. Grosvalet, C. Motsch and R. Tribes, "Physical phenomenon responsible for saturation current in field-effect devices," Solid-State Electronics, vol. 6, pp. 65-67, January 1963.

13. R. Zuleeg, "Current saturation in multichannel field-effect transistors," Proc. IEEE, vol. 53, pp. 2111-2112, December 1965.

14. J. R. Hauser, "Characteristics of junction field-effect devices with small channel length-to-width ratios," Solid-State Electronics, vol. 10, pp. 577-587, June 1967.

15. A. B. Grebene and S. K. Ghandhi, "General theory for pinched operation of the junction-gate FET," Solid-State Electronics, vol. 12, pp. 573-589, July 1969.

16. S. Teszner and R. Gicquel, "Gridistor - A new field-effect device," Proc. IEEE, vol. 52, pp. 1502-1513, December 1964.

17. R. Zuleeg, "A silicon space-charge limited triode and analog transistor," Solid-State Electronics, vol. 10, pp. 449-460, May 1967.

18. W. Shockley, "The theory of p-n junctions and p-n junction transistors," B.S.T.J., vol. 28, pp. 435-489, July 1949.

19. P. E. Gray et. al., SEEC, vol. 2, Wiley, New York, 1964.

20. H. K. Gummel, "A self-consistant iterative scheme for one-dimensional steady state transistor calculations," IEEE Trans. Electron Devices, vol. ED-11, pp. 455-465, October 1964.

21. J. Early, "Effects of space-charge layer widening in junction transistors," Proc. IRE, vol. 40, pp. 1401-1406, November 1952.

22. V. G. K. Reddi and C. T. Sah, "Source-to-drain resistance beyond pinch-off in metal-oxide-semiconductor (MOST) transistors," IEEE Trans. Electron Devices, vol. ED-12, pp. 139-141, March 1965.

23. D. Young, "Iterative methods for solving partial differential equations of elliptic type," Trans. of American Mathematical Society, vol. 76, pp. 92-111, January 1954.

24. G. E. Forsythe and W. Wasow, Finite difference methods for partial differential equations, Wiley, New York, 1960.

25. J. Todd, Survey of numerical analysis, McGraw-Hill, New York, 1962.

26. D. Greenspan, Introductory numerical analysis of elliptic boundary value problems, Harper & Row, New York, 1965.

27. E. L. Wachspress, Iterative solution of elliptic systems and applications to the neutron diffusion equations of reactor physics, Prentice-Hall, Englewood Cliffs, N. J., 1966.

28. S. K. Godunov and V. S. Ryabenki, Theory of difference schemes - An introduction, North-Holland Publishing Company, Amsterdam, 1964.

29. R. C. Courant and D. Hilbert, Methods of mathematical physics, II, Interscience, New York, 1962.

30. A. Demari, "An accurate numerical steady-state one-dimensional solution of the p-n junction," Solid-State Electronics, vol. 11, pp. 33-58, January 1968.

31. S. Denda and M. A. Nicolet, "Pure space-charge-limited electron current in silicon," Journal of Applied Physics, vol. 37, pp. 2412-2424, May 1966.

32. C. Y. Duh and J. L. Moll, "Electron drift velocity in avalanching silicon diodes," IEEE Trans. Electron Devices, vol. ED-14, pp. 46-49, January 1967.

33. C. B. Norris, Jr. and J. F. Gibbons, "Measurement of high-field carrier drift velocities in silicon by a time-of-flight technique," IEEE Trans. Electron Devices, vol. ED-14, pp. 38-43, January 1967.

34. R. Zuleeg, "Multi-channel field-effect transistor theory and experiment," Solid-State Electronics, vol. 10, pp. 559-576, June 1967.

35. J. A. Geurst, "Theory of insulated-gate field-effect transistors near and beyond pinch-off," Solid-State Electronics, vol. 9, pp. 129-142, February 1966.

36. E. S. Rittner and G. F. Neumark, "Theory of the surface gate dielectric triode," Solid-State Electronics, vol. 9, pp. 885-898, September 1966.

37. G. F. Neumark and E. S. Rittner, "Transition from pentode- to triode-like characteristics in field effect transistors," Solid-State Electronics, vol. 10, pp. 299-304, April 1967.

38. B. L. Gregory and A. G. Jordan, "Single-carrier injection in silicon at 76^{o} and 300^{o}K," Journal of Applied Physics, vol. 35, pp. 3046-3047, October 1964.

39. W. Shockley and R. C. Prim, "Space-charge limited emission in semiconductors," Phys. Rev., vol. 90, pp. 753-758, June 1953.